UNIVERSITEIT
STELLENBOSCH
UNIVERSITY

Dynamics and Energy Management of Electric Vehicles

Daniel Jacobus van Schalkwyk

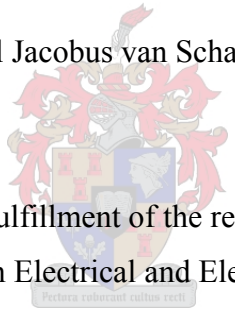

Thesis presented in partial fulfillment of the requirements for the degree of
Master of Science in Electrical and Electronic Engineering
at the University of Stellenbosch

Promoter:
Prof. Maarten J. Kamper, (University of Stellenbosch)

December 2007

Declaration:

I, the undersigned, hereby declare that the work contained in this thesis is my own original work and that I have not previously in its entirety or in part submitted it at any university for a degree.

D.J. Van Schalkwyk

Signature

January 2007
Stellenbosch, South Africa

Abstract

The work presented in this thesis forms part of the participation of the University of Stellenbosch in an electric vehicle project. The thesis deals with three aspects of the dynamics and energy management of the electric vehicle. The three aspects that are dealt with are the suspension system of an electric vehicle with in-wheel propulsion, the traction control of an electric vehicle and the energy system of such a vehicle.

An investigation is presented in the thesis on the effect the mass of the hub motors has on the safety, stability and comfort of the electric vehicle. The investigation is done through a system frequency analysis and a comparative simulation. A comparison is made between a standard vehicle and a vehicle with in-wheel propulsion. A vehicle model is derived for the simulation of the vehicle. Finally, a few of the results of physical measurements performed are also presented.

The traction control requirements of an EV are investigated. A discussion is given on the parts that make up an EV's traction control system. A few examples of possible traction control systems are given through a step by step evolution of a traction control system. A vehicle model is derived for both static and kinetic friction conditions. The model is used in simulations to illustrate the need for traction control in EV's.

The thesis presents two methods for choosing a battery pack size, in terms of energy capacity etc. The difficulties associated with choosing a battery pack, using each of these methods are given. A battery pack choice for the specific electric vehicle, is presented. The measurements of one of the required charge-discharge cycles are presented to illustrate the charge and discharge curves of the battery cells used.

The management of energy flow within the energy system of the EV is crucial, especially if regenerative braking is utilized. This is to protect the battery cells as well as to extend the range of the vehicle. The thesis presents the evaluation of an energy management system (EMS) using ultra capacitors as auxiliary storage device. An electronic load system is designed to simulate the operation of the vehicle motors. The transfer functions for the EMS and load system are derived and used to design the respective control algorithms. The control algorithms were implemented in both simulation as well as a laboratory setup to show the operation of the EMS.

A new energy system configuration is presented. The aim of the new configuration is to solve certain problems encountered when implementing a conventional EMS. The operation of the new configuration is discussed. A comparative study is made between the conventional and the new configurations.

Opsomming

Die werk wat in hierdie tesis voorgelê word is deel van die deelname van die Universiteit van Stellenbosch aan ‘n elektriese voertuig projek. Die tesis handel oor drie aspekte van die dinamika en energie bestuur van die elektriese voertuig. Die drie aspekte wat behandel word is die suspensie stelsel van ‘n wiel-motor aangedrewe elektriese voertuig, die trekkrag-beheer van ‘n elektriese voertuig en die energie-stelsel van so ‘n voertuig.

Die tesis ondersoek die effekte van die massa van die wiel-motors op die veiligheid, stabiliteit en gemak van ‘n elektriese voertuig. Die ondersoek word gedoen deur ‘n stelsel-frekwensie-analise as ook vergelykende simulasies. ‘n Vergelyking word getref tussen ‘n standard voertuig en ‘n wiel-motor aangedrewe voertuig. ‘n Voertuig model is afgelei vir simulasie doeleindes. Laastens word ‘n paar praktiese meetings voorgelê.

Die trekkrag-beheer vereistes van ‘n EV word ondersoek. ‘n Bespreking oor die komponente van ‘n trekkrag-beheer stelsel word gegee. ‘n Paar voorbeelde van trekkrag-beheer stelsels word gegee deur middel van ‘n stap vir stap evolusie van ‘n trekkrag-beheer stelsel. ‘n Voertuig model word afgelei vir beide statiese en kinetiese wiel wrywing. Die model word in simulasie gebruik waar geen trekkrag beheer uitgevoer word nie, om die behoefte aan so ‘n stelsel te illustreer.

Die tesis stel twee metodes voor vir die kies van ‘n battery pak in terme van energy inhoud ens. Die probleme geassosieer met die kies van ‘n battery pak word gegee. ‘n Spesifieke battery pak keuse vir die EV word gegee. ‘n Paar van die meet resultate wat verkry is tydens een van die noodsaaklike laai-ontlaai siklusse word gegee om die laai en ontlaai kurwes van die battery selle wat gebruik is, te illustreer.

‘n Baie belangrike aspek is die bestuur van energie in die energie-stelsel van die EV. Dit is om beide die battery selle te beskerm en om die reikafstand van die voertuig te verleng. Die tesis evalueer ‘n energie-bestuur-stelsel (EBS) wat ultra kapasitore gebruik as sekondêre storingsmeganisme. ‘n Elektroniese las is ontwerp om motors van die voertuig te simuleer. Die oordrag funksies van beide die EBS en die elektroniese las word afgelei en gebruik vir die ontwerp van die onderskeie beheer-algoritmes. Die beheer-algoritmes word geïmplementeer in beide simulasies en in ‘n praktiese opstelling, om die werking daarvan te ondersoek.

‘n Nuwe energie stelsel konfigurasie word voorgelê. Die doel van die nuwe stelsel is om ‘n paar van die probleme wat teëgekom is tydens die implimentering van die konvensionele stelsel op te los. Die werking van die nuwe stelsel word bespreek. ‘n Vergelykende studie word gedoen tussen die konvensionele stelsel en die nuwe stelsel.

Acknowledgements

I would like to express my sincere appreciation to:

- My promoter, Prof. Maarten Kamper, for giving me the opportunity to be part of such a project.
- Optimal Energy Ltd., for their cooperation during the completion of the project.
- My collogues, A.Rix, F. Rossouw and H. de Kock, for their assistance and camaraderie.
- My family for their love and support.
- My Heavenly Farther, for His daily inspiration and strength.

Glossary of symbols and abbreviations

These symbols and abbreviations are in no particular order. In some equations uppercase letters are used – this refers to the steady state.

Chapter 2:

Symbol	Meaning	Unit
M_v	sprung mass	kilograms [kg]
M_s	unsprung mass	kilograms [kg]
B_s	suspension damping coefficient	Newton seconds per metre [Ns/m]
B_t	tyre damping coefficient	Newton seconds per metre [Ns/m]
K_s	suspension spring coefficient	Newton per metre [N/m]
K_t	tyre spring coefficient	Newton per metre [N/m]
F_v	total force acting on vehicle	Newton [N]
F_s	total force acting on wheel	Newton [N]
M	mass matrix	
K	spring constant matrix	
C	damping constant matrix	
$\widetilde{K}$	mass normalized stiffness matrix	
λ_{eig}	system eigenvalues	
$\widetilde{K}_{st}$	$\widetilde{K}$ of standard vehicle	
$\widetilde{K}_{hd}$	$\widetilde{K}$ of hub driven vehicle	
I	identity matrix	
ω_n	natural frequency	radians per second [rad/s]
g	gravity	metre per second squared [m/s^2]

Chapter 3:

Symbol	Meaning	Unit
F_d	traction or driving force	Newton [N]
F_w	rolling resistance	Newton [N]
F_v	aerodynamic drag force	Newton [N]
T_w	applied wheel torque	Newton metre [Nm]
N	normal force	Newton [N]
M_v	vehicle mass	kilograms [kg]
M_w	wheel mass	kilograms [kg]
J_w	wheel moment of inertia	kilogram metre squared [kg/m^2]

K_t	tyre spring coefficient	Newton per metre [N/m]
r_w	wheel radius	metre [m]
σ	incline angle	degrees [°]
ω_w	wheel rotational velocity	radians per second [rad/s]
v_v	vehicle linear velocity	metres per second [m/s]
μ_w	rolling resistance coefficient	
C_d	vehicle friction coefficient	
A_v	equivalent vehicle frontal area	metres squared [m^2]
ρ_{air}	density of air	kilograms per metres cubed [kg/m^3]
v_{cm}	linear velocity of object centre	metres per second [m/s]
a_{cm}	acceleration of object centre	metres per second squared [m/s^2]
μ_s	static friction coefficient	
F_m	force equivalent of vehicle mass	Newton [N]
M_{cm}	moment acting upon object centre	Newton metres [Nm]
μ_a	adhesion coefficient	
λ_{sr}	slip ratio	

Chapter 4:

Symbol	**Meaning**	**Unit**
W_{bat}	energy capability of battery pack	Joule or Watt second [J or Ws]
η_{in}	inverter efficiency	
η_{con}	converter efficiency	
n_m	number of motors	
W_m	energy requirement of motor	Joule or Watt second [J or Ws]
$I_c.h$	current capability of battery cell	Ampere hours [Ah]
V_c	battery cell voltage	Volt [V]
n_c	number of battery cells	
V_{LL}	motor line to line voltage	Volt [V]
V_{LN}	motor phase voltage	Volt [V]
I_L	motor phase current	Ampere [V]
V_{bus}	battery pack and bus voltage	Volt [V]
P_{bat}	battery power	Watt [W]
Φ	power factor angle	Radians [rad]

Chapter 5:

Symbol	Meaning	Unit
ε_0	permittivity of free space	Coulomb squared per Newton metre squared [C^2/Nm^2]
ε_r	relative permittivity of dielectric	
A_p	area of parallel plates	metres squared [m^2]
d	distance between parallel plates	metre [m]
E_{uc}	capacitor energy capacity	Joule or Watt second [J or Ws]
C_{uc}	ultra capacitor capacitance	Farad [F]
n_s	number of series capacitors	
n_p	number of parallel capacitor sets	
V_{uc}	ultra capacitor voltage	Volt [V]
V_{cell}	ultra capacitor cell voltage	Volt [V]
i_{load}	load current	Ampere [A]
i_{bat}	battery current	Ampere [A]
i_{con}	converter current	Ampere [A]
V_{uc_lim}	ultra capacitor voltage limit	Volt [V]
$d(s)$	duty cycle	
d_{lim}	duty cycle limit	
V_{bat}	battery pack nominal voltage	Volt [V]
V_{bus}	bus voltage	Volt [V]
f_s	converter switching frequency	Hertz [Hz]

Abbreviation	Meaning
ICE	internal combustion engine
EV	electric vehicle
BMS	battery management system
SOC	state of charge
2DOF	two degrees of freedom
EMS	energy management system
DLC	double layer capacitor
PI	proportional integral
EMI	electromagnetic interference
EMF	electromagnetic force
FPGA	field programmable gate array
DSP	digital signal processor
IGBT	insulated gate bipolar transistor

Table of Contents

Chapter 1 Introduction

In this chapter background information on electric vehicles and the specific project dealt with in this thesis are given in order to orientate the reader. A summary of some of the questions that are answered by the work presented in the thesis as well as the methods used to answer them are presented.

1.1 Background

The electric vehicle has been around longer than what most people realize. An electric car is often seen as something out of a science fiction movie. In actual fact, the electric car was invented around the middle of the 19th century; at about the same time as the internal combustion engine (ICE) car was invented [1, p1-7]. Electrically- and ICE powered vehicles offered the same performance and furthermore, electric vehicles (EV) were safer and more reliable than ICE vehicles. The Electric Carriage and Wagon Company used electric cars in the first ever automotive passenger transport service [2]. The first ever taxi was an electric car. However, limited range and power of electric cars as well as the rapid design improvements to ICE's led to the rapid decline in the interest in electric cars. They were soon forgotten. For decades, the only electric vehicles that were seen were electric trains and trams with the odd electric milk wagon seen here and there. The ICE powered vehicle had won.

Renewed interest in the electric vehicle was sparked in the last decades of the 20th century. This was due to a few factors, the main ones being oil and the environment. Souring oil prices and a possible oil crisis looming evoked the search for alternative fuels [3]. Also the increase in environmental awareness and the impact that burning of fossil fuels have on the environment meant that alternative fuels had to be environmentally friendly. The world started looking for greener alternatives. The first alternatives were replacing one of the main consumers of oil products, the ICE. Research has been done regarding many alternatives such as bio fuel and hydrogen fuel cells. The search for alternatives brought about the resurrection of the EV.

The Electric Machines Laboratory, a division within the Faculty of Engineering at the University of Stellenbosch, became involved in the development of an electric car. This multi year project entailed the design and testing of a vehicle that would be commercially available to the South African market. The design process encapsulated various aspects of an EV such as the mechanical design of the vehicle, the energy and propulsion systems and the control of the vehicle.

One of the first design decisions that were made was to use in-wheel propulsion instead of a single electric motor with a drive train. Many other research studies have been done on vehicles using in-wheel propulsion [4] [5] [6]. In-wheel propulsion offers a multitude of advantages. Moving the propulsion to the wheels allows for greater freedom when designing the shape and layout of the vehicle. On the other hand, in-wheel propulsion raises a few questions, some of which are answered in this thesis.

Many types of battery technology exist in the world today, each with their own advantages and disadvantages. The most commonly found battery in the automotive industry is probably the lead acid battery. Lead acid batteries are very reliable, but their capabilities and high mass are not sufficient to meet the requirements of an EV fully. This type of battery technology has also reached a peak in its development. A lithium ion battery is considered the best candidate as a storage device for the EV [1, p46] [7]. Although not the best technology available at the moment, Lithium ion battery technology is a very attractive technology for EV applications. Vast improvements have been made in the capabilities of Lithium ion cells and their capabilities will continue to increase in years to come [8].

1.2 Problem statement and approach

This thesis deals with three distinct aspects of an electric vehicle. During the completion of the first year of development of the vehicle, questions concerning certain aspects of the vehicle were raised. These aspects are:

- EV suspension system
- EV traction control
- EV energy system

A. Suspension system

Hub or in-wheel motors have always been considered as propulsion for EV's, but not widely used due to various negative aspects. One of these is the uncertainty of the effect the added wheel mass has on the stability, safety and comfort of the vehicle. This question was when decisions were made on the main design decisions of the vehicle. Moving the propulsion from the vehicle body to the wheel can add up to 60 kg per wheel to the unsprung mass of the vehicle. Most research done on vehicle suspension systems has been done for standard road vehicles [9] [10]. No investigation has been done on vehicles having an unsprung to sprung mass ratio similar to that of the vehicle being developed. A few recommendations state that the unsprung mass should not exceed 20% of the sprung mass, as in current road vehicles. There are no research results to support this statement. There is no evidence to

prove that hub drives are not a viable option due to the increased unsprung mass for vehicle propulsion.

It is the aim of this thesis, in part, to answer the question: is it possible to place the propulsion of an EV in the wheel without having a negative effect on the stability, safety and comfort of the vehicle? This question is studied by means of system frequency analysis and simulation. A model of the vehicle system is derived and used in the study. The simulation results of a hub driven vehicle are compared to those of a standard vehicle to ascertain the effects.

It must be noted that the added mass has an effect on the handling of the vehicle. It is beyond the scope of the thesis to investigate this area, as the model and analyses that are required are extremely complex. It is the opinion of the author that the results obtained from the analysis done in this thesis are sufficient to come to a conclusion on the effect of the increased unsprung mass.

B. Vehicle traction control

Traction control systems are a common occurrence in modern vehicles. A traction control system can be found in a variety of vehicles, from off-road vehicles to high speed sports cars. A traction control system is used to ensure that maximum wheel traction is obtained. Maximum traction ensures maximum acceleration as well as passenger safety. Even anti-lock braking systems, also known as ABS, are a form of traction control.

Traction control systems for EV's are almost as old as for ICE vehicles. The field of electric vehicle traction control is also a well researched field. A fine example was developed by the University of Tokyo [11] [12] [13]. It has been found that all electric vehicles need a traction control system in one form or another. This is due to the nature of electric propulsion. The first reason is that the delay from command to torque on road is significantly shorter in comparison with ICE vehicles, especially when in-wheel propulsion is used. This quickened response leads to uneven acceleration and excessive wheel spin. The second reason is to prevent rotational runaway of the electric motor. It is a characteristic of an electric motor to keep the applied torque the same. If the wheel loses traction, the excessive torque causes the wheel to accelerate uncontrollably. This could lead to motor as well as vehicle damage.

Research has shown that an EV's handling can be vastly improved with the implementation of a complex traction control system. Traction control in EV's does allow for maneuvering that surpasses that of ICE vehicles, especially when in-wheel propulsion is used. [14].

An overview of a traction control system is presented in this thesis. The components of such a system are described. A step by step evolution of a traction control system is given, ranging from the minimal system required to a complex system. A vehicle model is derived for simulation purposes. This model is used in simulations to illustrate the need for a traction control system.

C. Energy System

The main contributors to the high cost associated with an EV, are the energy storage devices such as the batteries. Although Lithium based cells give some of the best performances, they are also one of the most expensive [15, p166-168] [16]. This is due to the fact that the Lithium based technology is still in the improvement phase of its life cycle, unlike lead acid technology that has reached a peak in its improvement. It is predicted that the price of Lithium based cells will decrease significantly in the future. Due to its high cost, it is critically important to determine the optimum battery pack size for the specific application. This is also important from a weight and volume point of view. Two methods for calculating the optimum battery pack size are presented in this thesis. All aspects that influence the size and configuration of the battery pack are mentioned. A few configuration options, using both these methods, are given for the vehicle system being developed. Finally, a battery pack is selected for the vehicle. The results of the first charging and discharging of the cells are also presented.

The performance and use of Lithium based cell technology has a price. The nature of the cells requires controlled voltage and current operation. Lithium cells are intolerant to over-voltage and over-current. Over-voltage and over-current can lead to decreased cell battery performance and even irreversible cell damage. This creates the need for a precise Battery Monitoring System (BMS). A BMS not only monitors the entire battery pack, but each individual cell as well. The BMS can alert the vehicle system to any situation that might damage the cells. In some cases the BMS is developed to take action if these situations arise. These systems are called Battery Management Systems. It is also the function of the BMS to calculate the state of charge (SOC) of the battery pack. The SOC is an indicator of the amount of charge that a battery still has. Complex cell models are used to calculate the SOC. It is these models that make the development of a BMS a field of study on its own [17] [18] [19]. Although the study of a BMS is not dealt with in this thesis, it is used during laboratory testing where Lithium-ion cells are used.

One of the main disadvantages of battery powered vehicles is their limited range in comparison to ICE vehicles. Even with the major advantages in battery technology, the battery will be hard pressed to compete with the specific energy of fossil fuels. It is thus crucially important to save every drop of energy possible. This is why EV designers strive to develop the most efficient systems possible. One of the areas where energy can be reclaimed is during braking; it is possible to return energy to the energy system of the vehicle when electrical braking is used instead of mechanical braking. This is

called regenerative braking. The problem with regenerative braking is the amount of power that is returned to the energy system of the EV. Although offering high specific energy, Lithium based cells have a relatively low specific power. These cells are unable to accept the peak power delivered by regenerative braking without reducing the lifetime of the cells. It must also be remembered that Lithium based cells can deliver more power than what they can receive, without damage, when the electric drives can deliver as much power back into the system, during braking, as it draws during motoring. Fast changes in the rate of power are also detrimental to the cells. This occurs during braking as well as during quick acceleration of the vehicle. Many vehicle systems use a braking resistor to dissipate the excess power returned during braking. Thus, the power is wasted as heat. This waste creates the need for an auxiliary storage unit. The storage device used should have a high specific power. As will be explained, ultra capacitors are ideal as auxiliary storage devices. In this thesis an energy management system is developed using ultra capacitors. The auxiliary storage will serve as a power buffer between the electric motors and the battery pack and so doing extend the life of the cells as well as increasing the range of the vehicle. Many research studies have been done on developing such energy management systems [20] [21] [22]. What makes the system presented in this thesis different to the others is that the energy system of the vehicle was designed to be a low voltage, high current system. This decision has its advantages and disadvantages. These will be pointed out in the thesis. The operation of the energy management system is illustrated. A system model is derived for the purpose of designing the control algorithm and for simulations. A laboratory setup of the energy management system was implemented and the test results are presented.

The conventional system used has a few negative aspects to energy management in an EV. A new configuration is proposed that eliminates some of the disadvantages experienced in the conventional energy system configuration. A new energy system configuration is presented and compared to the conventional configuration.

1.3. Thesis layout

The layout of the remainder of this thesis is as follows:

Chapter 2: The analysis of the effects of the added wheel mass on the stability, safety and comfort of an electric vehicle. A vehicle model is derived and used in a system frequency analysis and simulation.

Chapter 3: The traction control system of an electric vehicle is discussed. Various forms of traction control systems are presented, ranging from a simple to complex system. A vehicle model is derived. Simulation results are presented to illustrate the need for a traction control system.

Chapter 4: Two methods for choosing a battery pack for an electric vehicle are presented.

Chapter 5: The design of a system utilizing ultra capacitors as auxiliary storage device is presented. This system is also known as the vehicle's energy management system. The circuit model and control algorithm are derived. Simulation results and practical measurements of the system are presented.

Chapter 6: A summary is given of the work covered in this thesis as well as conclusions drawn from the results obtained. A few recommendations are made concerning the work presented and possible future research.

Chapter 2 Vehicle suspension analysis

In this chapter the effect of a hub motor's mass on the stability and comfort of electric vehicles is investigated. A simple model is derived and used in the investigation. The investigation takes on the form of a comparative study between a standard vehicle and a hub driven vehicle. From frequency analysis and simulation results, conclusions are drawn on the viability of hub motors as propulsion for electric vehicles.

2.1 Vehicle suspension model

A vehicle model is required for the frequency analysis as well as for simulations. This section describes the derivation of such a model.

2.1.1 Quarter Vehicle Model

The vehicle is modelled using a two-degree-of-freedom (2DOF) system [23]. The number of degrees of freedom of a system is determined by the number of directions in which the parts of a system can move. This is a standard model used in the simulation of suspension systems [9] [10]. The system comprises of two masses suspended by two sets of spring-damper systems. It represents a quarter of the vehicle and hence is called a quarter vehicle suspension model. The advantage of using a 2DOF system is that it gives a simple, but relatively accurate model of the vehicle's mass-suspension system and tyre. The model allows observation of both suspension and tyre deflection under applied road conditions.

Fig 2.1 represents the quarter vehicle suspension model. The masses, M_V and M_S, are the sprung mass and unsprung mass respectively. The suspension and tyre damper coefficients are represented by B_S and B_T. The suspension and tyre spring coefficients are represented by K_S and K_T. The road, unsprung mass and sprung mass displacement are represented by x, y and z respectively.

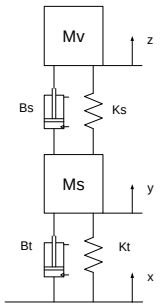

Fig. 2.1: Quarter vehicle suspension model.

The quarter vehicle model has certain shortcomings when it is used as simulation model. Firstly, each quarter of the vehicle is independent from the others. This model does not take the effect of the three other wheels on the fourth as well as the effect of the vehicle body rotating around its rotational centre into consideration. Secondly, the model is a point representation of a body with volume. This makes the model time invariant. Current road contact points have no effect on the system's future response and future road contact points have no effect on the current response. An example of this is the tyre climbing a road curb. The volume of the tyre causes a future contact point to have an effect on the current response. It is the author's opinion that the model has such a high level of accuracy that the required conclusions can be drawn for the study from the obtained results.

As can be seen from Fig. 2.1, the displacement of the sprung mass, the unsprung mass and road surface have different origins relative to each other. By using these reference frames, the displacements y and z can refer to any solidly connected point on the unsprung and sprung mass. Thus the y displacement can be e.g. the edge of the rim or one of the bolts connecting the wheel to the axle. This is the same for the sprung mass displacement z.

2.1.2 Dynamic equations

The next step in deriving a mathematical model for the vehicle suspension system is to obtain the dynamic equations for the system. This is easily done by applying Newton's second law of motion to Fig 2.1 Since there are two bodies, two equations need to be satisfied:

$$M_V \ddot{z} = \sum F_V \tag{2.1}$$

$$M_S \ddot{y} = \sum F_S \tag{2.2}$$

The unknown forces can be found by inspection of Fig 2.1.

(i) Forces acting on sprung mass (F_V):

From Fig. 2.1.1 it can be seen that there are three forces acting on the sprung mass. They are:

Suspension spring force: $F = displacement * K_S = (z - y)K_S$

Suspension damper force: $F = speed * B_S = (\dot{z} - \dot{y})B_S$

Sprung mass: $F = mass * gravity = M_V g$

In the case where z is larger than y; the sprung mass's displacement is larger than that of the unsprung mass; the spring will "pull" down on the sprung mass. Thus the force due to the suspension spring will be negative.

In the case where the time derivative of z is larger than the time derivative of y; velocity of the sprung mass is larger than that of the unsprung mass; the damper will "pull" down on the sprung mass. Thus the force due to the suspension damper will be negative.

There is a force exerted on the sprung mass due to its own weight. As gravity always is in a downward direction, this force is negative.

Thus the total force acting on the sprung mass is:

$$F_V = -K_S(z-y) - B_S(\dot{z}-\dot{y}) - M_V g \qquad (2.3)$$

(ii) Forces acting on unsprung mass (F_S):

From Fig 2.1 it can be seen that there are five forces acting on the unsprung mass. They are:

Suspension spring force: $F = displacement * K_S = (z-y)K_S$

Suspension damper force: $F = speed * B_S = (\dot{z}-\dot{y})B_S$

Tyre spring force: $F = displacement * K_T = (y-z)K_T$

Tyre damper force: $F = speed * B_T = (y-x)B_T$

Unsprung mass: $F = mass * gravity = M_S g$

In the case where z is larger than y; the displacement of the sprung mass is larger than that of the unsprung mass' displacement; the spring will "pull" up on the unsprung mass. Thus the force due to the suspension spring will be positive.

In the case where the time derivative of z is larger than the time derivative of y; the velocity of the sprung mass is larger than the unsprung mass' velocity; the damper will "pull" up on the unsprung mass. Thus the force due to the suspension damper will be positive.

In the case where y is larger than x; the displacement of the unsprung mass is larger than the road displacement; the spring will "pull" down on the unsprung mass. Thus the force due to the tyre spring will be negative.

In the case where the time derivative of y is larger than the time derivative of x; the velocity of the unsprung mass is larger than the change in road condition; the damper will "pull" down on the unsprung mass. Thus the force due to the tyre damper will be negative.

As gravity "pulls" down on the unsprung mass the force due to its mass will be negative.

Thus the total force acting on the unsprung mass is:

$$F_S = K_S(z-y) + B_S(\dot{z}-\dot{y}) - K_T(y-x) - B_T(\dot{y}-\dot{x}) - M_S g \qquad (2.4)$$

If equation 2.3 and 2.4 are substituted into equations 2.1 and 2.2, the dynamic equations for the system are:

$$M_V \ddot{z} = -K_S(z-y) - B_S(\dot{z}-\dot{y}) - M_V g \qquad (2.5)$$

$$M_S \ddot{y} = K_S(z-y) + B_S(\dot{z}-\dot{y}) - K_T(y-x) - B_T(\dot{y}-\dot{x}) - M_S g \qquad (2.6)$$

2.1.3 Wheel hop

A very real phenomenon is that of the tyre losing contact with the road surface, also known as "wheel hop". This phenomenon needs to be taken into account as it could happen during the simulations that the tyre loses contact with the road due to either fast changing road conditions or the instability of the suspension system.

The last point of contact between the tyre and the road surface occurs when the unsprung mass and the road surface are equally displaced from their respective origins i.e. **y-x=0**. The forces due to the tyre spring and damper are only exerted when the wheel is in contact with the road surface. Incorporating wheel hop into the dynamic equations, equation 2.6 becomes:

$$M_S \ddot{y} = K_S(z-y) + B_S(\dot{z}-\dot{y}) - K_T(y-x) - B_T(\dot{y}-\dot{x}) - M_S g \quad \text{if } (y\text{-}x) \geq 0$$

$$M_S \ddot{y} = K_S(z-y) + B_S(\dot{z}-\dot{y}) - M_S g \quad \text{if } (y\text{-}x) \leq 0 \qquad (2.7)$$

2.1.4 Vehicle Parameters

Two vehicles are compared in the study. One is a standard vehicle and the other a vehicle with hub drives placed in each wheel. The same total mass i.e. sprung and unsprung mass combined, is used for both vehicles. A total mass of 1500 kg was chosen. This is the mass of a fully laden vehicle (vehicle mass, passengers and payload). The standard vehicle will serve as the control for the study and the hub driven vehicle as the experiment. The comparison of the hub driven vehicle to a standard vehicle will indicate to what extent the shift in mass affects the system.

All constants used such as damping and spring coefficients are kept the same for both vehicles. As the model used during this study represents a quarter of the vehicle, all masses are divided by four. Table 2.1 lists the values used in the study.

	Standard Vehicle		Hub Driven Vehicle	
	Total	Model	Total	Model
Total Mass	1500kg	375kg	1500kg	375kg
Sprung Mass	1340kg	335kg	1100kg	275kg
Unsprung Mass	160kg	40kg	400kg	100kg
Ks	36000 N/m	36000 N/m	36000 N/m	36000 N/m
Bs	3000 Ns/m	3000 Ns/m	3000 Ns/m	3000 Ns/m
Kt	110000 N/m	110000 N/m	110000 N/m	110000 N/m
Bt	200 Ns/m	200 Ns/m	200 Ns/m	200 Ns/m

Table 2.1.1: Vehicle parameters

2.2 Frequency Analysis

It is important to verify that the suspension system and thus the vehicle are stable under changing road surface conditions. The frequency response of a system can give a clear indication of the stability of that system. The simplest method of investigating the frequency response stability of the system is to do an analysis on the system's Bode plot.

A second aspect to investigate is the natural frequency or frequencies of the system. The natural frequency of the system affects the frequency at which maximum oscillation amplitude occurs. This frequency is important to note when investigating how comfortable a vehicle is to drive. The human body is sensitive to certain frequencies of vibrations. Prolonged exposure to these vibrations causes discomfort and even injury. The natural frequency can easily be calculated from the simulation model.

2.2.1 Bode plot analysis

A Bode plot analysis is the simplest way to determine if a system will have a stable frequency response or not. It is important that the suspension system of a vehicle have a bounded frequency response.

The transfer function is required to obtain the Bode-plot of the system. The transfer function can be mathematically derived from the dynamic equations or extracted from the linear model using MatLab.

From MatLab the transfer function for the standard vehicle system is given as

$$\text{Standard vehicle: } G(s)_S = \frac{8.527e-14s^3 + 4.093e-12s^2 + 2.463e4s + 2.955e5}{s^4 + 88.96s^3 + 3802s^2 + 2.516e4s + 2.955e5} \quad (2.8)$$

and for the hub driven vehicle as

$$\text{Hub driven vehicle: } G(s)_{HD} = \frac{6.395e-14s^3 + 3.638e-12s^2 + 1.2e4s + 1.44e5}{s^4 + 42.91s^3 + 1613s^2 + 1.226e4s + 1.44e5} \quad (2.9)$$

The transfer function can give an indication of the stability of the system. Both transfer functions have higher order poles than zeros. It can be seen that the second and third order zeros are small in comparison with the rest. This is a good indication that the systems are stable. It is still good practice to do a Bode plot analysis to comment on the stability of the systems. Fig 2.2 shows the Bode plots for both the standard and hub driven vehicles.

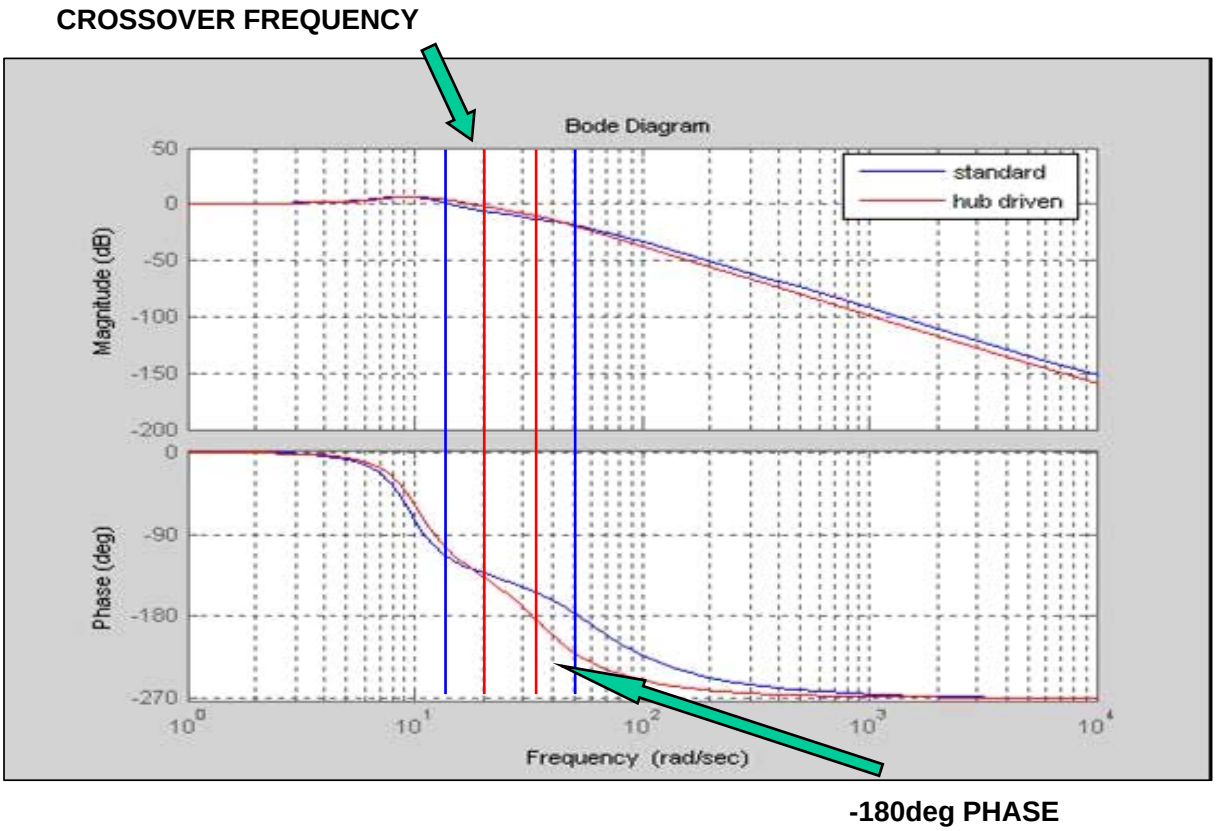

Fig. 2.2: Bode plot of standard and hub driven vehicles.

A system is said to be unstable if it has a phase of -180 degrees at its crossover frequency. A system could also possibly be unstable if the magnitude is larger than 1 dB when the phase is equal to -180 degrees. The crossover frequencies and -180 degree phase points are marked on Fig 2.2. From Fig. 2.2 and Table 2.2 it can be seen that the standard and hub driven vehicle do not meet the instability criteria and are thus stable.

The dominant natural frequency of the system can easily be seen from the Bode-plot. This frequency is where the Bode-plot reaches a maximum. As both systems are 2DOF systems, two natural frequencies occur. The first or lower frequency will be the dominant natural frequency, with the higher second frequency being the damped natural frequency. The damped natural frequency is difficult to distinguish, but can be found by looking at the shape of the Bode-plot. The natural frequency can be calculated more accurately.

	Standard Vehicle	Hub Driven Vehicle
First Natural Frequency	9 rad/s	10 rad/s
Second Natural Frequency	60 rad/s	40 rad/s
Crossover Frequency	15 rad/s	18 rad/s
-180 deg Frequency	52 rad/s	33 rad/s
Magnitude at Natural Frequency	7dB	7.5 dB

Table 2.2: Bode plot information.

Something to note is that the two natural frequencies move closer together as the mass is shifted from the body to the wheels. When the natural frequencies are far apart the second is extremely damped and plays virtually no part in the oscillation of the system. As the two move closer together, the second frequency starts playing a larger role. The two frequencies could move so close together, super positioning on each other, causing larger and unwanted oscillations.

2.2.2 Natural Frequency

The natural frequency of a system is the frequency at which the driving force should be to cause the system to have maximum or unbounded oscillations. The system thus resonates at its natural frequency. In multiple-degree-of freedom systems, the system has ***n*** natural frequencies. It is possible that the system resonates at all, some or none of its natural frequencies. Most multiple-degree-of-freedom systems only experience damped oscillation with maximum amplitude at their natural frequency.

The natural frequency of a system is calculated from information obtained from the dynamic equations. The dynamic equations should be in matrix form to do so. The matrix form of the dynamic equations is obtained by combining equations 2.5 and 2.6. This can be found in Appendix A as equation A.1. To simplify the equations the following substitutions were made:

$$x = w$$
$$y = x_1$$
$$z = x_2$$

The dynamic equations in matrix form become:

$$\begin{bmatrix} M_S & 0 \\ 0 & M_V \end{bmatrix}\begin{bmatrix} \ddot{x}_1 \\ \ddot{x}_2 \end{bmatrix}+\begin{bmatrix} (B_S+B_T) & -B_S \\ -B_S & B_S \end{bmatrix}\begin{bmatrix} \dot{x}_1 \\ \dot{x}_2 \end{bmatrix}+\begin{bmatrix} (K_S+K_T) & -K_S \\ -K_S & K_S \end{bmatrix}\begin{bmatrix} x_1 \\ x_2 \end{bmatrix}=\begin{bmatrix} K_T \\ 0 \end{bmatrix}\begin{bmatrix} w_1 \\ w_2 \end{bmatrix}+\begin{bmatrix} -B_T \\ 0 \end{bmatrix}\begin{bmatrix} \dot{w}_1 \\ \dot{w}_2 \end{bmatrix}-\begin{bmatrix} M_S g \\ M_V g \end{bmatrix}$$

The following matrices are needed when calculating the natural frequencies of the systems can be extracted from the above equation:

Mass matrix: $$M = \begin{bmatrix} M_S & 0 \\ 0 & M_V \end{bmatrix}$$

Spring constant matrix: $$K = \begin{bmatrix} K_S + K_T & -K_S \\ -K_S & K_S \end{bmatrix}$$

Damping spring matrix: $$C = \begin{bmatrix} B_S + B_T & -B_S \\ -B_S & B_S \end{bmatrix}$$

These matrices are used to calculate the mass normalized stiffness matrix. The natural frequency of the system is given as the square root of the eigenvalues of the mass normalized stiffness matrix. The mass normalized stiffness matrix is given by:

$$\widetilde{K} = M^{\frac{1}{2}} K M^{-\frac{1}{2}} = \begin{bmatrix} \dfrac{K_S + K_T}{M_S} & -\dfrac{K_S}{\sqrt{M_S M_V}} \\ -\dfrac{K_S}{\sqrt{M_S M_V}} & \dfrac{K_S}{M_V} \end{bmatrix} \qquad (2.10)$$

The calculation of the mass normalized stiffness matrix is given in Appendix A as equations A.2.

As the system is a 2DOF system the matrix $\widetilde{K}$ will have two eigenvalues and thus two natural frequencies, as can be seen from the Bode-plot in the previous section. The eigenvalues for the mass normalized stiffness matrix are calculated by solving the following equation:

$$\det\left(\widetilde{K} - \lambda_{eig} I\right) = 0 \tag{2.11}$$

The equations for the eigenvalues of the mass normalized matrix as given in Appendix A as equations A.3 and A.4 are:

$$\lambda_1 = \frac{1}{2}\left[\left(\frac{K_S + K_T}{M_S}\right) - \sqrt{\left(\frac{K_S + K_T}{M_S} + \frac{K_S}{M_V}\right)^2 - 4\left(\frac{K_S K_T}{M_S M_V}\right)}\right] \tag{2.12}$$

$$\lambda_2 = \frac{1}{2}\left[\left(\frac{K_S + K_T}{M_S}\right) + \sqrt{\left(\frac{K_S + K_T}{M_S} + \frac{K_S}{M_V}\right)^2 - 4\left(\frac{K_S K_T}{M_S M_V}\right)}\right] \tag{2.13}$$

If the vehicle parameters are substituted into equations 2.12 and 2.13, the eigenvalues are calculated as:

Standard vehicle: $\lambda_1 = 80.368$

$\lambda_2 = 3677.091$

Hun driven vehicle: $\lambda_1 = 96.349$

$\lambda_2 = 1494.561$

From the eigenvalues the natural frequencies of the systems are calculated as:

Standard vehicle: $\omega_{n1} = \sqrt{80.368} = 8.96$ rad/s or 1.43 Hz

$\omega_{n2} = \sqrt{3677.091} = 60.639$ rad/s or 9.65 Hz

Hub driven vehicle: $\omega_{n1} = \sqrt{96.349} = 9.82$ rad/s or 1.56 Hz

$\omega_{n2} = \sqrt{1494.561} = 38.56$ rad/s or 6.15 Hz

The natural frequencies obtained from the Bode plot can be compared with those of the calculated values. Table 2.3 (on next page) lists the Bode plot as well as the calculated values. It can be seen that the Bode plot values compare well with the calculated values. The margin of error made through inspection is very slight.

	Standard Vehicle	
	Bode plot	Calculated
First Natural Frequency	9 rad/s	8.96 rad/s
Second Natural Frequency	60 rad/s	60.639 rad/s
	Hub Driven Vehicle	
	Bode plot	Calculated
First Natural Frequency	10 rad/s	9.82 rad/s
Second Natural Frequency	40 rad/s	38.659 rad/s

Table 2.3: Comparative frequency information.

In 2DOF systems the second or higher natural frequency is neglected in the frequency analysis of the system as the second frequency is extremely damped and will have no effect on the vibrations perceived by the occupants of the vehicle. This fact was shown to be true in the Bode plot analysis.

Different parts of the human body are sensitive to different frequency ranges. The vehicle will be classified as uncomfortable if the dominant natural frequency falls within these ranges. It has been found that a frequency between 0.5 to 1 Hz causes a high occurrence of motion sickness. The human head and neck are especially sensitive to vibrations between 18 and 20 Hz. The abdomen region of the body is sensitive to vibrations between 5 and 7 Hz, and the spine from 7 to about 12 Hz. Although there might be a slight difference from person to person, it is safe to state that these are the unwanted frequency ranges. Prolonged exposure to these frequencies is not only uncomfortable but could cause injury to the occupants of the vehicle. Research has also shown that a system with a natural frequency higher than 3 Hz is perceived as a 'harsh ride' by humans. A ride is considered to be comfortable if it has a natural frequency near the 1.5 Hz mark. Fig 2.3 illustrates these frequency ranges.

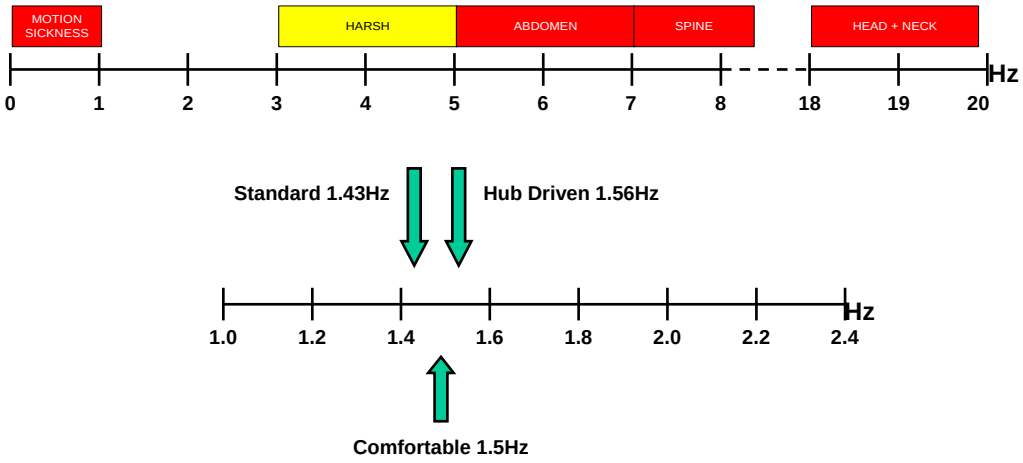

Fig 2.3: Comfort frequency range.

Taking these mentioned frequency ranges into account; it is safe to stipulate a guideline stating that a safe and comfortable system would have a dominant natural frequency between 1 and 3 Hz. It can be seen that the calculated frequencies fall within this ranges. Furthermore they are close to 1.5 Hz which is perceived as the optimum natural frequency.

2.2.3 Payload Analysis

The analysis in the previous sections was done on the suspension system of a fully loaded standard and hub driven vehicle. The total mass used was the sum of the vehicle's curb weight and a payload. A vehicle's curb weight is defined as the weight of the vehicle when it is fully operational plus one passenger. An electric vehicle's curb weight is generally lower than that of a standard vehicle, as is used in this section. The next step is to investigate what effect a varying payload has on the natural frequencies of the system. The payload of a vehicle can range from empty to full load. The curb weights for a standard and hub driven vehicle are chosen as 900 kg and 750 kg respectively.

As seen in a previous section, the best indicator of a system's response is its natural frequency. Firstly, the dominant natural frequency gives an indication of the safety and comfort of the vehicle and secondly, the distance between the two natural frequencies gives an indication on the stability of the vehicle.

Fig 2.4 shows the dominant natural frequency for both the standard and hub-driven vehicles for the range of payloads. The natural frequencies are calculated by means of the equations derived in Section 2.2.2.

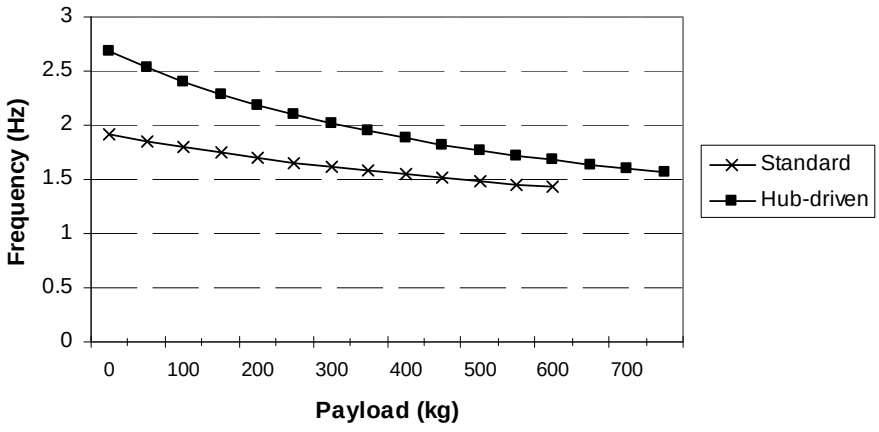

Fig 2.4: Dominant natural frequency of standard and hub driven vehicle.

The varying payload has little effect on the natural frequencies of the standard vehicle and stays within the 1 to 3 Hz range. This can be ascribed to the fact that the suspension system was specially designed for the standard vehicle. On the other hand, the varying payload causes significant variation in the natural frequency of the hub-driven vehicle. The hub-driven vehicle will have slightly different responses depending on the size of the payload. The natural frequency of the hub-driven vehicle is still within the comfort range of 1 to 3 Hz.

The stability of the vehicle systems can be verified by examining the distance between the dominant and damped natural frequencies of the systems. As seen in Section 2.2.1, the two natural frequencies move closer together as mass is shifted from the sprung to the unsprung mass of the vehicle. Taking this fact into consideration, it seems that the empty hub-driven vehicle runs the greater risk of being unstable. Fig 2.5 gives both natural frequencies of the hub-driven vehicle for various loads. These frequencies are still far enough apart so as not to cause instability in the system. This has been verified by doing both a Bode and Nyquist analysis of the empty vehicle system.

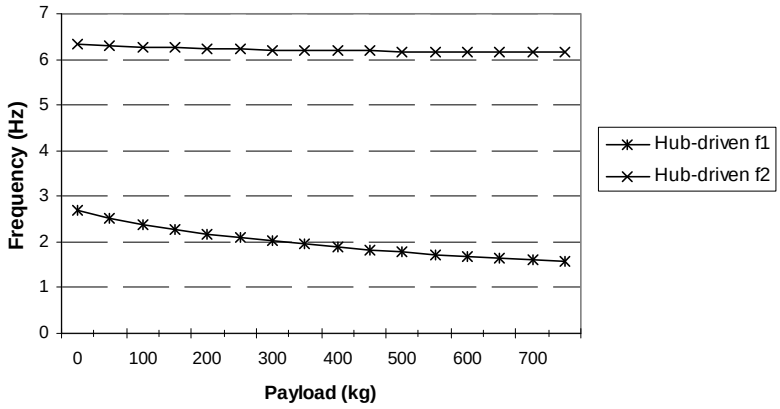

Fig 2.5: Natural frequencies of the hub driven vehicle for various payloads.

2.3 Simulation results

It is important to investigate the time domain response of the two systems. The simulation results for the standard and hub driven vehicles are compared to come to the necessary conclusions on the effect of the added wheel mass. Simulations are done using a model implemented in MatLab/Simulink. The simulation model is the dynamic equations of the systems implemented in block diagram form. The vehicle parameters used in the previous section are also used in the simulation model. These are imported into the model using a MatLab M-file.

2.3.1 Simulation model

Before the model is implemented in MatLab/Simulink, the dynamic equations are rewritten in integral form to simplify creating the block diagram. The dynamic equations in integral form are:

$$y = \iint \frac{1}{M_S}\left[K_S(z-y) + B_S(\dot{z}-\dot{y}) - K_T(y-x) - B_T(\dot{y}-\dot{x}) - M_S g\right]dt \qquad (2.14)$$

$$z = \iint \frac{1}{M_V}\left[-K_S(z-y) - B_S(\dot{z}-\dot{y}) - M_V g\right]dt \qquad (2.15)$$

The block diagram is derived from the dynamic equations in integral form. Fig 2.6 and 2.7 show the block diagrams of equations 2.14 and 2.15 respectively.

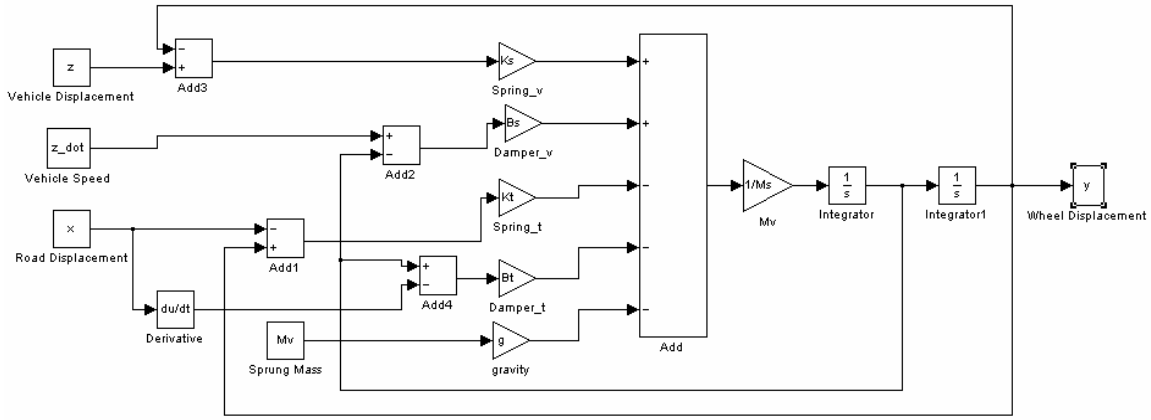

Fig 2.6: Block diagram of equation 2.14.

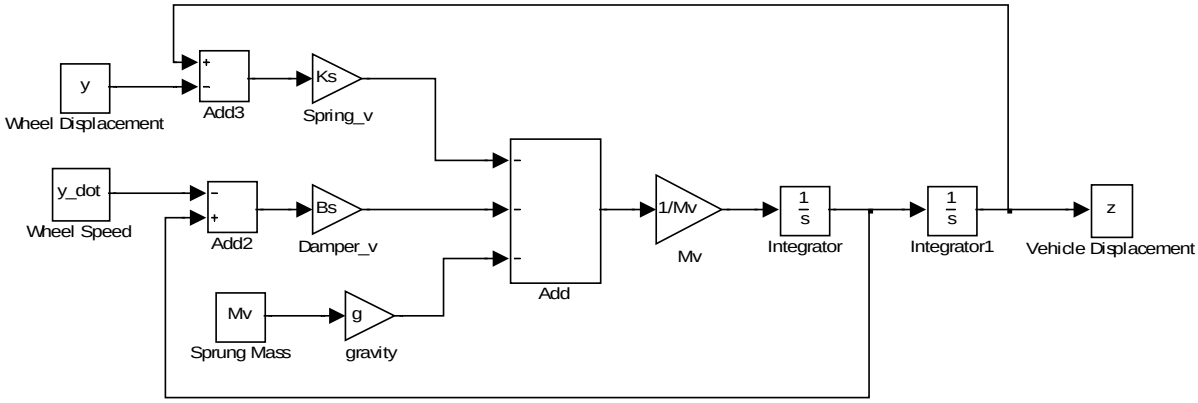

Fig 2.7: Block diagram of equation 2.15.

The wheel hop phenomenon is implemented with the use of a rational operator block. The rational operator block performs the check to verify if the wheel is still in contact with the road surface. The output of the rational operator is multiplied with the tyre forces. As stated before, the wheel loses contact with the road surface when the wheel's displacement is more than the road's displacement i.e. $(y-x) \geq 0$. When the wheel is in contact with the road when $(y-x) \leq 0$. The rational operator outputs a "1" when this is true and a "0" when false. Thus the tyre forces are only added while $(y-x) \leq 0$. Fig 2.8 shows the block diagram of the wheel hop check.

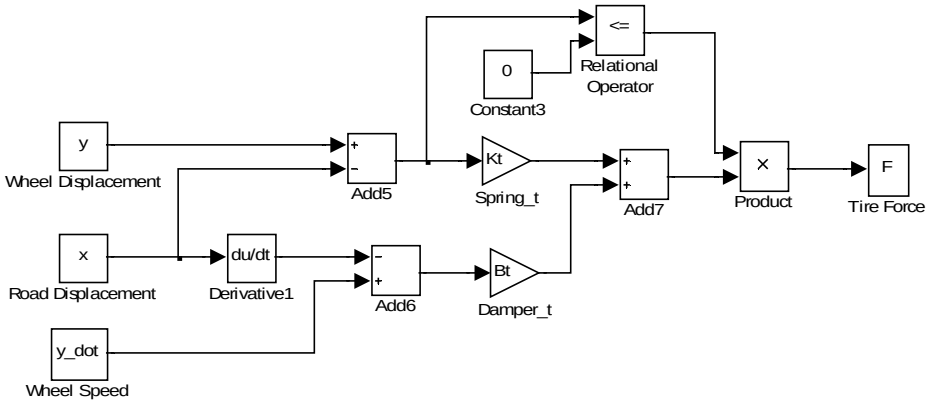

Fig 2.8: Block diagram implementation of "wheel hop".

The three block diagrams from Fig 2.6, 2.7 and 2.8 are combined to form the block diagram model of the system. Fig 2.9 shows the full block diagram.

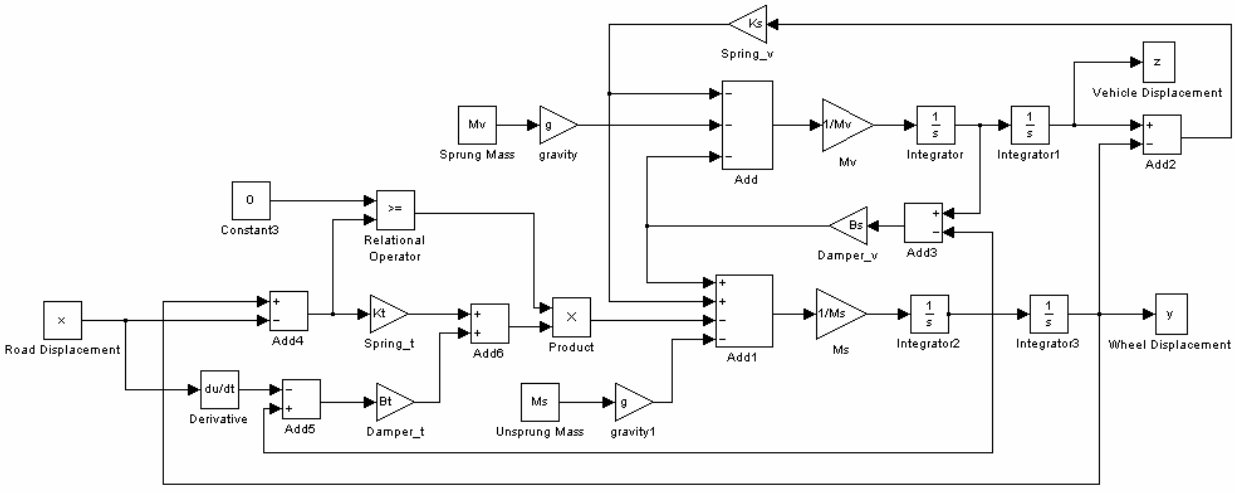

Fig 2.9: Block diagram model of the vehicle mass-suspension system.

2.3.2 Static Deflection

The simulation model shown in Fig. 2.9 takes static deflection of the suspension and tyre into account. This is physically observed as the suspension and tyre sag under the weight of the vehicle. Both masses will thus have a negative displacement at equilibrium. Some models compensate for this by either adding pre-stress forces to the weight of the vehicle or removing the weight from the model. As the investigation is to determine what effect the changes in mass have on the system, no static deflection compensation should be done. It is thus important to allow the simulation to reach equilibrium before any road input is given.

The static deflection points of the simulation were verified by comparing them with those of an actual vehicle. The actual vehicle has a mass of 1100 kg. The vehicle parameters were changed to match the actual vehicle's parameters.

From measurements the static deflection points of the sprung and unsprung mass of an actual vehicle were 0.087 m and 0.023 m respectively. Fig 2.10 shows the simulation static deflection points to be 0.091 m and 0.025 m. This error can be attributed to inaccuracies in the spring and damper coefficients. It is the author's opinion that the margin of error is acceptable and that the model will deliver useful results.

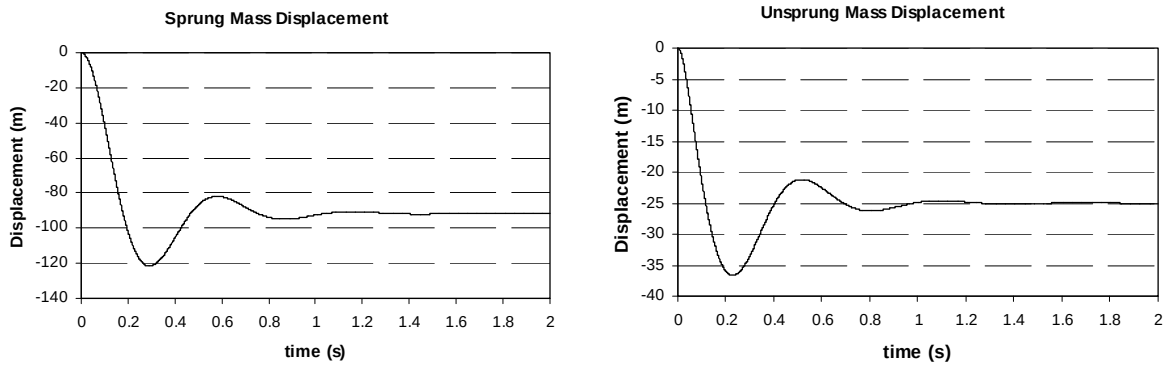

Fig 2.10: Simulation results of static deflection of actual vehicle.

A few observations can be made from the static deflection of the standard vehicle and hub driven vehicle. These are shown in Fig 2.11. It can be seen that the hub driven vehicle reaches equilibrium more quickly than the standard vehicle. Secondly it can be seen that the displacement of the standard vehicle's sprung mass is more than that of the hub driven vehicle, although the unsprung mass displacement is the same. Both these are attributed to the shift in mass. With a smaller sprung mass, less suspension compression takes places. This reduced suspension compression will be seen in all of the simulation results. Fig 2.11 shows that a period of 3 seconds is enough time for the system to reach equilibrium before any road inputs are given.

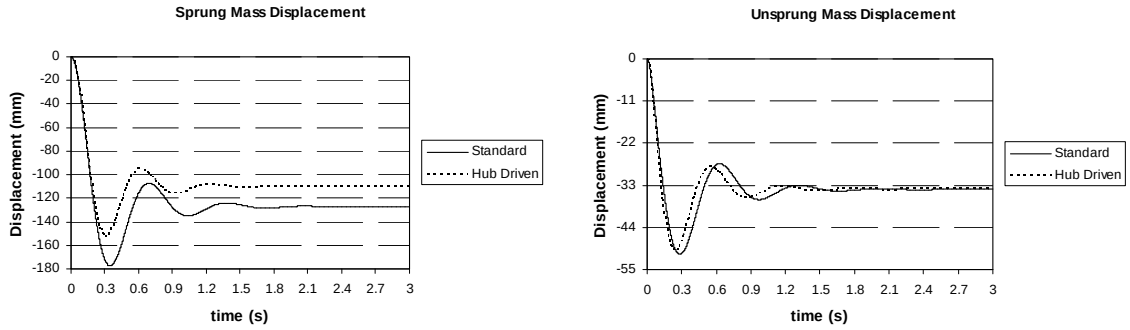

Fig 2.11: Static deflection of standard and hub driven vehicles

2.3.3 Step response

The drop test is a standard test used to measure the damping as well as the oscillation frequency of a physical vehicle's suspension system. The procedure involves giving the system the equivalent of a step input. The drop test thus physically measures the step response of a vehicle's suspension system. The standard height used in industry is 0.08 m. In practical tests a vehicle can either be driven off a 0.08 m high ledge or dropped from a height of 0.08 m. A simulated drop test is done by giving the system a step input with a start value of 0.08 and an end value of 0.

Fig 2.12 shows the displacement of the sprung and unsprung mass of the standard and hub driven vehicles. There are no major differences in displacement of the standard and hub driven vehicle's unsprung mass. The only occurrence worth noting is the peak of the first oscillation of the hub driven vehicle's unsprung mass displacement. The hub driven vehicle's has a larger displacement in the first oscillation than the standard vehicle. The upward force, i.e. force due to the compressed tyre, exerted on the unsprung mass is equal for the standard and hub driven vehicles. The hub driven vehicle's unsprung mass has less upward acceleration due to its having a larger inertia. Thus, the hub driven vehicle's wheel has a longer stopping distance and thus a larger first oscillation.

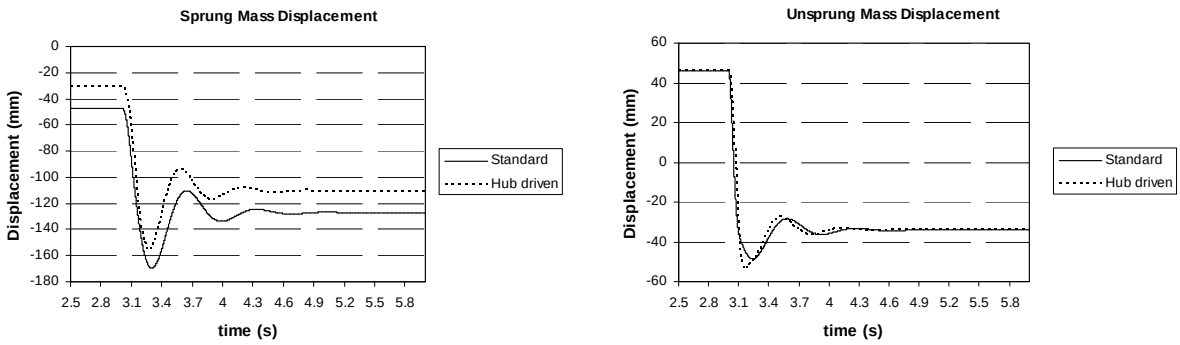

Fig 2.12: Step response comparison of standard and hub driven vehicles.

Fig 2.13 shows the output of the rational operator and thus the occurrence of the wheel hop phenomenon during the drop test. It can be seen that the standard vehicle regains contact with the road surface more quickly than that the hub driven vehicle. The function of a vehicle's suspension system, when it was first invented, was to exert a force on the unsprung mass and keep it in contact with the road surface, and not for comfort. The hub driven vehicle's suspension experiences less compression due to the fact that the sprung mass is less in comparison with that of the standard vehicle. The suspension exerts less force on the unsprung mass. The hub driven vehicle's unsprung mass has less downward acceleration than that of the standard vehicle and thus takes longer to regain contact with the road surface. A dramatic increase in this time results in the deterioration of the vehicle's handling. It is the author's opinion that this increase; 0.015 seconds; is so slight that no difference in handling due to this increase will be felt by the driver.

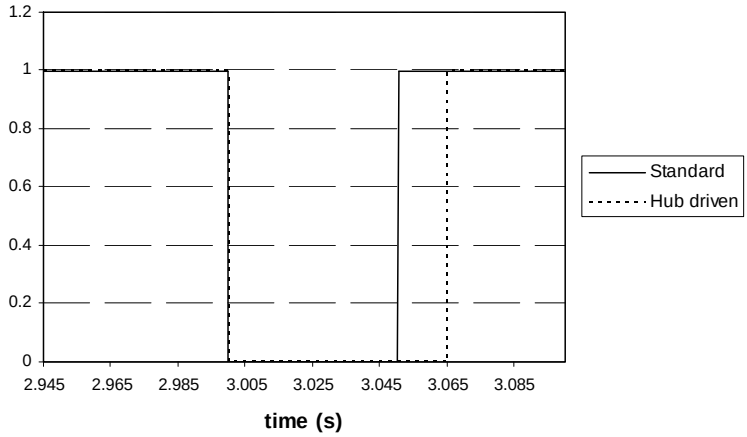

Fig 2.13: Rational operator output showing duration of "wheel hop".

2.3.4 Road surface simulation

In the following section the system's response to changing road surfaces are investigated. This is done for both single and multiple bumps as road surface inputs. These simulations are done at various speeds. The speeds chosen are 5, 50 and 100 km/h. The vehicle speed is important in that it determines the time it takes the wheel to cross the bump. As the crossing time is decreased so is the frequency content of the road surface increased. The bump appears sharper and approaches an impulse.

Fig 2.14 shows the same bump at various speeds. It can be observed that as the speed increases so the crossing time decreases. The road data is calculated in the same M-file used to import the system constants. This allows any shape or number of bumps to be imported into the simulation. Cosine bumps were used to investigate the system's response to a single input frequency.

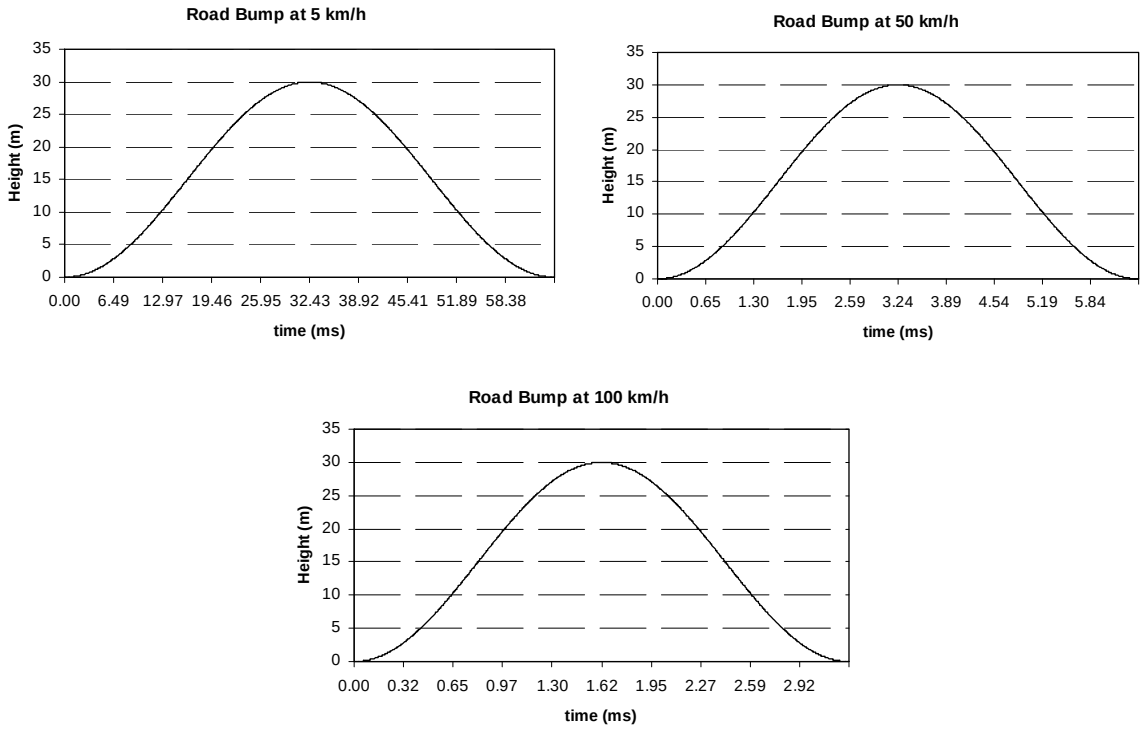

Fig 2.14: Bump crossing times at various speeds.

A. Single bump response

In this section the response of the hub driven vehicle system to a single road bump is compared to that of the standard vehicle. The bump used as input has the following dimensions: 0.03 m high and 0.09 m wide. The bump is introduced at 3 seconds to allow for static deflection. Fig 2.15 (on the next page) shows the single bump simulation results.

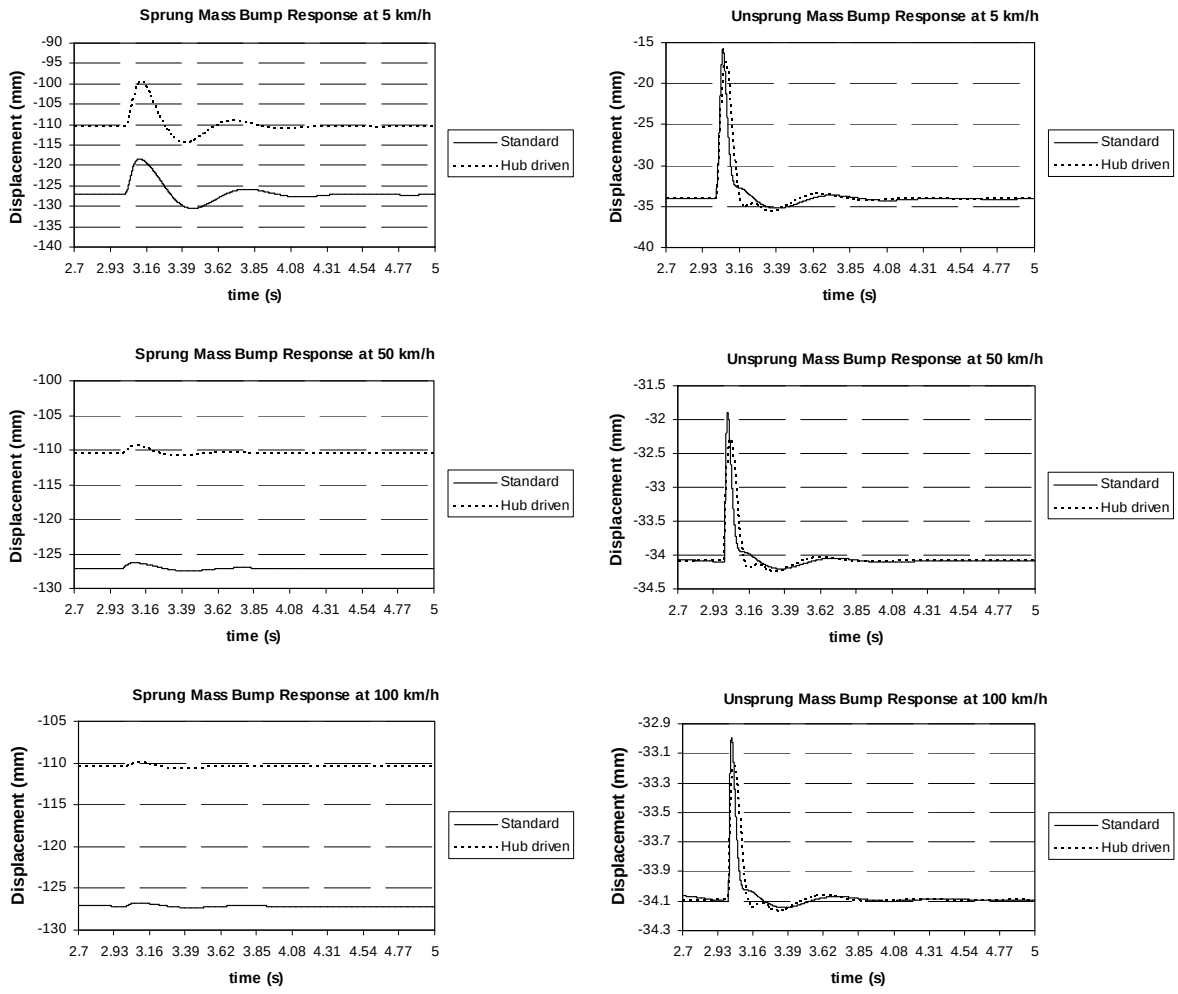

Fig 2.15: Single bump simulation results.

As can be seen, the systems are stable at the simulated speeds and no unwanted oscillations occur. Fig 2.15 shows that the amount of displacement experienced by both the sprung and unsprung mass of the hub driven vehicle as well as the standard vehicle decreases with an increase in speed. It can be seen that the sprung mass of the hub driven vehicle and that of standard vehicle have almost the same displacement apart from their static deflection. On the other hand, the unsprung mass of the hub driven vehicle undergoes less displacement than that of the standard vehicle. This is due to the increase in unsprung mass.

If the sprung and unsprung mass, are both studied, it can be seen that there is a decrease in displacement with an increase in vehicle speed. This is due to the fact that an increase in speed increases the frequency content of the bump. The input frequency moves further away from the natural frequency of the system. This means that more of the bump is absorbed by the tyre and it undergoes more compression. This increase in tyre compression could lead to increased tyre wear. If the tyre compression is large, can be of such an extent that rim damage could also occur. This compression is

not significantly higher for the hub driven vehicle than for the standard vehicle. The danger of wheel damage is not significantly increased for the hub driven vehicle.

Overall, when the hub driven vehicle is compared to the standard vehicle, no major differences are found in the displacement of the masses.

B. Multiple bump response

The next step in the study is to investigate the response of the two systems to multiple bumps and harmonic road surfaces. These are implemented by using a series of the bumps used in the single bump simulation. Thus, a series of the 0.03 m x 0.09 m bumps are connected together. The first bump is introduced at 3 seconds to allow for static deflection. Fig 2.16 shows the simulation results at the various speeds i.e. 5, 50 and 100 km/h.

The introduction of a series of bumps causes vibrations in the displacement of both the sprung and unsprung mass. The unsprung mass experiences more vibrations than the sprung mass. It is interesting to note that although the frequency of the vibrations are the same for the two vehicles, the amplitude of the vibrations experienced by the hub driven vehicle is smaller than that of the standard vehicle. Thus the tyre compression is higher for the hub driven vehicle than for the standard vehicle. As mentioned, this could lead to higher tyre wear and even rim damage.

As mentioned there is a decrease in the response amplitude of the two systems as the speed increases. This is an interesting observation as the systems' response to the series of bumps starts to resemble that of a step response at high speed. At high speed the system seems to 'glide' across the bumps. This is again due to the fact that the input frequency increases with an increase in speed and moves away from the system natural frequency.

The system was monitored for the "wheel hop" phenomenon. None of the above simulations presented "wheel hop". It was found that extreme road inputs are required for "wheel hop" to occur.

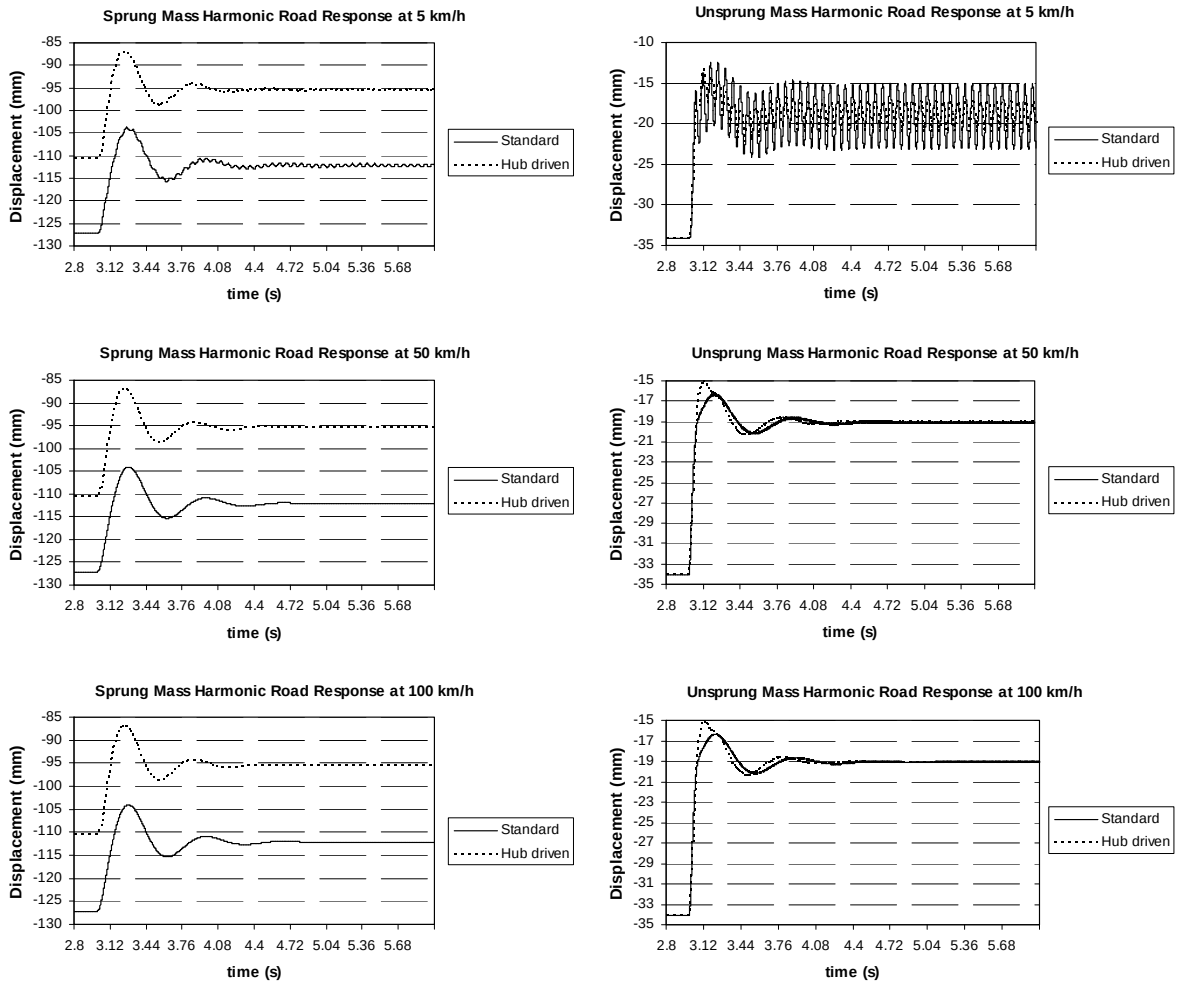

Fig 2.16: Multiple bump simulation results.

2.3.5 Unsprung mass force analysis

Standard vehicle wheels are rigid structures able to absorb high shock and vibration forces without sustaining any damage. By using hub motors, a critical system is placed within the wheels of the vehicle. It is important to determine the magnitude of the forces exerted on the unsprung mass. If these forces are too high and are transferred through the motor, this could lead to quicker wearing of components or even damage of the motor. The forces are presented for both single and multiple bumps road inputs as seen in Fig 2.17 and 2.18 respectively. Table 2.4 lists the initial shock force exerted on the unsprung mass during the single bump simulation as it strikes the bump. Table 2.4 and 2.6 list the initial shock force exerted on the unsprung mass during the multiple bump simulation as well as the maximum amplitude and frequency of the vibration force.

Speed	Standard		Hub driven	
	Tyre Force	Suspension Force	Tyre Force	Suspension Force
5 km/h	6305 N	5296 N	6620 N	4170 N
50 km/h	8715 N	4191 N	8740 N	3120 N
100 km/h	11452 N	3990 N	11466 N	3017 N

Table 2.4: Initial force exerted on unsprung mass (single bump).

Speed	Standard		Hub driven	
	Tyre Force	Suspension Force	Tyre Force	Suspension Force
5 km/h	6323 N	5293 N	6655 N	4162 N
50 km/h	8802 N	4660 N	8945 N	3670 N
100 km/h	11585 N	4635 N	11600 N	3660 N

Table 2.5: Initial forces exerted on unsprung mass (multiple bumps).

Speed	Standard				Hub driven			
	Tyre Force		Suspension Force		Tyre Force		Suspension Force	
	Maximum	Frequency	Maximum	Frequency	Maximum	Frequency	Maximum	Frequency
5 km/h	5650 N	15.13 Hz	4520 N	15.46 Hz	5650 N	15.63 Hz	3300 N	15.58 Hz
50 km/h	7360 N	153.85 Hz	3602 N	153.85 Hz	7300 N	149.25 Hz	2852 N	151.52 Hz
100 km/h	10100 N	303.03 Hz	3570 N	312.5 Hz	10050 N	303.03 Hz	2836 N	303.03 Hz

Table 2.6: Maximum amplitude and frequency of vibration forces (multiple bumps).

As can be seen from Fig 2.17, the force that the tyre exerts on the unsprung mass when it hits the bump is almost equal for the standard and hub driven vehicles. The two show slight deviation at low speed becoming indistinguishable at high speed. An interesting phenomenon to observe is the change in the shape of the suspension force plot as the speed increases. It loses its second oscillation as the vehicle speed increases.

An added advantage found in the analysis is that the suspension of the hub driven vehicle exerts less force than that of the standard vehicle. This is due to the decrease in sprung mass. The benefit of the decreased suspension force is that less suspension compression takes place. This leads to decreased suspension wear.

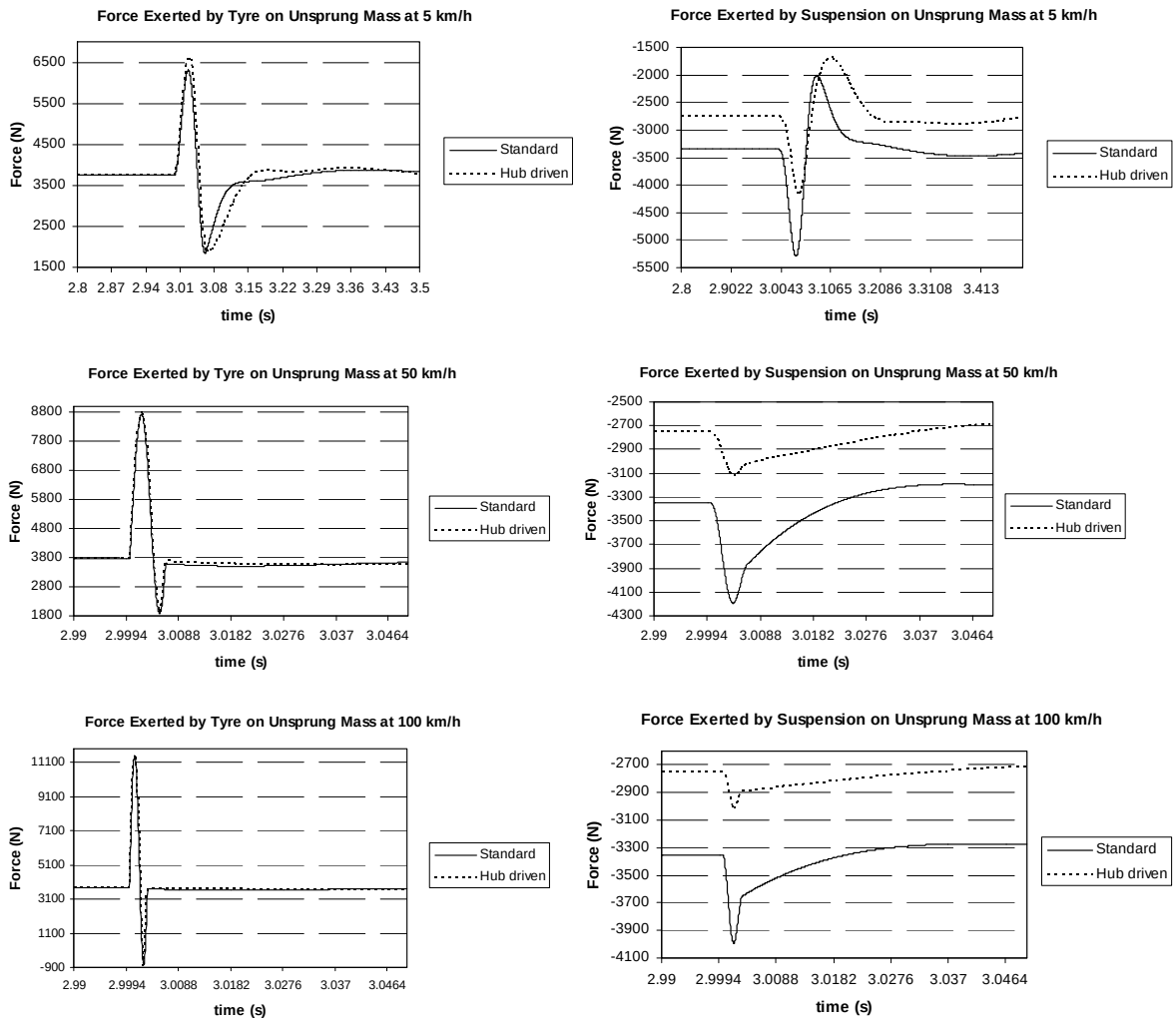

Fig 2.17: Forces exerted on unsprung mass (single bump).

Fig 2.18 shows the forces exerted by the tyre and suspension system on the unsprung mass for multiple bumps. The unsprung mass receives an initial shock force when the tyre hits the first of the bumps. It can be seen that the initial force or first oscillations are higher than the vibration force amplitude. It has the same magnitude as for the single bump simulation. After the initial force, the unsprung mass experiences the vibrations caused by traveling across the series of bumps. It can be seen that the force exerted by the tyre on the unsprung mass increases with an increase in vehicle speed. These forces are basically identical for the standard and hub driven vehicles. On the other hand, the force exerted by the suspension system on the unsprung mass decreases slightly with the increase in vehicle speed.

It cannot be determined whether the results of the force analysis are within limits. The force exerted on the unsprung mass of the hub driven vehicle is not remarkably higher than that experienced by the standard vehicle. The force analysis only gives an indication of the magnitude of the force and vibration that the motor structure must be able to endure. The only way to determine whether or not

the results obtained are acceptable is to investigate the physical structure of the hub motor. As mentioned, the force exerted by the tyre is the larger of the forces acting on the unsprung mass. It is important that the structure is of such a nature as to divert the tyre forces away from the critical components within the motor such as the magnets. A finite element strength analysis can determine if the wheel structure and motor can withstand the shock and vibration forces presented.

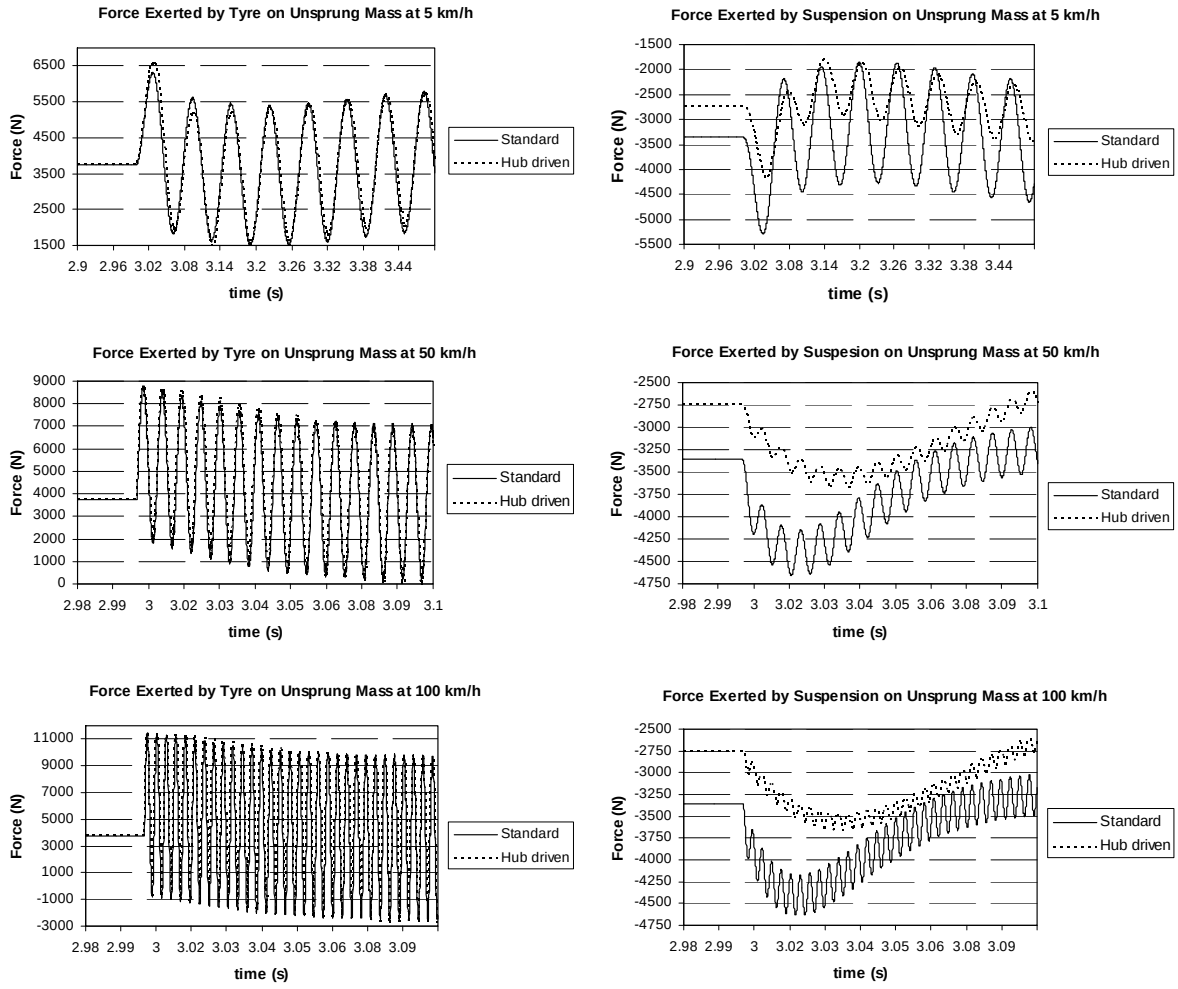

Fig 2.18: Forces exerted on unsprung mass (multiple bumps).

2.3.6 Practical Measurements

It is important to compare simulation results with practical measurement, as far as possible. This is done to determine the accuracy and validity of the simulation model as well as the conclusions drawn from the simulation results. In some cases it is not possible to make an exact comparison between the simulation and practical results, as is the case in this study. However, it is still possible to verify certain trends seen in the simulation and practical results such as decrease in unsprung mass displacement due to the increase in mass. These trends can be used to determine the validity of the results and conclusion. The main aim of the study is to observe any negative effects of the increased wheel mass thereby making hub drives unsuitable for vehicle propulsion. These negative effects can easily be seen from the practical measurements.

The parties responsible for the practical measurements of the vehicle ‘s suspension system were Mr. J. Visagie, an engineer from Optimal Energy Ltd. and the Department of Mechanical Engineering at the University of Stellenbosch. The author was not directly involved in the practical measurements or the processing of the raw measurement data. The author only took part as an observer during the practical measurements. Only some of the critical results will be presented in this section. The full results of the testing can be found in a report written by Mr. Visagie [24].

An experimental test setup was devised where a mass is attached to the hub of a vehicle. This mass should ideally be a hub motor. The risk of damage to the hub motor was not acceptable. The vehicle’s axle was modified so that the hub motor could be replaced by a weight. This weight can easily be removed in the field. The mass of the weight was chosen to be 35 kg, the same mass as the designed hub motor. Still powered by its internal combustion engine, the vehicle could be driven on a variety of road surfaces at different speeds. This setup also allows for a simple evaluation of the vehicle’s handling with and without the added wheel mass. Fig 2.19 shows the wheel assembly used.

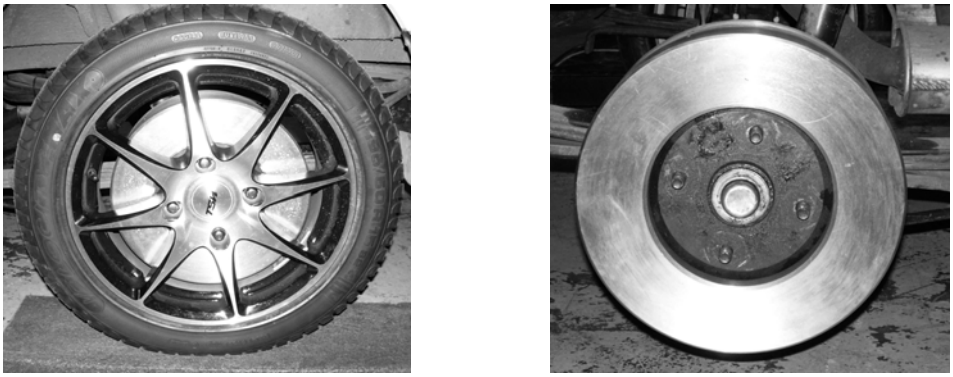

Fig 2.19: Wheel assembly.

Accelerometers were placed in certain positions on the test vehicle. Fig 2.20 shows the placement of two of the accelerometers attached to the sprung and unsprung mass. A sensor was also placed at the vehicle's estimated centre of gravity. The investigation required the monitoring of the pitch and role of the vehicle. These are both movements of the vehicle around its centre of gravity. With this data it can be determined how much of the vertical movement of the sprung and unsprung mass is caused by the pitching and rolling of the vehicle.

Fig 2.20: Accelerometers on sprung and unsprung mass

The analysis done by Mr. Visagie, unlike the simulation done by the author, concentrated on the acceleration of the sprung and unsprung mass. The sensors used in the testing measured this acceleration. The same conclusion that was drawn from the displacement of the sprung and unsprung mass can be drawn from their acceleration. Certain trends that were witnessed in the simulation results can be seen in the acceleration data.

Fig 2.21 shows the measured data from a single bump or discrete impact test was done. These results were taken from Mr. Visagie's report. It was found in the simulation results that the sprung mass of both the heavy hub (hub driven) and standard vehicle experiences the same displacement under a discreet road input. From Fig 2.21 it can be seen that this trend is found in the practical measurements as well. The measured data shows that the acceleration of the heavy hub and standard vehicle's sprung mass is the same. If two bodies have the same acceleration they will have the same displacement, ignoring their initial position such as static deflection. Correlation can also been seen between the simulation and measured results of the unsprung mass. The simulation results showed that the heavy hub vehicle's unsprung mass experiences less displacement during a discrete impact than the standard vehicle. The same trend is seen in the measured results of the unsprung mass; Fig 2.21. The large second oscillation in the standard vehicle's unsprung mass is attributed to a measurement error.

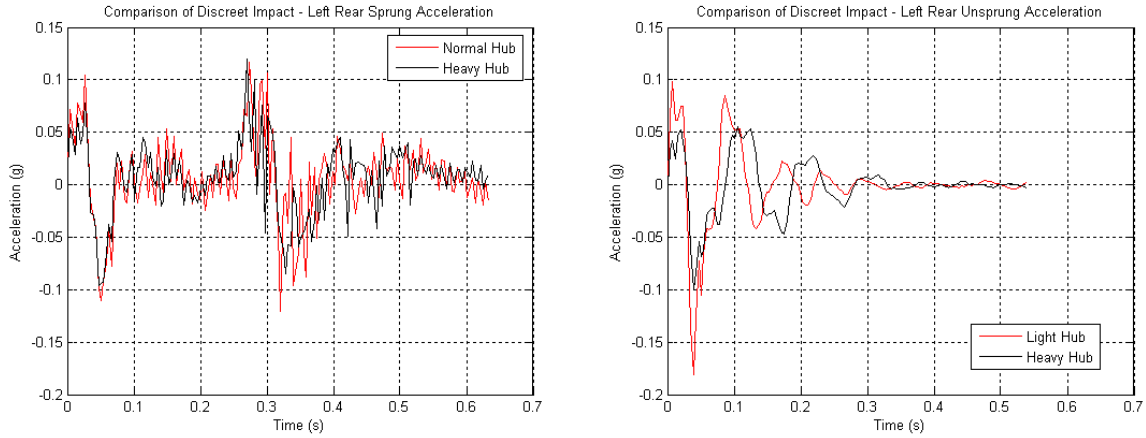

Fig 2.21: Sprung and unsprung mass measured acceleration (single bump).

The simulation results from section 2.3.4, for harmonic road input, show a trend where the sprung mass as well as the unsprung mass of the heavy hub vehicle experiences less vibration than that of the standard vehicle. Fig 2.22 shows this same trend in the acceleration when driven over a harmonic road surface. It can be seen that the vibration amplitude is less for the heavy hub vehicle than for the standard vehicle, verifying the simulation results.

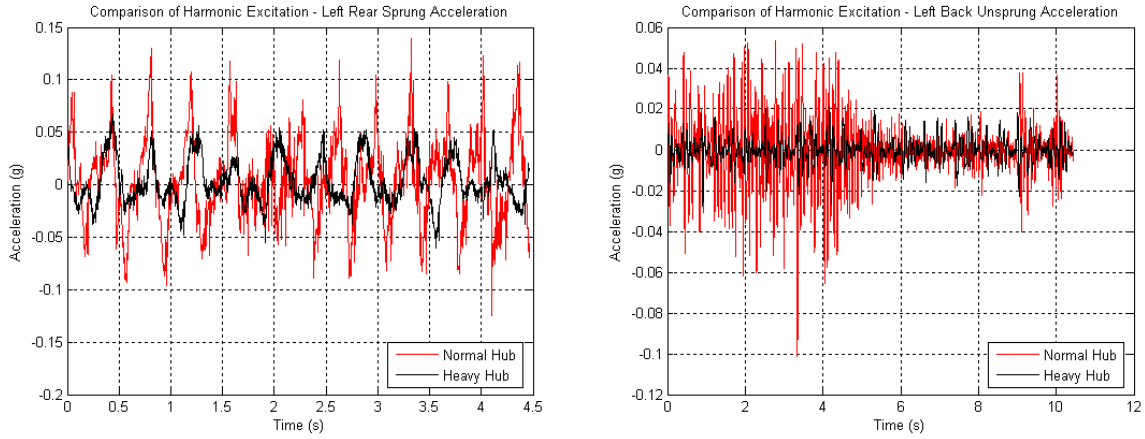

Fig 2.22: Sprung and unsprung mass measured acceleration (single bump)

The testing of the heavy hub vehicle presented no negative effects. Drivability stayed much the same for the heavy hub and standard vehicles. Overall, the practical testing and measurements confirm that the conclusions drawn from the simulation results are accurate.

2.3.7 Summary and conclusion

In this chapter a study was done to investigate the effect of placing hub motors in the wheels of a vehicle. The effect on the stability and comfort was investigated. This study took on the form of a comparative study between a standard and a hub driven vehicle. A vehicle model representing a quarter of the vehicle was derived. This model was used to do a frequency response analysis as well as the simulation of the system's response to road condition at various speeds.

Both a Bode plot analysis and natural frequency analysis showed promising results and no negative effects could be observed. The frequency analysis presents no reason for not placing hub motors in the wheels of the vehicle.

The simulation results show no major difference in the response of the standard and hub driven vehicles. The results from the unsprung mass force analysis are inconclusive without any structural analysis done.

The question arises as to what the limit is for the unsprung-sprung mass ratio. After studying all the results, the author recommends that the unsprung mass should not be more than 80% of that of the sprung mass. As mentioned in a previous section, the two natural frequencies of the system move closer together as the masses become the same. Although the natural frequencies do not lie at the same point when the masses are the same, they are close enough together to cause unwanted oscillation.

Chapter 3 Electric vehicle traction control

A traction control system, in any form, is an integral part of any electric vehicle. The main reason for this is the quick response of the electric motors to deliver torque on command. It is even more important in in-wheel applications where there is no response delay due to the drive train of the vehicle (deferential, gearbox etc.). This chapter investigates traction control for electric vehicles and determines the system required to do so.

A step by step development of a conceptual traction control system is given in this chapter, starting with the simplest system required, and then building up to a full traction control system. After the conceptual traction control system is presented, a model is derived that is required for the development of the control strategy and the algorithm, as well as for simulation purposes.

Traction control systems for internal combustion engine vehicles are well developed. Many of the same principles that apply to internal combustion engine vehicles apply to electric vehicles as well. Many studies have been done in the field of electric vehicle traction control systems [25] [26] [27].

3.1. Conceptual traction control system

The first step in any system development is to determine and define each part of the system. The same applies when developing a traction control system. Fig 3.1 shows a block diagram of such a conceptual vehicle system.

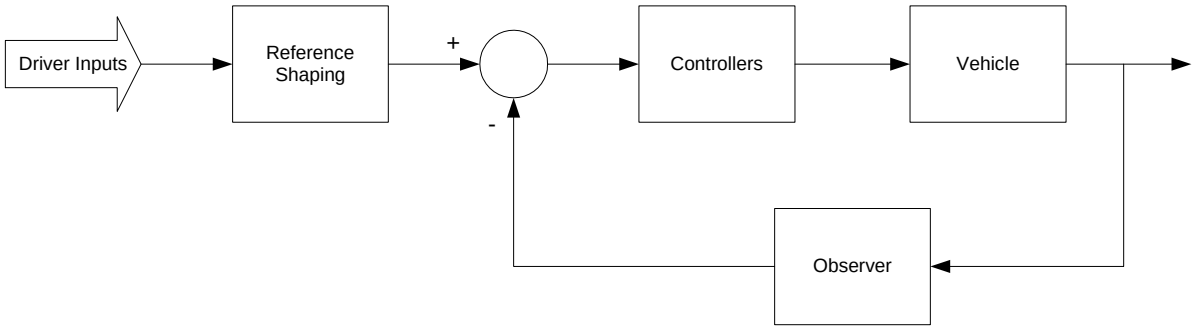

Fig 3.1: Vehicle system block diagram

The vehicle system has the following parts:

a) driver inputs
b) reference shaping
c) controllers
d) actual vehicle / vehicle model
e) observer system (load torque, adhesion etc.)

a.) The driver inputs are defined as all the devises that the driver uses to give commands to the vehicle. These include, depending on the complexity of the control system, the accelerator pedal, brake pedal, steering wheel etc. These could either be mechanical or electronic devices as well as being analogue or digital. The outputs of the driver input devices are passed on to the control circuit of the vehicle.

b.) The main function of the reference shaping block is to determine the required controller references. These references can be speed, current, torque references or even a combination of these depending on the type of controller implemented. The reference is obtained by interpreting the information received from the driver input devices. This information is generally position information given by the driver input devices as a voltage or current signal, depending on the device. The reference shaping block has the added function of not only determining the controller references but also of determining if these references are suitable operating conditions for the vehicle and of adjusting the references accordingly. This algorithm thus limits the response of the vehicle. Reference shaping is the first stage in the traction control of the vehicle. The reference shaping block also serves as an input filter to the system. This filter can remove any unwanted noise added to the signal received from the driver input devices. The filter can either be implemented before reference shaping is done or built into the shaping algorithm, depending on the choice of system.

c.) The controller block represents the algorithm and circuitry used to control the electric motor or motors. The type and complexity of the controllers is the choice of the designer. These controllers can be speed and/or current controllers. It should be noted that no traction control takes place in this block. As stated, its function is to control the motors according to the references it received from the reference shaping block.

d.) The main component of the system is probably the motor or vehicle. The vehicle block represents either the model or the actual machine. The model can either be a motor or vehicle model depending on the traction control system used. This will be explained in a coming section.

e.) The last block represents an observer algorithm. An observer forms part of the control system of the vehicle. Its function is to calculate or observe a quantity in the system that cannot be physically measured. An example of such a quantity is the load torque that is placed on a motor. The controllers mentioned usually do not take these quantities into account. After the observer has calculated these quantities, it determines the value with which the controller references need to be compensated to take them into account. It can be seen that it is in this observer block that the real traction control takes place.

3.2. Evolution of a traction control system

There exists a large amount of freedom when choosing a traction control system. The complexity of the traction control system depends on aspects such as number of driven wheels, directions of control etc. The ultimate decision lies with the designer of the system. A step by step evolution of a system from a simple to a complex traction control system will be studied in the following section.

The simplest implementation of a traction control system is to use motor controllers with a load torque observer. A good example of such a system is given in H.W. de Kock's thesis, *Dynamic control of the permanent magnet assisted reluctance synchronous machine with constant current angle* [28]. In his thesis, a control strategy is proposed for a PMA RSM using a load torque observer. Thus, the same control used in the laboratory testing of the vehicle's motor can be implemented in the vehicle itself. There is a direct connection between the load torque that is experienced by the vehicle's motor and the traction of the vehicle. Traction control can be achieved by compensating for variations in load torque; the very function of a load torque observer. Fig 3.2 shows a block diagram of such a system.

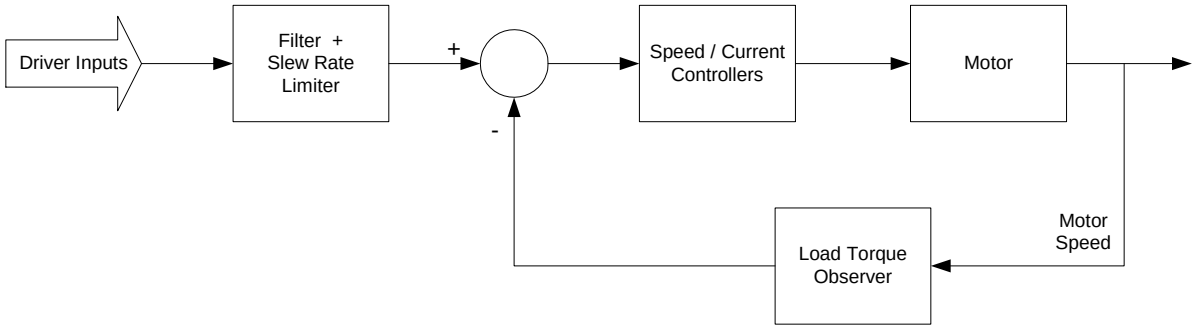

Fig 3.2: Motor control system with load torque observer.

There is a loss in accuracy when using a load torque observer. This is due to the fact that the control focuses on the motor and not the vehicle as a whole.

A very basic reference shaping algorithm is used in Fig 3.2. The reference shaping consists of an input filter as well as a slew rate limiter. The function of the slew rate limiter is to limit the acceleration of the motor and thus the acceleration of the vehicle. The rate of acceleration can be set to a fixed value or can be a driver input.

Using a slew rate limiter to determine the controller references is a very primitive way of reference shaping. A more accurate and reliable method of reference shaping is to use speed curves. Speed curves are mathematical equations used to calculate the acceptable speed and acceleration of the motor from the signals received from the driver input devices. These speed curves have been used in EV traction control systems [29] [30]. They have the following advantages:

a) Smooth acceleration of the motor or vehicle by removing vehicle jerk
b) Improved wheel traction

The speed curves also serve as an input filter. The mathematical nature of the speed curve calculation removes any high frequency content from the signals received from the driver input devices.

A load torque observer is still required with the use of speed curves to compensate for load torque variations. The introduction of speed curves vastly improves the performance of the traction control system. Fig 3.3 shows the block diagram of the vehicle system with speed curves.

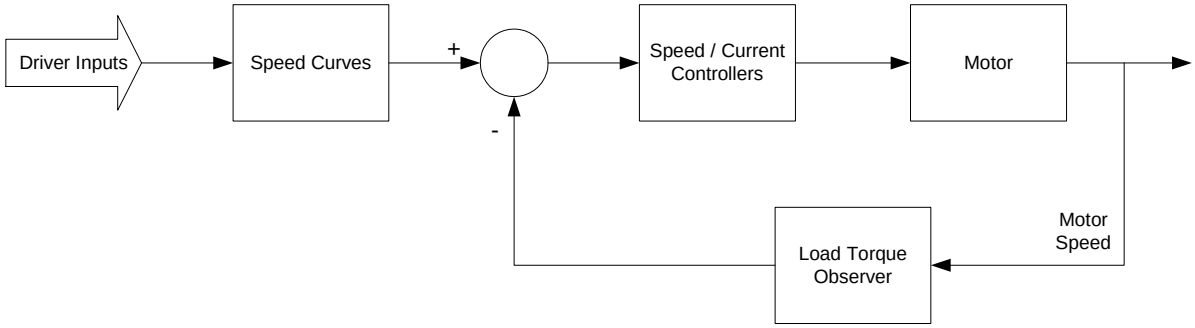

Fig 3.3: Motor control system with speed curves and load torque observer.

The next step in the evolution of a traction control system is to move to a full vehicle system. The machine model used in the motor control system is replaced with a vehicle model. The model can range from a single wheel quarter vehicle model to a full four wheel model. The complexity of the model is dependent on the complexity of the traction control system.

With the replacement of the machine model with a vehicle, the load torque observer needs to be replaced as well. The quantity that is observed is dependent on the traction control strategy used. These quantities include adhesion coefficient, adhesion force and wheel slip ratio. It is the observing of these quantities that gives the traction control its complexity. Fig 3.4 shows a block diagram of the system.

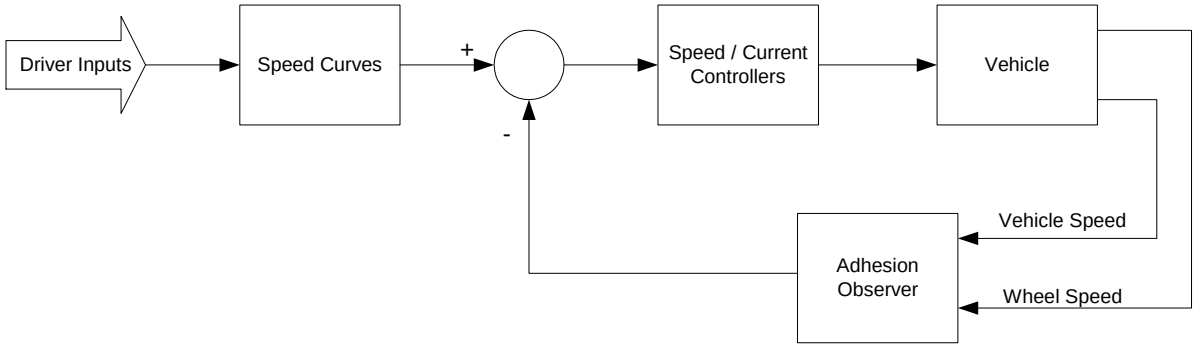

Fig 3.4: Vehicle system with vehicle model and wheel adhesion observer.

3.3. Vehicle Model

A vehicle model is required for simulation and control system design purposes. The complexity of the model is dependent on two factors i.e. i) the level of accuracy required from the vehicle model ii) the number of aspects to be controlled by the traction control system such as longitudinal and/or lateral traction. In this thesis a one wheel traction control system is presented. Only the longitudinal traction of the vehicle is dealt with. The model does not have to take into account the effect of the other three wheels on the fourth one. Thus, a quarter vehicle model would be sufficient. A more complex model is required if control of the lateral movement of the vehicle has to be done or if features such as an electronic differential are to be added to the traction control system. The quarter vehicle model can easily be duplicated for four wheels if a four wheel model is required, given that only the longitudinal movement of the vehicle has to be taken into account.

3.3.1 Quarter vehicle model

Fig 3.5 is a representation of a quarter of the vehicle. It also shows the forces acting on the different parts of the vehicle.

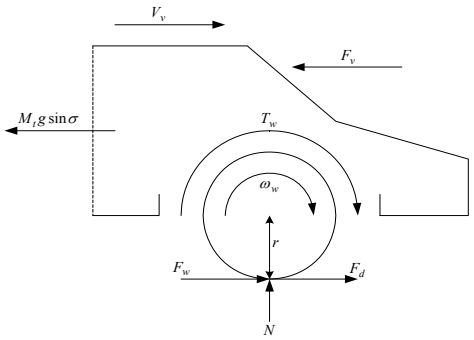

Fig 3.5: Quarter vehicle model

The following symbols are found in Fig 3.5:

F_d: friction force
F_w: rolling resistance
F_v: force due to wind resistance
T_w: torque applied to wheel
N: tyre normal force
M_v: vehicle mass
M_w: wheel mass
J_w: wheel inertia
r_w: wheel radius
σ: incline angle of road
ω_w: angular velocity of wheel
v_v: linear velocity of vehicle

There are two forces acting at the point of contact between the road surface and the tyre contact patch, as shown in Fig 3.5. These are the rolling resistance, F_w and the friction or driving force F_d. The rolling resistance is equal to the product of the tyre normal force, N, and the rolling resistance coefficient, μ_w and is given as:

$$F_w = N\mu_w \tag{3.1}$$

The origin of the friction or driving force will be discussed in section 3.3.2.

The difference between the rolling resistance and the driving force is the following. The rolling resistance is always in the opposite direction to wheel rotation. It only changes direction when the direction in which the wheel is rotating changes. On the other hand, the driving force is in the opposite direction to the applied wheel torque. The applied torque is not always in the direction of wheel rotation. An example of this is when braking torque is applied to the wheel of the vehicle.

Two forces act on the vehicle body. These are i.) the force due to the aerodynamic resistance of the vehicle and ii.) the force caused by the mass of the vehicle when standing or moving on an incline. The force due to wind resistance is given as:

$$F_v = 0.5 C_d A_v \rho_{air} v_v^2 \tag{3.2}$$

where C_d is the drag coefficient of the vehicle, A_v is the equivalent frontal area of the vehicle and ρ_{air} the density of air. The force due to the mass of the vehicle is given as:

$$F_m = M_v g \sin\sigma \tag{3.3}$$

where M_v is the vehicle mass, g the gravity constant and σ the incline angle.

3.3.2 Vehicle-wheel dynamics

It is important to study the dynamics between the road, wheel and vehicle when deriving a model for the vehicle system. It is important that all the forces that play a role in the traction of a vehicle are known. The system may not be as simple as it appears.

The system analysis starts with a body that has a pure rolling motion [31] [32]. A pure rolling body is a cylinder or sphere whose motion can be modelled as the super positioning of pure rotation and pure translation motion. There are no external forces or torque applied to a pure rolling body. A rolling body is shown in Fig 3.6. During pure translation all the points on the body have the same linear velocity as shown in Fig 3.6a. All the points on the body have the same velocity as the centre of mass i.e. $v_{cm.}$ During pure rotational motion the top and bottom points of the body have a linear velocity equal to the product of the rotational velocity and the body radius i.e. $r_w\omega_w$. It must be remembered that these points are not fixed to the body but are fixed points in space. The velocity of the centre of mass is equal to zero. Pure rotational motion is shown in Fig 3.6b.

Pure translation and pure rotational motion is super positioned to obtain pure rolling motion as shown in Fig 3.6c. The centre of the body has a linear velocity of v_{cm} and the top and bottom of the body a linear velocity of $v_{cm} + r_w\omega_w$ and $v_{cm} - r_w\omega_w$ respectively. A characteristic of a body with a pure rolling motion is that the contact points i.e. the contact patch between the body and the surface, have the same velocity relative to each other. If the surface has a linear velocity equal to zero then the bottom point of the body also has a linear velocity equal to zero. Taking this into account, v_{cm} is equal to $r_w\omega_w$ for a body that has pure rolling motion.

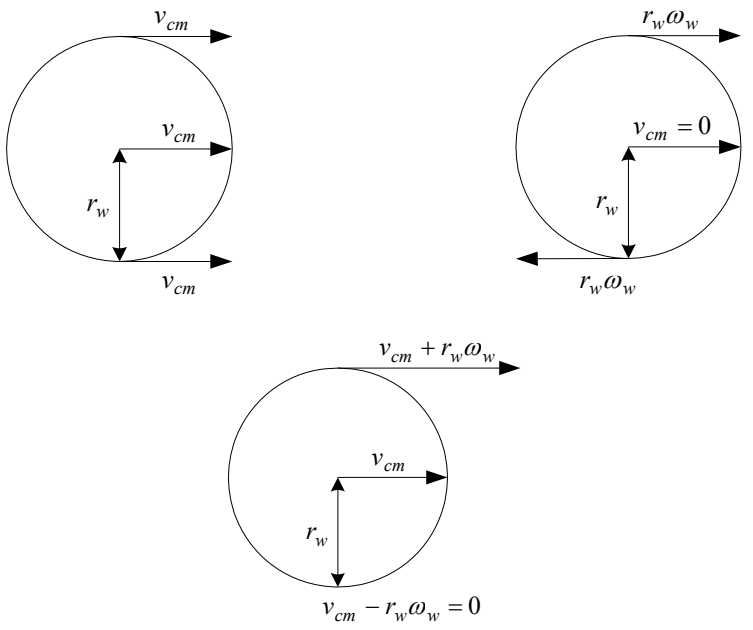

Fig 3.6: Body with (a) pure translation (b) pure rotation (c) pure rolling

The next step is to apply a torque, T_w, to the centre of mass of the body. This applied torque causes a force to be generated between the body and surface contact points in the form of a frictional force, F_d. This frictional force is called static friction. Static friction only occurs when two surfaces that are in contact with each other do not move relative to each other. Static friction is less or equal to the product of the tyre normal force, N, and the static friction coefficient, μ_s. The equation for the static friction force is derived in Appendix B and is given as:

$$F_d = \frac{1}{\frac{J_w}{M_v r_w} + r_w}\left[T_w - r_w F_w + \frac{J_w}{M_v r_w}\left(F_v + F_m\right)\right] \tag{3.4}$$

It is this friction force that causes the acceleration of the body in the linier direction. As long as the contact points have the same velocity relative to each other the body still has a pure rolling motion. Fig 3.7 shows the free body diagram of the rolling body.

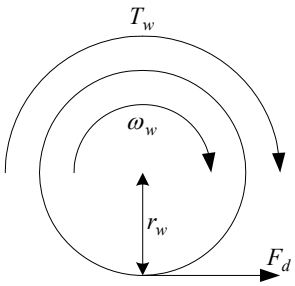

Fig 3.7: Free body diagram of rolling body

It is possible that the body can slip or spin on the contact surface if enough torque is applied to the centre of mass of the body. One of the criteria for this to happen is when the friction force, calculated with equation 3.4, is larger than $\mu_s N$, which is not possible. The contact points do not move at the same velocity relative to each other any more. Thus $v_{cm} = r_w\omega_w$ does not apply any more. A force still exists between the body and surface contact points. This frictional force is no longer static friction but is now known as kinetic friction. The value of the kinetic friction coefficient is different to the static friction coefficient for the same road surface.

The boundary between static and kinetic friction is mainly determined by the amount of torque applied to the centre mass of the body. The equation that gives the maximum torque that can be applied before kinetic friction occurs is derived in Appendix B. This torque is given as:

$$T_w \leq \left(\frac{J_w}{M_v r_w} + r_w \right) \mu_s N + r_w F_w - \frac{J_w}{M_v r_w} \left(F_v + F_m \right) \qquad (3.5)$$

All of the above applies to the vehicle system as well. The vehicle's wheel will have a pure rolling motion until enough torque is applied to the wheel causing it to slip (accelerating) or skid (braking). The frictional force is also known as the driving force. It's known as the driving force because it is this force that is responsible for accelerating or decelerating the vehicle.

3.3.3 Dynamic equations

The dynamic equations for the system in Fig 3.5 are obtained by applying Newton's second law of motion to the vehicle body and wheel. Each is taken as a separate body. As there are two bodies, two equations need to be satisfied:

$$M_V \dot{v}_v = \sum F \tag{3.6}$$

$$J_w \dot{\omega}_w = \sum T \tag{3.7}$$

(i) Force acting on vehicle

Friction or driving force: F_d

Force due to wind resistance: F_v

Force due to its own mass pulling it down an incline: F_m

Taking the forward direction as positive, it can be seen from Fig 3.5 that F_d is positive and that F_m and F_v are negative.

(ii) Torque acting on wheel

Motor torque applied to wheel: T_w

Torque equivalent of rolling resistance: $r_w F_w$

Torque equivalent of driving force: $r_w F_d$

The torque produced by the forces, F_w and F_d, is calculated by multiplying them with the radius of the wheel. The positive direction of rotation is taken as the direction in which torque must be applied to cause the vehicle to move forward. Thus, the clock wise direction is taken as positive. Taking this into account, it can be seen that the applied wheel torque is positive and the torque equivalents of the rolling resistance force and the driving force is negative as they are in an anti-clockwise direction.

If the above forces and torque are substituted into Equations 3.6 and 3.7, they become:

$$M_V \dot{v}_v = F_d - F_v - F_m \tag{3.8}$$

$$J_w \dot{\omega}_w = T_w - r_w F_w - r_w F_d \tag{3.9}$$

If equations 3.2 and 3.3 are substituted into equations 3.8 and 3.9 the dynamic equations of the system become:

$$M_V \dot{v}_v = F_d - 0.5 C_d A_v \rho_{air} v_v^2 - M_V g \sin\sigma \tag{3.10}$$

$$J_w \dot{\omega}_w = T_w - r_w F_d - r_w N \mu_f \tag{3.11}$$

Equation 3.10 shows that it is the friction force between the tyre and the road that causes acceleration of the vehicle. For this reason is it called the driving or traction force.

3.3.4 Slip ratio and adhesion coefficient

In section 3.3.3 it was stated that a torque boundary exists between static and kinetic friction. Is it possible to determine the kinetic friction coefficient? It has been found that there is a relationship between the slip ratio, λ_{sr}, and the kinetic friction coefficient. This slip ratio is defined as the difference between the wheel speed and vehicle speed. These speeds should be of the same orientation, either being rotational or longitudinal speed. The longitudinal velocity was chosen. The slip ratio is given as:

$$\lambda_{sr} = \frac{v_w - v_v}{v_w} = \frac{r_w \omega_w - v_v}{r_w \omega_w} \tag{3.12}$$

This slip ratio forms the basis of almost all traction control systems, even ABS braking systems. Many equations exist to describe the relationship between the slip ratio and the kinetic friction coefficient, also known as the adhesion coefficient. The most commonly used equation is:

$$\mu_a(\lambda_{sr}) = \frac{\left(2\mu_p \lambda_p \lambda_{sr}\right)}{\left(\lambda_p^2 + \lambda_{sr}^2\right)} \tag{3.13}$$

where μ_p is the maximum adhesion coefficient and λ_p the slip ratio at which the maximum adhesion coefficient occurs. These values are dependent on the type of road surface as well as the road surface conditions. Fig 3.8 shows the adhesion coefficient for three hypothetical roads. These roads could be for example a dry tar road, a wet tar road, and a tar road with an icy surface.

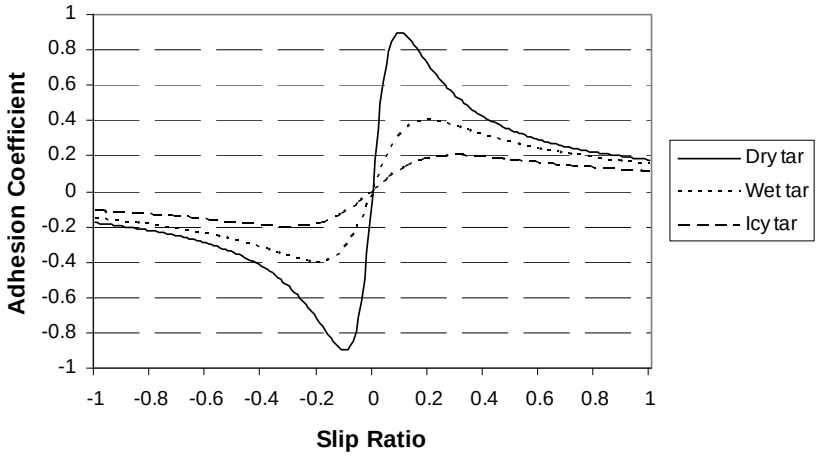

Fig 3.8: Adhesion coefficients for three hypothetical road surfaces.

Fig 3.8 clearly shows that each road surface has an optimum slip ratio at which the maximum adhesion coefficient occurs and thus the maximum driving force. It is thus the purpose of an adhesion coefficient observer to determine the optimum slip ratio, as mentioned in a previous section. The equation for the driving force during kinetic friction conditions is given as:

$$F_d = \mu_a(\lambda_{sr})N \tag{3.14}$$

Two words that are extensively used in the world of traction control systems need to be defined. These are 'skid' and 'slip'. Slip occurs when the wheel's velocity is greater than that of the vehicle i.e. λ_{sr} is positive. This occurs during acceleration of the vehicle. Skid occurs when the wheel's velocity is less than that of the vehicle i.e. λ_{sr} is negative. This occurs during deceleration of the vehicle.

3.3.5 Simulation model

The dynamic equations are easily implemented in a software package such as MatLab/Simulink. The rotational velocity and acceleration of the wheel, in Equation 3.11 are changed to the longitudinal direction. The dynamic equations are:

$$M_v\dot{v}_v = F_d - 0.5C_d A_v \rho_{air} v_v^2 - M_v g \sin\sigma \tag{3.15}$$

$$\tfrac{1}{r_w} J_w \dot{v}_w = T_w - r_w N \mu_w - r_w F_d \tag{3.16}$$

The dynamic equations are changed into integral form so that the block diagram can be derived. Fig 3.9 and 3.10 show the block diagram implementation of the dynamic equation in integral form.

The dynamic equations in integral form are:

$$v_v = \int \frac{1}{M_V}\left[F_d - 0.5C_d A_v \rho_{air} v_v^2 - M_v g \sin\sigma\right]dt \tag{3.17}$$

$$v_w = r_w \int \frac{1}{J_w}\left[T_w - rN\mu_w - rF_d\right]dt \tag{3.18}$$

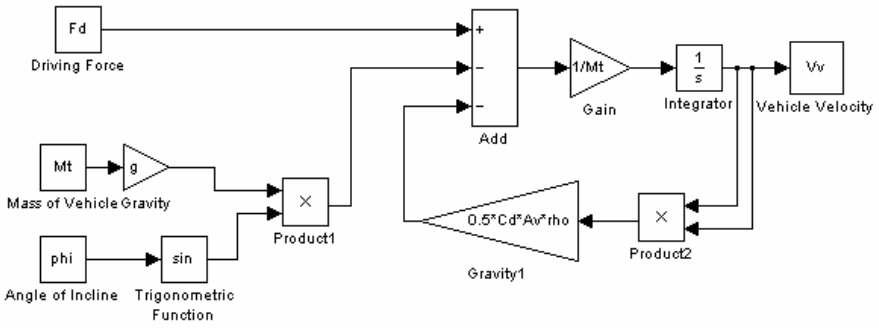

Fig 3.9: Block diagram of equation 3.17.

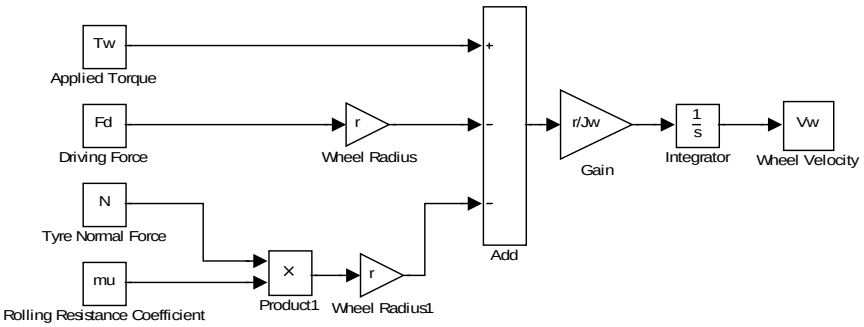

Fig 3.10: Block diagram of equation 3.18.

In section 3.3.3 it was shown that there is a limit to the amount of torque that can be applied to a wheel before the wheel slips. This is the boundary between static and kinetic friction. The vehicle block diagram model thus requires a selector between static and kinetic friction. This selection is done according to equation 3.5. Fig 3.11 shows the friction selector.

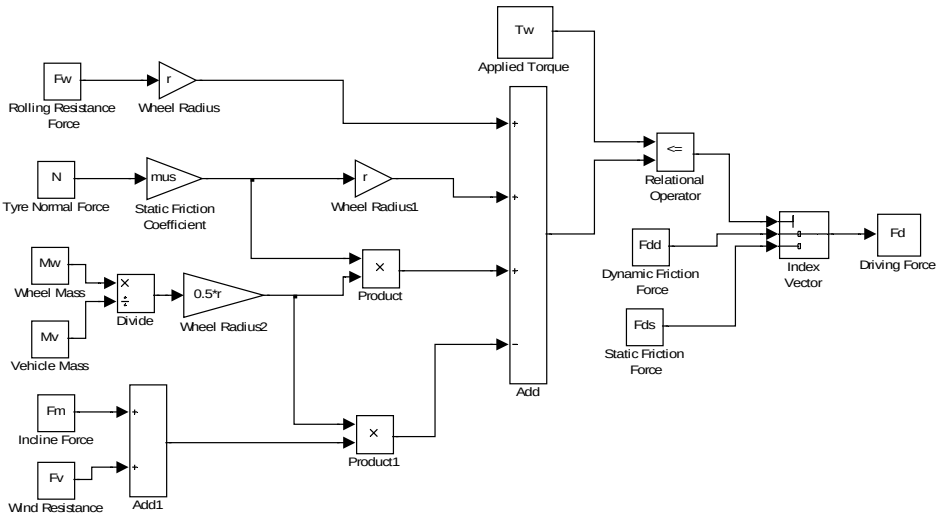

Fig 3.11: Block diagram of friction selector.

The driving force is defined by one of two equations depending on whether static or kinetic friction occurs. The two equations for the friction force are given by equation 3.4 and 3.14 and are implemented in block diagram form as shown in Fig 3.12 and 3.13.

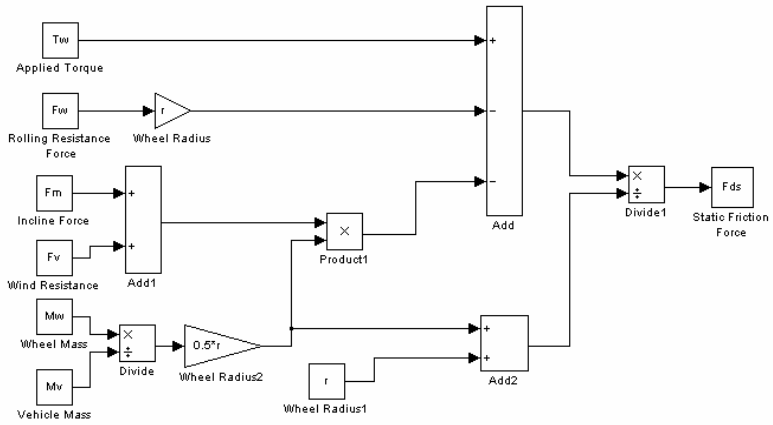

Fig 3.12: Block diagram of static friction.

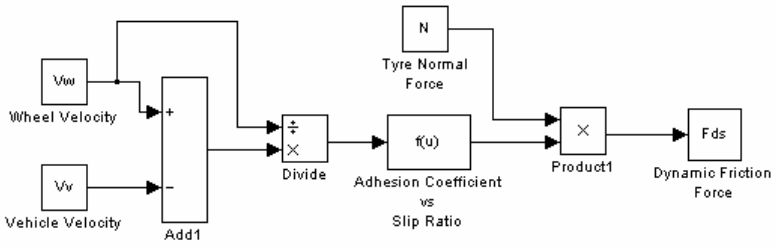

Fig 3.13: Block diagram of kinetic friction.

The full block diagram of the vehicle model is obtained by combining all of the above figures and is shown in Fig 3.14.

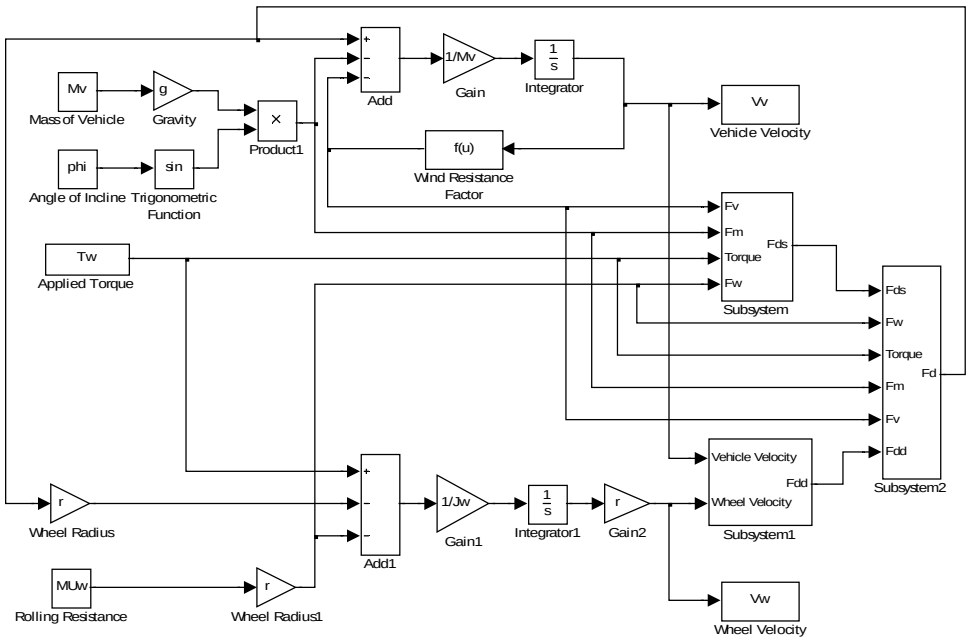

Fig 3.14: Block diagram of vehicle model.

3.4. Simulation results

In this section a few simple simulations are done to investigate the response of the vehicle model when torque is applied to the wheel of the vehicle. The model is implemented in block diagram form in MatLab/Simulink. The vehicle parameters are imported into the simulation by means of a MatLab M-file. These vehicle parameters are varied in the simulations to investigate the effect they have on the traction of the vehicle.

The vehicle mass, M_v, used in the simulation is a critical parameter for this determination. It has been found that the total vehicle mass used as simulation mass is related to the amount of driving wheels the vehicle has. The quarter vehicle model has only one driving wheel, where the actual vehicle could either have two or four driving wheels. The actual vehicle mass must be divided by the number of driving wheels to obtain the total vehicle mass used in the simulation.

The applied torque is assumed to be an ideal step function. This is not true for real vehicles. It is a known fact that electric motors deliver constant torque below base speed and constant power above base speed. The amount of torque that an electric motor delivers decreases as the speed increases

above base speed. The shape of the applied torque is not an ideal step function, even with the introduction of a gear box to the drive system of an electric vehicle. A step torque was chosen to simplify the input to the system. The investigation requires a magnitude of torque applied to the wheel of the vehicle and not accuracy in the shape thereof. The acceleration and speeds reached in the simulation results might not be an accurate representation of the actual vehicle. The simulation is a worst case representation of the actual world. Even with the applied torque being ideal, the simulation results give a good indication whether the conditions require a vehicle to have traction or not. No torque control is done in any of the simulations. The purpose of this simulation is to illustrate the need for traction control.

3.4.1 Varying-torque simulation

The first simulation shows the effect of various applied torques on the traction of the vehicle. A total vehicle mass, M_v, of 1500 kg was chosen. Dry tar was chosen as the road surface having a static friction coefficient, μ_s of 0.7 and a kinetic friction coefficient as shown in Fig 3.8. This kinetic friction has a maximum friction coefficient of 0.9 that occurs at a slip ratio of 0.1. The applied torque was chosen having values of 100, 200 and 300 Nm.

Fig 3.15 shows the torque boundary between static and kinetic friction. It must be noted that the variation in this boundary is very slight. More than 800 Nm of torque per wheel is required to cause the wheel to slip. A road surface with a smaller static friction coefficient is needed for the torque boundary to be crossed with the above applied torque. This will be shown in the next section. Fig 3.16 shows the vehicle and wheel speeds.

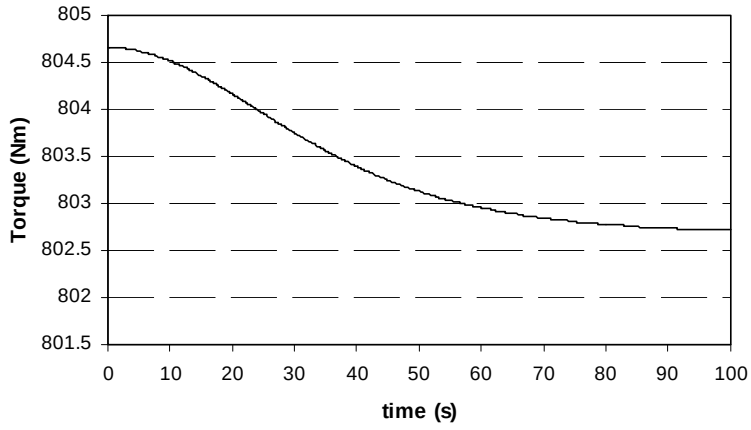

Fig 3.15: Torque boundary between static and dynamic friction (dry tar).

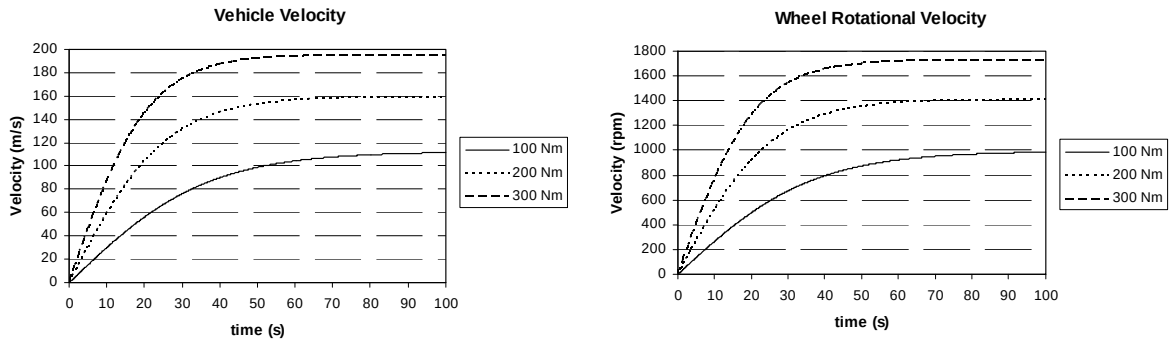

Fig 3.16: Vehicle and wheel velocity for varying torque.

3.4.2 Varying-road condition simulation

In the previous section it was found that for a dry tar road, having a static friction coefficient of 0.7, a high amount of applied torque is required to cross the torque boundary and cause the wheel to slip. In this section two different road surfaces are used in the simulation i.e. dry and wet tar. Wet tar can have a static friction coefficient of 0.3 in comparison to that of 0.7 for dry tar. Wet tar has a kinetic friction coefficient or adhesion coefficient as seen in Fig 3.8, having a maximum kinetic friction coefficient of 0.4 at a slip ratio of 0.2. An applied torque of 250 Nm was chosen. Fig 3.17 shows the torque boundary for a road surface having a static friction coefficient of 0.3. It can be seen that the applied torque is higher than the torque limit. The vehicle wheel loses traction due to the driving force being too small to stop the wheel from accelerating. The wheel has a very high acceleration as can seen in Fig 3.18b. This shows the need for a torque control algorithm to stop rotational runaway of the electric motors. Rotational runaway of an electric motor is a very dangerous occurrence, both to the vehicle and its occupants. The vehicle still accelerates as can been seen in Fig 3.18a, but its acceleration and top speed are lower than for dry tar.

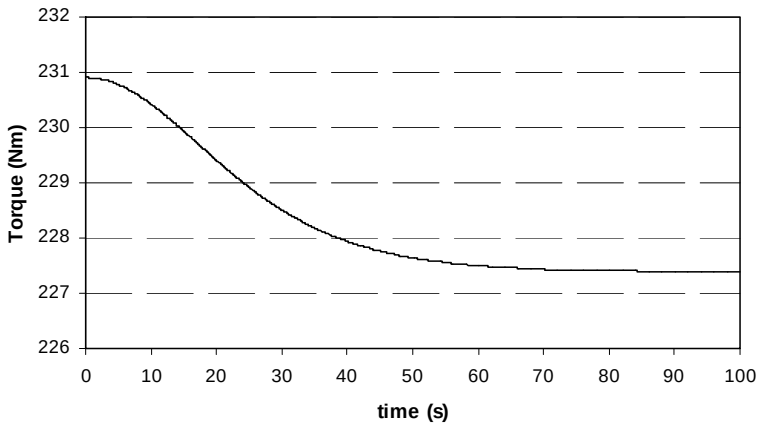

Fig 3.17: Torque boundary between static and dynamic friction (wet tar)

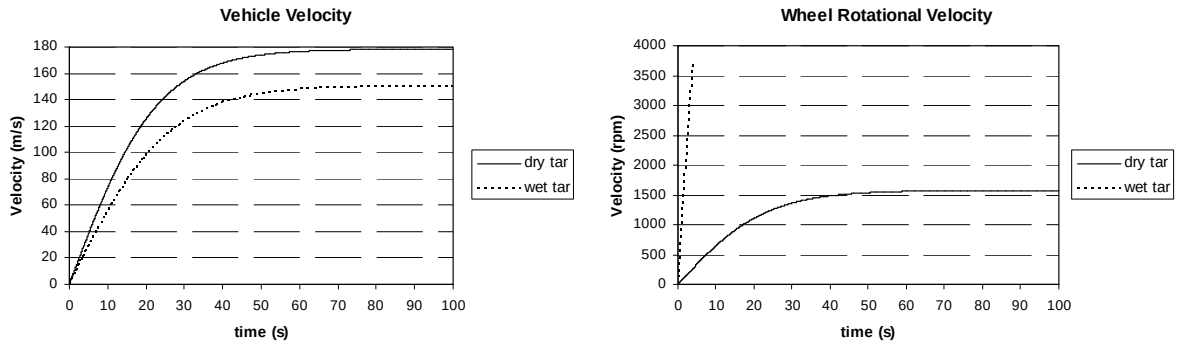

Fig 3.18: Vehicle and wheel velocity for varying road conditions.

3.4.3 Varying-vehicle-mass simulation

The mass of the vehicle plays a role in the traction of the vehicle, as can be seen in equation 3.5, the equation for the torque boundary between static and kinetic friction. In the following simulation, vehicle masses of 900 and 1200 kg were chosen. A road surface with a static friction coefficient of 0.4 and an adhesion coefficient the same as used in the simulation in section 3.4.2, were chosen. Fig 3.19 shows the torque boundary for both these cases. The applied torque for the 1200 kg vehicle is well below the torque limit, and thus no wheel slip take place. On the other hand, the torque for the 900 kg vehicle is above the boundary and wheel slip will takes place as can be seen in Fig 3.20.

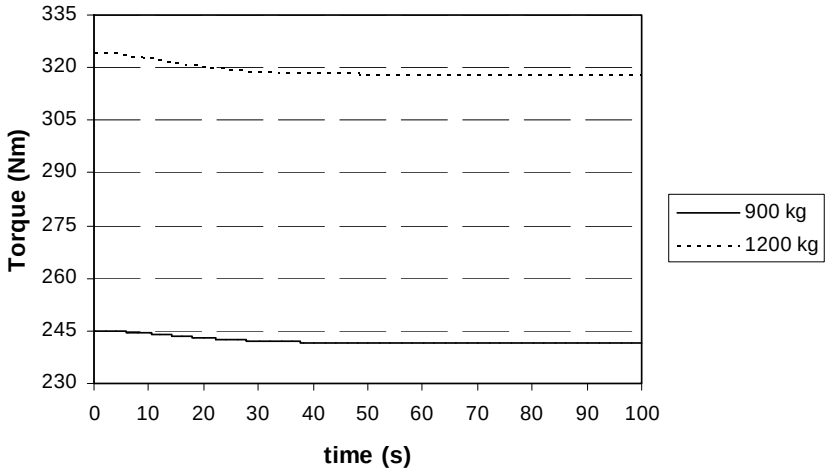

Fig 3.19: Torque boundary between static and dynamic friction.

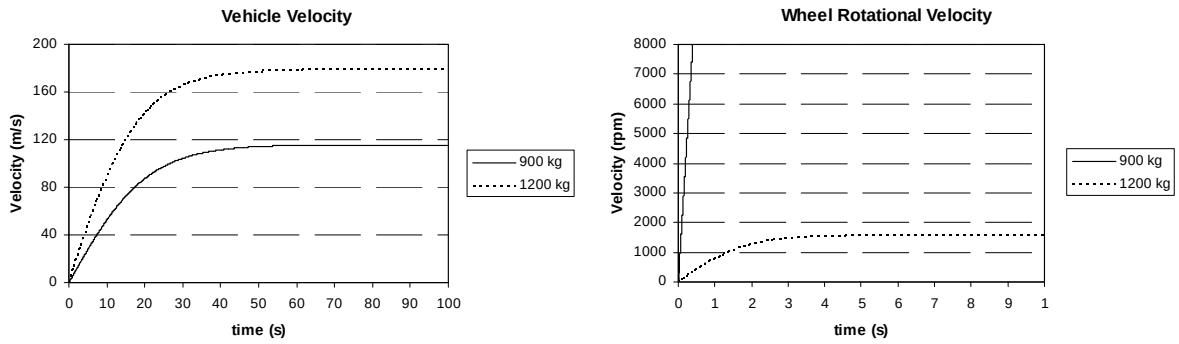

Fig 3.20: Vehicle and wheel velocity for varying vehicle mass.

3.4.4 Torque Control

In the previous sections the results showed the importance of controlling the torque to avoid rotational runaway of the electric motor. The best method of controlling the traction of the vehicle is to keep the applied torque below the torque boundary. The trouble with this control strategy is that it is difficult to obtain the value of the static friction coefficient. The static friction coefficient is required to calculate the torque boundary, as seen in equation 3.5. It is a complex if not nearly impossible task to determine the static friction coefficient for a specific road surface. A different strategy is required to control the applied torque and thus the traction of the vehicle. It is here that the before mentioned adhesion and slip observer control strategies are used.

A simulation has been prepared to illustrate the strategy of slip control. A hypothetical road surface was chosen for the simulation. This road surface does not exist in the actual world. The road surface has a low static friction coefficient and a high adhesion coefficient. It was chosen so that the road would have a low torque boundary, but would have a high driving force once the wheel slipped. Fig 3.21 shows the torque boundary for the chosen road surface.

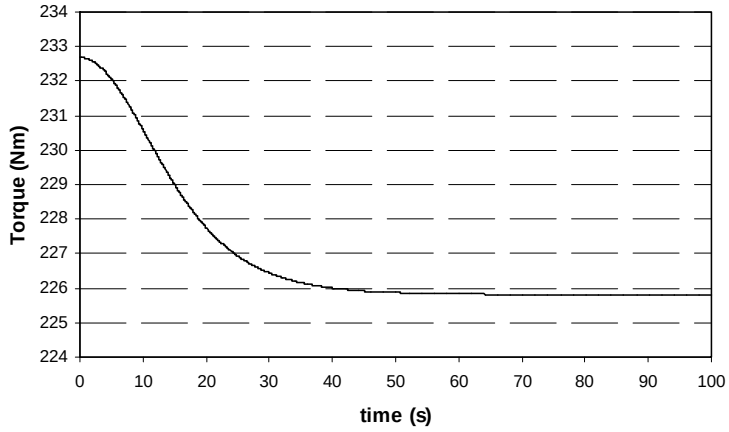

Fig 3.21: Torque boundary between static and dynamic friction

The applied torque was chosen close to the torque boundary i.e. 230 Nm. The total vehicle mass was chosen as 1000 kg. Fig 3.22 shows the linear velocity of both the vehicle and wheel. At the time when the applied torque crosses the torque boundary the wheel starts to slip but does not run away. This is due to the fact that the driving force is large enough to stop rotational runaway.

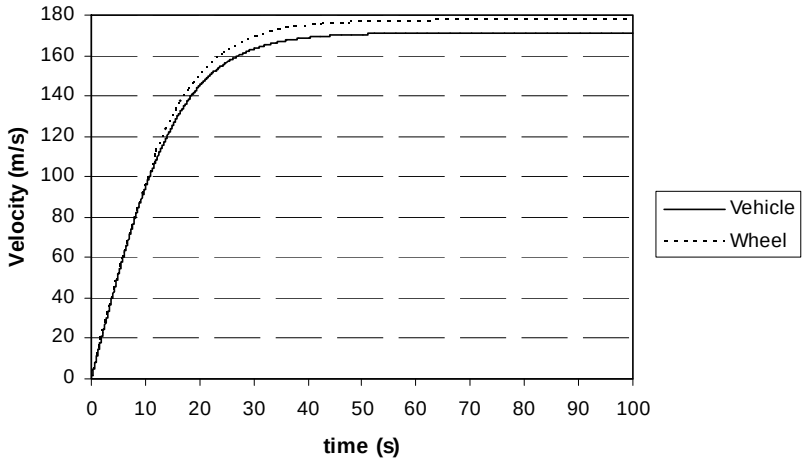

Fig 3.22: Vehicle and wheel linear velocity with torque control.

Fig 3.23 shows the slip ratio when 225, 230 and 235 Nm are applied to the wheel of the vehicle. The torque boundary is never crossed when 225 Nm of torque is applied. The wheel and vehicle move at the same velocity and the slip ratio is equal to zero. The boundary is crossed when 230 Nm is applied to the wheel of the vehicle. The applied torque is not of such a magnitude as to overcome the driving force and the wheel does not experience rotational runaway. Fig 3.23 shows that the slip ratio settles at 0.05 when 230 Nm of torque is applied. Consider Fig 3.8, the adhesion versus slip ratio curve. The applied torque accelerates the wheel, increasing the slip ratio and moving it along the μ_a-λ_{sr} curve. As the slip ratio increases, so the driving force increases. If the applied torque and driving force reach equilibrium before the peak of the curve is reached, the adhesion coefficient is kept at that value. The applied torque can be so large that the slip ratio moves over the peak of the curve. Equilibrium between the applied torque and driving force is never reached and rotational runaway of the wheel occurs, as can be seen when 235 Nm of torque is applied.

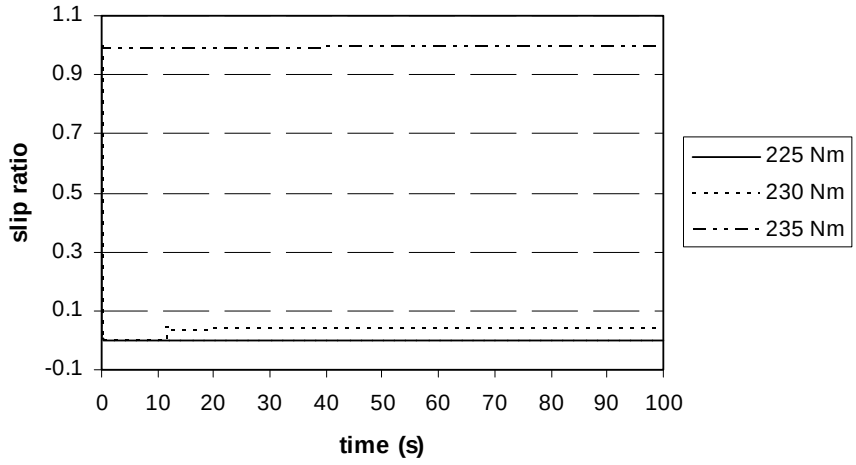

Fig 3.23: Slip ratio for various applied wheel torques.

One method of traction control is to prevent the wheel from slipping. This is done by monitoring if wheel slip takes place and adjusting the applied torque accordingly. Thus, the applied torque is kept below the torque boundary. This is a very simple method of traction control utilizing a form of motor speed control or load torque observer control. Although it is sufficient for traction control, it is not the best method.

A second method is to adjust the applied torque to obtain an optimum slip ratio, once the torque boundary is crossed. If the applied torque is adjusted to achieve the optimum slip ratio, maximum acceleration or deceleration for the specific road surface can be achieved. The acceleration can be higher than when the wheel is under static friction. ABS braking systems operate on this principle of having an optimum slip ratio to achieve maximum braking force. The method of optimum slip ratio control requires a slip detector and an optimum slip ratio observer [33]. The slip detectors determines if the torque boundary has been crossed and thus if the wheel is slipping. This is easily done by monitoring the acceleration of the wheel. The optimum slip ratio observer determines the $\mu_a - \lambda_{sr}$ curve of the particular road surface as well as the optimum slip ratio thereof. It then adjusts the controller commands to obtain the optimum slip ratio.

3.5 Implementation

A major question that arises concerns the physical implementation of the traction control algorithm. The implementation is simple in a single motor vehicle system as it usually only has one control circuit. On the other hand, this implementation becomes more complex in multiple motor systems. Some of these systems have a control circuit at each of the motors (motor controller) as well as a centralized controller (vehicle controller). Fig 3.24 shows such a system using two motors. The traction control algorithm can be implemented in both these circuits. It must be remembered that the communication between the circuits adds a delay to the reaction of the system. It is advisable that the per wheel traction control be implemented in the motor controller as a fast response to changing conditions is required.

A more complex traction control system can be split between the motor and vehicle controllers. The per wheel traction control is implemented in the motor controller and the overall vehicle traction control (lateral control, electronic differential etc.) in the vehicle controller. It is however important to ensure that the communication between the controller is of such a rate as not to delay the response of the system. An example of such a system can be found in [33].

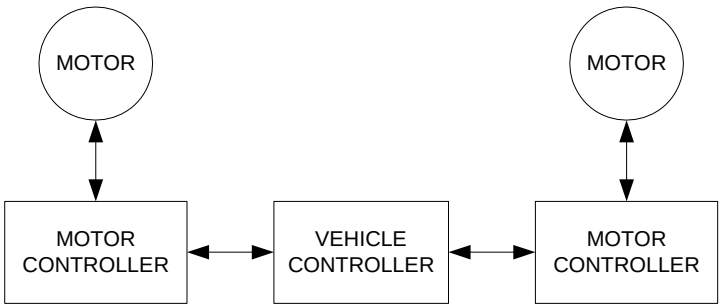

Fig 3.24: Multiple motor system multiple motor control units.

Chapter 4 Battery pack sizing

At this stage in the development of EV's one of the main contributors to its high cost is the energy storage devices such as batteries and ultra capacitors. It is thus critically important, from a cost point of view, to calculate the size of the storage units required accurately. Although a larger than required battery pack would increase the range of the vehicle, the extra cost associated with that increase is very high.

In this chapter two options for calculating the correct battery pack size are presented. The possible inverter topologies, which form part of the electric drive system, as well as the impact of these topologies on the battery pack, are also presented. A specific battery pack chosen for an electric vehicle is also discussed.

It is recommended, by the battery pack manufacturer, that the battery pack undergo a certain number of charge and discharge cycles before it is used in any application. The measurements taken during one of these charge-discharge cycles are also presented to show the cell charge and discharge curves.

4.1. System specifications and topologies

The motor or motors of an EV are the main energy consumers in the EV system. For the actual vehicle designed, it has been specified that the batteries must be able to deliver enough power so that the electric wheel motors are able to run at rated power for an hour. The rated power of the motors to be used in the vehicle is 10.5 kW. Table 4.1 lists the motor specifications. It has been calculated that 16.5 kW's of power is required for a 1500 kg vehicle to travel along a road having a 0 % gradient at a speed of 120 km/h [39]. It can be seen that the two motors will not be running at rated power under these conditions.

Motor Specifications	
Rated Power	10.5 kW
Line Voltage (V_{LL})	173 V rms
Phase Current (I_F)	35 A rms

Table 4.1: In-wheel motor specifications

The in-wheel motor that was designed for the electric vehicle is a permanent magnet motor. This motor operates at almost unity power factor. In this study a power factor of one is assumed, i.e. the power factor angle, φ, is equal to zero.

Lithium-ion cells were chosen for the electric vehicle application. This type of cell is widely used in electric as well as in hybrid vehicles. Cells with a capacity rating of 100, 150 and 200 Ah were chosen. This was due to the fact that these cells have higher energy densities than their lower current rating counterparts. Each of these cells has a minimum voltage of 3 V. The specifications for the cells used can be found in the manufacturer's cell brochure [49].

4.1.1 Inverter topologies

One of the major factors in determining the size of an electric vehicle battery pack is the topology of the inverter between the battery pack and the motor(s). The drive system requires a minimum DC bus voltage so that the inverter output voltage meets the voltage requirement of the electric motors. This DC bus voltage is dependent on the topology of the inverter.

There are three possible system configurations for the EV's electric drive system that can be used, each having advantages and disadvantages. These will be shown when the possible system configuration options are compared. The three options are:

- Half bridge inverter between the electric motor and battery pack (Fig 4.1)
- Full bridge inverter between the electric motor and battery pack (Fig 4.2)
- Half bridge inverter with DC to DC converter (Fig 4.3)

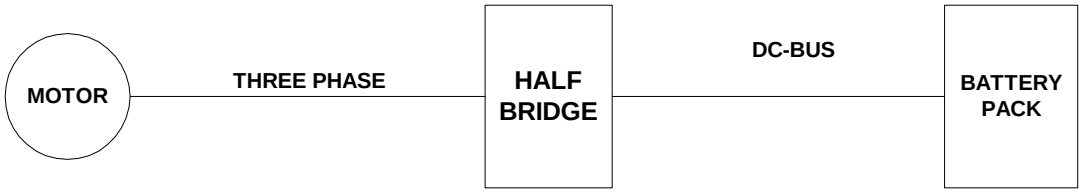

Fig 4.1: System with half bridge inverter

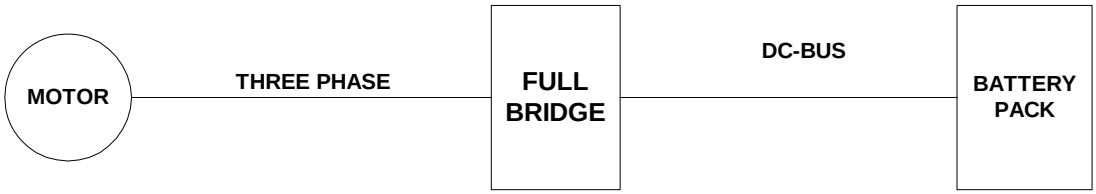

Fig 4.2: System with full bridge inverter

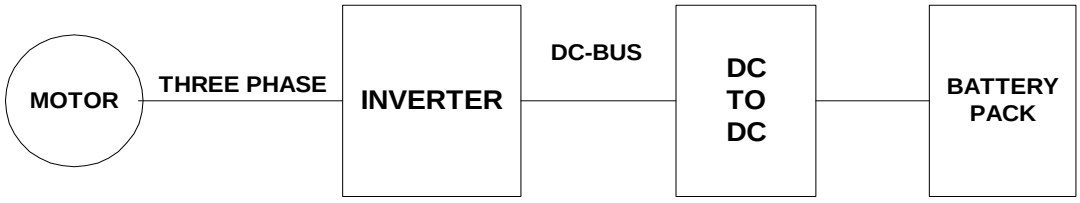

Fig 4.3: System with series connected inverter and DC to DC converter

Each of the EV's motors is driven by its own inverter. The inverters are connected in parallel to the DC bus. Fig 4.4 illustrates this connection. The power required from the batteries increases as the number of inverters increases. This causes an increase in the maximum battery current, requiring a higher current capability from the batteries.

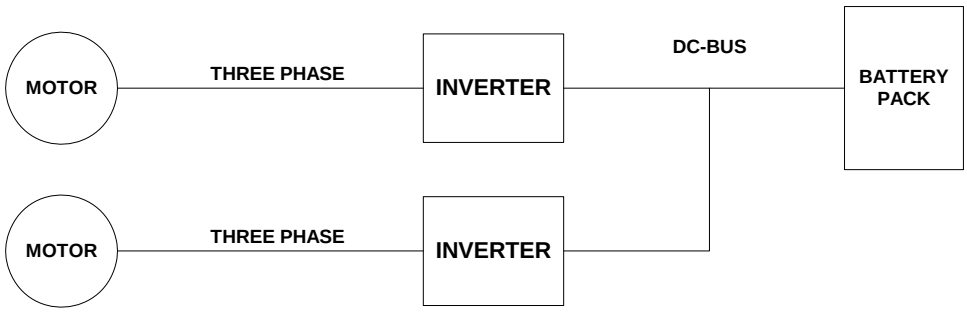

Fig 4.4: Parallel connected electric drives

4.2. Option 1: Battery sized according to motor design

The first battery pack selection method is used when the electric motor specifications have already been determined. The battery pack size is selected to match the voltage, current and power requirements of the motor(s). These voltage and power criteria can be expressed in the form of equations for each of the system configurations. These equations are derived in Appendix C.

A certain number of cells are required for the battery pack to have the energy capacity to meet the requirement of the motor(s). The number of cells required to meet this criterion is given as:

$$n_c = \frac{W_m \cdot n_m}{I_c.h \cdot \eta_{in} \cdot V_c} \qquad (4.1)$$

where n_m is the number of motors, V_c and $I_c.h$ the cell voltage and current capability, η_{in} the inverter efficiency and W_m the required energy. The required energy is given as the required power times the duration, in hours, that the power is required. Equation 4.1 is, however, not valid for the configuration

of Fig 4.2 using a DC to DC converter. The number of cells required when a DC to DC converter is added to the system will be higher because of the efficiency of the converter. The number of cells required when a DC to DC converter is used is given as:

$$n_c = \frac{W_m \cdot n_m}{I_C .h \cdot \eta_{con} \cdot \eta_{in} \cdot V_c} \tag{4.2}$$

The minimum number of cells in the battery pack is determined by the voltage criterion. The number of cells required to meet the criterion depends on the inverter topology used. However, this does not apply to the configuration using the DC to DC converter, as this converter matches the battery pack voltage to the required DC bus voltage. The number of cells required to meet the voltage requirement is given as:

Half bridge: $$n_c = \frac{2\sqrt{2}}{\sqrt{3}} \frac{V_{LL}}{V_C} \tag{4.3}$$

Full bridge: $$n_c = \frac{\sqrt{2}}{\sqrt{3}} \frac{V_{LL}}{V_C} \tag{4.4}$$

It is important to calculate the maximum battery current for a selected number of cells. Some cell types have a limit to the amount of current they can deliver without damaging the cells. The battery pack current is given as:

$$I_B = \frac{3I_L \cdot V_{LN} \cdot n_m \cdot \cos\varphi}{\eta_{in} \cdot V_c \cdot n_c} \tag{4.5}$$

Equation 4.5 only applies to the configurations that do not use a DC to DC converter. For the configuration using a DC to DC converter, as in Fig 4.3, the maximum battery current equation must take the DC to DC converter's efficiency into account. The equation for the maximum battery current when a DC to DC converter is used is given by:

$$I_B = \frac{3 \cdot I_L \cdot V_{LN} \cdot n_m \cdot \cos\varphi}{\eta_{con} \cdot \eta_{in} \cdot V_c \cdot n_c} \tag{4.6}$$

4.2.1 Comparison

A comparison is made between all the possible battery pack options. Some of the options were omitted due to the fact that the battery pack required in these options had to be extremely oversized in energy capacity to meet the voltage requirement. This is especially true when a half bridge inverter is used. Although a larger battery pack would give extended range, the price paid in cost, volume and weight does not make this option viable.

Each of the configuration options (Fig 4.1 to 4.3) has its own advantages and disadvantages. The advantage of using a half bridge inverter is that the number of components used is half that of a full bridge inverter. Only half the number of power electronic modules is required as well as half the number of PWM signals. On the other hand, from equations 4.3 and 4.4, the use of a full-bridge inverter only requires half the number of cell in series to meet the voltage criterion compared to the use of a half bridge inverter. Although the full bridge inverter requires double the number of components, it also allows for non-sinusoidal motor currents. Non-sinusoidal motor currents may be used to improve the performance of the motor.

The battery pack voltage can be matched exactly to meet the requirements of the motor by adding a DC to DC converter without over sizing the battery pack. A price is paid to achieve this. The system's total efficiency is decreased with the addition of the converter. Extra cells are required to compensate for this loss in efficiency. This configuration is only seen as a viable option if this loss is deemed acceptable or an extremely high efficiency converter is used.

Table 4.2 lists the number of cells required to meet the energy capacity required by the electric wheel motors. These are calculated using equations 4.1 and 4.2.

	Without Converter			With Converter		
Current Capacity	100 Ah	150 Ah	200 Ah	100 Ah	150 Ah	200 Ah
Number required	78	52	39	87	58	44

Table 4.2: Number of cells required to meet energy specifications

Table 4.3 shows the comparison of all the viable battery pack options. The comparison shows that it is difficult to meet the voltage requirement and not oversize the battery pack in terms of energy capability when using high current capacity cells, except with the use of a DC to DC converter. It can be seen from Table 4.3 that in most cases, the number of cells required to match the voltage criterion is more than the number required to meet the energy criterion. Over sizing of the battery pack energy capability almost always occurs when a high voltage, low current electric motor is used. The option that best matches the battery pack to the motor is the configuration that uses 150 Ah cells with a full bridge inverter. It is advisable rather to use low capacity cells when a high voltage, low current motor is used.

	half bridge	full bridge			DC to DC converter	
Cell Current Capability (Ah)	100	100	150	200	half bridge 100	full bridge 200
Cells needed for: energy / voltage	78 / 95	78 / 96	52 / 48	39 / 48	87 / 87	44 / 44
Total number of cells used	95	96	52	48	87	44
Number of cell sets in parallel	all in series	2	all in series	all in series	variable	variable
Battery pack voltage (V)	285	144	156	144	variable	variable
Maximum battery current (A)	82.72	163.72	149.57	163.72	100.3	196.4
Battery energy Capacity (kWh)	28.5	28.8	23.4	28.8	26.1	26.4
Battery pack weight (kg)	285	288	275.6	264	261	242

Table 4.3: System configuration comparison

4.3. Option 2: Motor designed according to battery choice

In the previous section, it was seen that the battery pack could not be precisely matched to the electric motor system. The battery pack was mostly oversized to meet the voltage requirements. An oversized battery pack increases the range of the vehicle, but a high price is paid in cost, volume and mass. A match could only be made with the addition of a DC to DC converter, as shown in Fig 4.3. This configuration has the disadvantage of decreased system efficiency with the added power electronics converter.

An alternative method used in designing the system is to choose the battery pack first and then consider the voltage and current design of the electric drive system. More freedom exists in the voltage-current specification than in choosing a battery pack size. The drive system is thus designed to match the battery pack specifications. One of the two inverter topologies, i.e. half bridge or full bridge, is still used. This method, however, eliminates the use of a DC to DC converter to match the battery pack to the motor.

The number of cells is determined by the chosen energy capacity of the battery pack. The number of cells required to obtain the chosen energy capacity is given by:

$$n_c = \frac{W_{bat}}{V_c \cdot I_c . h} \tag{4.7}$$

The battery pack voltage and maximum current can be calculated once the number of cells required for the chosen energy capacity is known. The battery pack voltage and maximum current is given by:

$$V_B = \frac{W_{bat}}{I_C . h} \tag{4.8}$$

$$I_B = \frac{P_{bat} \cdot n_m}{\eta_{in} \cdot V_c \cdot n_c} \tag{4.9}$$

The battery pack voltage and maximum current is independent of the inverter topology, as can be seen from equation 4.8 and 4.9.

Fig 4.5 shows the battery pack voltage and maximum current for a range of energy capacities. The battery pack voltage and maximum current is calculated for the case where two electric motors are driven.

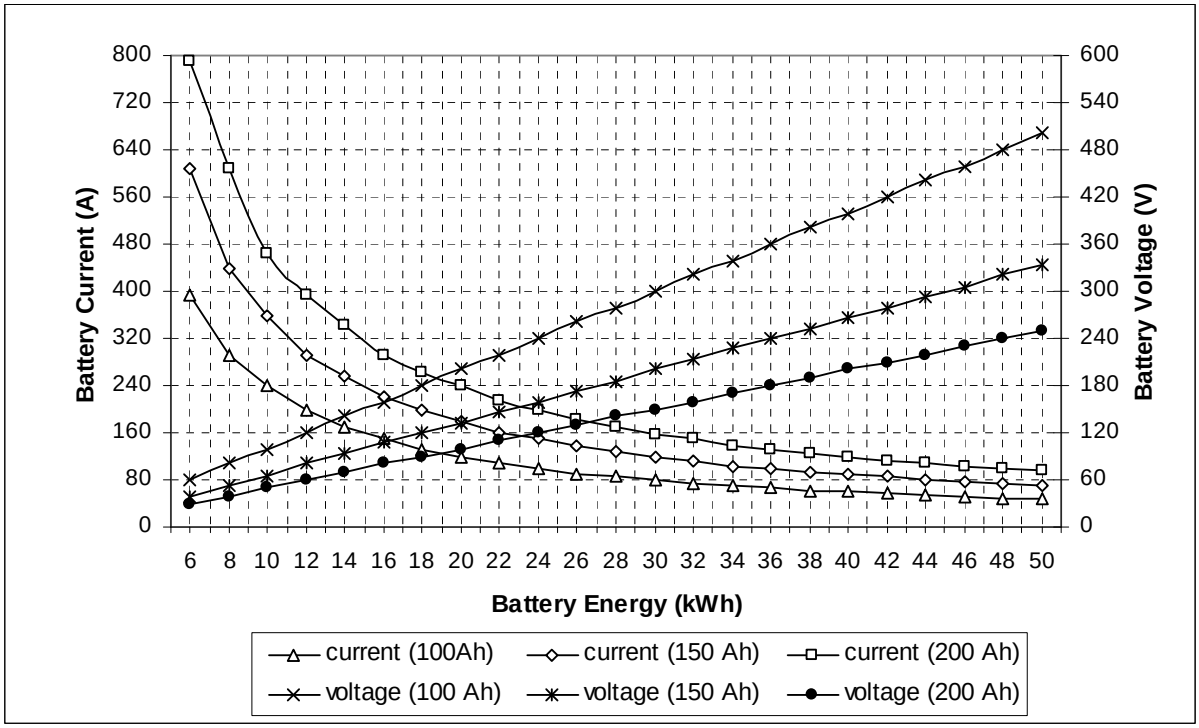

Fig 4.5: Battery current and voltage for two in-wheel motors.

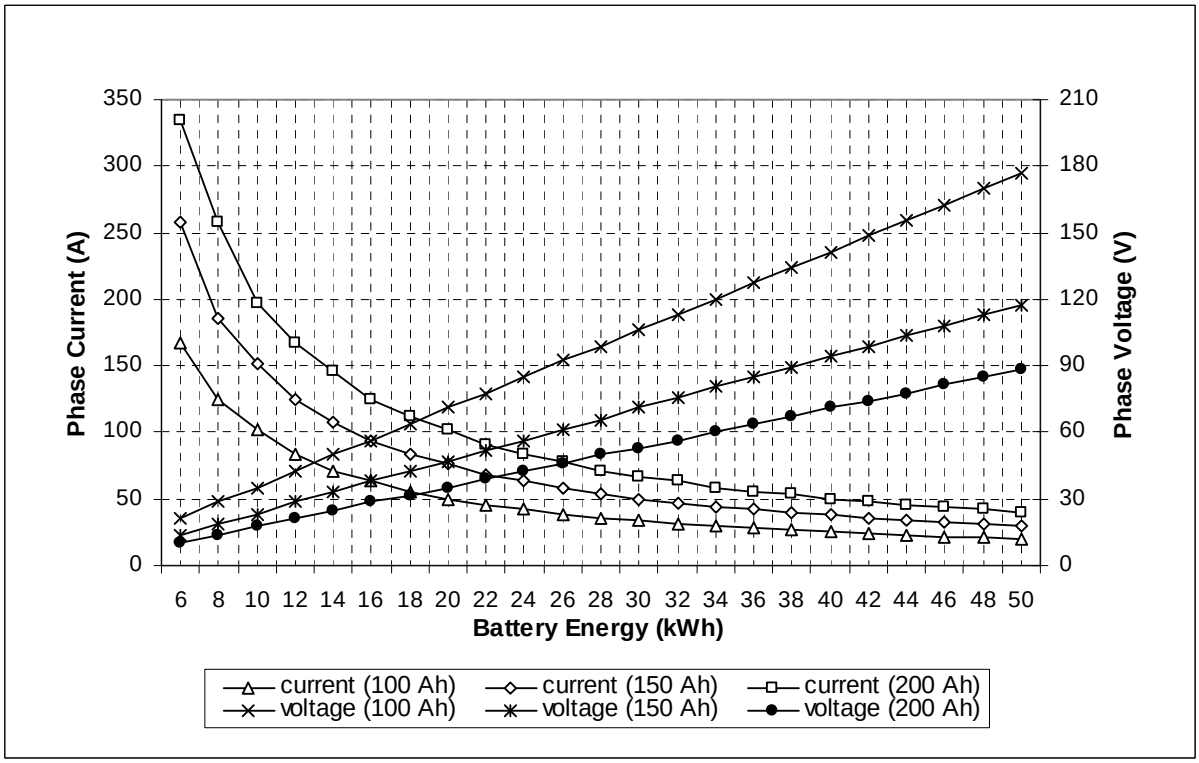

Fig 4.6: Motor phase current and voltage with half bridge inverter.

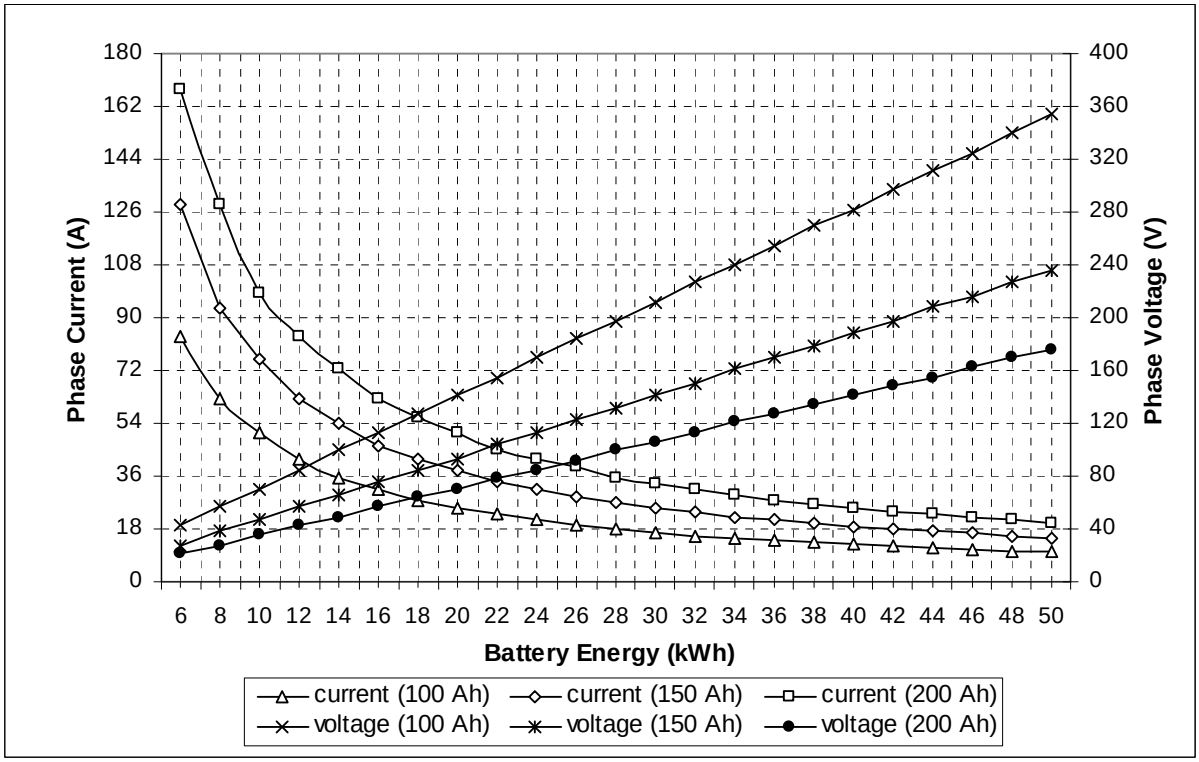

Fig 4.7: Motor phase current and voltage with full bridge inverter.

Although the above method achieves a more precise battery pack size than the previous method, there still exists a small amount of inaccuracy. This is due to the rounding of the number of cells required to obtain the energy capacity. This inaccuracy can be seen in the above figures as well. Ideally the voltage graphs should be a straight line, but as can be seen, they deviate slightly from a straight line due to the rounding of the number of cells required.

4.4. Battery pack choice

The battery selection method explained in section 4.3.2 was used to choose a battery pack size for an EV. It is not that the second method is seen as the best, but as the best for the specific application. In other applications, where the drive motor specifications are fixed, the first method will be the better option. At the stage at which the battery pack selection was made, the motors to be used in the EV application were still in the design phase, thus making the changing of the motor specifications easy.

The motor power rating was kept at 10.5 kW and the voltage and current parameters of the motor were changed to match the battery pack selection. The energy capacity of the battery pack was specified as being able to deliver 10.5 kW, per motor, for an hour. Taking this and the inverter efficiency into account, a 24 kWh battery pack was chosen.

According to the cell manufacturer's brochure [50] the 200 Ah cells are the most cost effective and more importantly, the cells with the highest energy to mass ratio (Wh/kg). For this reason the 200 Ah cells were chosen.

By studying Fig 4.6 and 4.7 it can be seen that the motors will have a relatively low phase voltage and high phase current. This has an impact on the conductor size of the motor windings. A full bridge inverter was chosen to minimize the motor phase current.

The EV system has the following parameters:

Battery energy capacity:	24 kWh
Battery capacity:	200 Ah
Number of cells:	40
Battery pack voltage:	120 V
Inverter topology:	full bridge
Motor phase current:	41.9 A
Motor phase voltage:	84.9 V rms

This battery pack selection was used in the next chapter during the laboratory testing of an Energy Management system.

4.5. Battery pack system

The battery cells are not the only parts of the battery pack system received. The battery pack system also contains a battery charger and a Battery Monitoring System. These were all received with the battery cells purchased. Photos of cells, charger and BMS can be found in Appendix E.

Lithium based battery cells, although providing excellent performance should be operated under controlled condition. These cells are negatively affected by over voltage and over current. These condition lead to cell damage on a chemical level that is irreversible. It is thus of the utmost importance that the operation of the battery pack is closely monitored. This is the function of the BMS. The BMS is equipped with measuring circuits able to measure each cell voltage as well as the battery pack current. The BMS detects any cell over voltage or current and either alerts the external system of this condition or, if the BMS is equipped with the necessary circuitry, takes action to protect the battery pack from damage. The BMS also uses the measurements to calculate the state of charge (SOC) of the cells. The SOC is a indication of the amount of charge left in the cells and can help determine the distance the vehicle can travel before running out of charge. The BMS uses the SOC to

determine the voltage and current limits of the cells. Complex cell models are used to calculate the SOC of the cells. Even the operation history of the cell plays a part in calculating the SOC of the cell. In some cases, the BMS unit stays with the battery pack for the duration of it life.

Large lithium based battery packs usually come equipped with their own chargers. These chargers allow for variable current charging of the cells. What makes these chargers unique is that they are in communication with the specific BMS unit. This ensures optimum charging of the cells as well as protection of the cells against overcharging.

The 40 cells used to make up the battery pack are all connected in series. Fig 4.8 shows the chosen battery pack layout used in the laboratory measurements in the next chapter. The specific layout was chosen to simplify the series connection of the cells as well as the connection of the BMS measurement circuit to each of the cells.

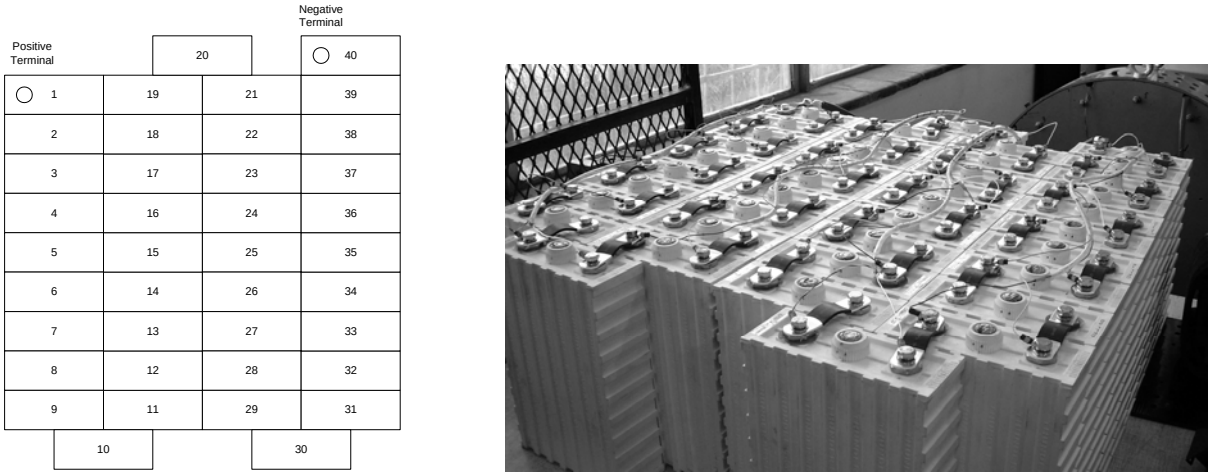

Fig 4.8: Layout and photo of Lithium-ion battery pack.

4.6. Charging and discharging of battery pack

The user manual of the Thundersky lithium ion cells specifies that the cells should be taken through 3-5 charge-discharge cycles before they are used in an application. The cells are, as far as possible, fully charged and then fully discharged during such a cycle. This is to activate the chemical processes within the cells. The recommended charge and discharge current is specified as 0.3 C. In section 4.4 200 Ah cells were chosen for the specific EV. Thus, the recommended charge and discharge current is equal to 60 A.

There is a specific charging method which is used to ensure optimum performance as well as cell protection. This method has two charging regions i.e. constant current and constant voltage charging. Constant current charging takes place during approximately the first 80% of charging and constant

voltage during the last 20%. During constant current charging, as the name implies, the charge current is kept constant. The cell voltage increases as the cells are charged. Constant current charging is continued until the cell voltage limit is reached. Once the limit is reached, the charging method is changed to constant voltage charging. During this method the cell voltage is kept relatively constant. This is achieved by continuously decreasing the charge current. This ensures that the cells are not over charged and thus damaged. The charge current can be increased again in some instances to ensure maximum charging of the cells. Then the constant voltage charging cycle starts again. This adjusting of the charge current is automatically handled by the interaction of the BMS and the charger. Fig 4.9a shows the current and charging curves for the battery pack. It can be seen that the constant voltage charging cycle was repeated four times, between 170 and 185 minutes, before the charger was switched off. Fig 4.9b shows the state of charge of the battery pack over the course of charging. The SOC of the battery pack is given as ampere hours remaining.

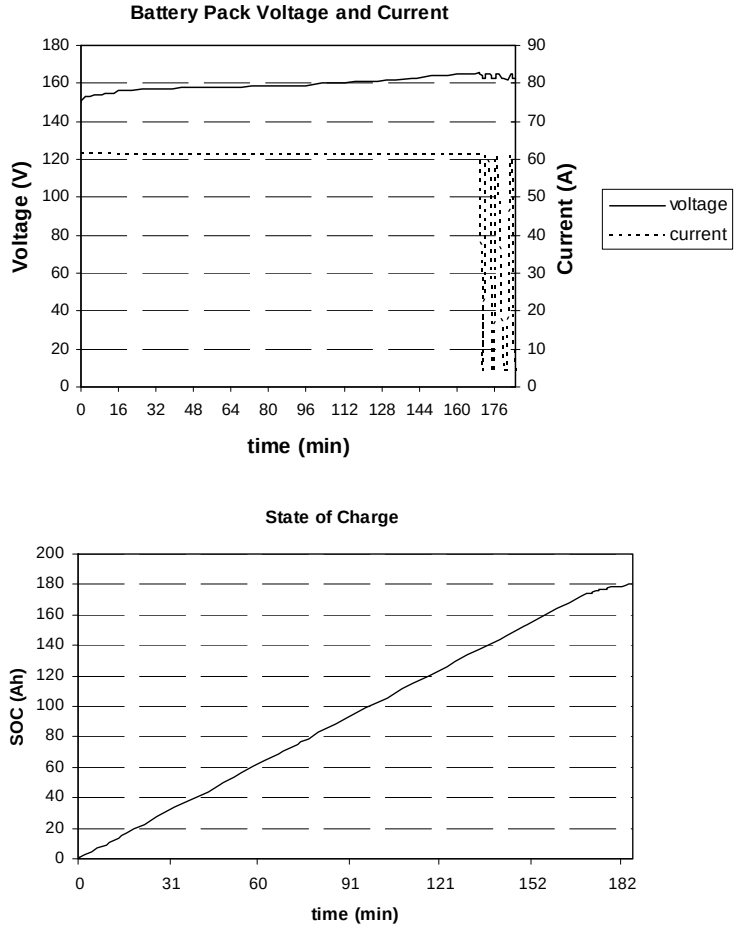

Fig 4.9: Measured a) battery pack current and voltage and b) battery pack state of charge.

The charge-discharge cycles require that the cells are discharged at a constant current. This requires a current controlled load system. Such a load system is easily constructed with the converter circuit shown in Fig 4.10. The current drawn from the battery pack is controlled by controlling the duty cycle of the converter. A control algorithm can be designed, but for the discharging of the cells it was decided to adjust the duty cycle manually to obtain the required battery discharge current. An electronic load system with current control is designed in the following chapter.

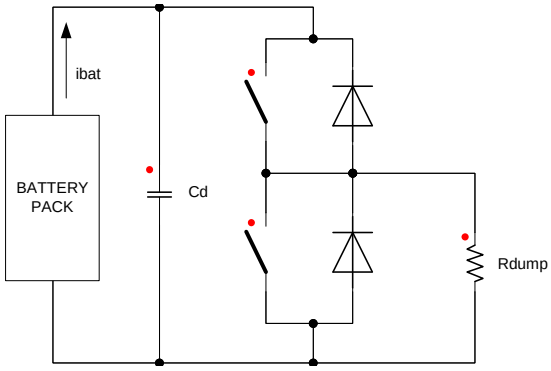

Fig 4.10: Battery discharge circuit

Fig 4.11 shows the battery pack voltage and current during the discharge cycle and Fig 4.12 the SOC of the battery pack. The SOC before the discharge of the cells commenced is given as 180.3 Ah. Thus, with a constant discharge current of 60 A it can be estimated that the cells will discharge for approximately 3 hours. Fig 4.12 shows that the cells took 183 minutes to discharge.

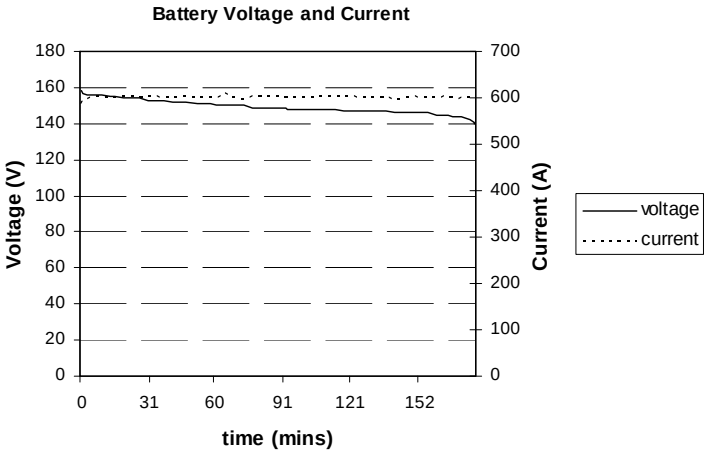

Fig 4.12: Battery state of charge during discharge.

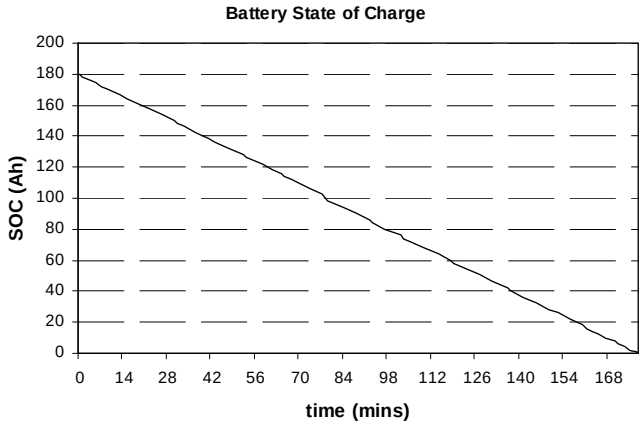

Fig 4.12: Battery state of charge.

Fig 4.12 shows the voltage and thus charge distribution through the battery pack. It can be seen that some cell voltages are somewhat higher or lower than the rest. This unequal distribution of charge limits the capacity of the battery pack as a whole. The BMS changes the charging and discharging conditions according to individual cell limits. Thus, if one cell reaches its limit before the others, the charging or discharging is stopped meaning the other cells are not at capacity. This is especially true for the discharging of the cells.

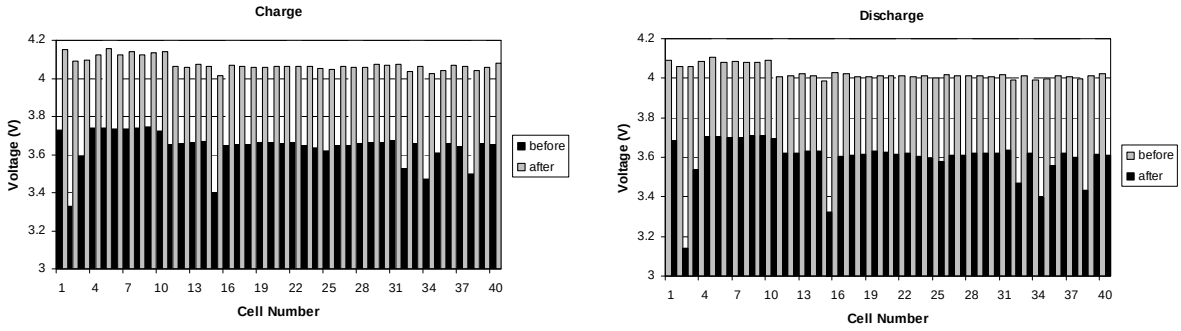

Fig 4.13: Measured cell voltage distribution before and after charging and discharging

The datasheet of the Thundersky cells shows the voltage charge and discharge curves for the various currents, including 0.3 C or 60 A. Fig 4.13 and 4.14 show the measured charge and discharge voltage curves obtained during one charge-discharge cycle for four cells. The location of these cells can be found in Fig 4.8. These curves compare well with the curves found in the datasheet.

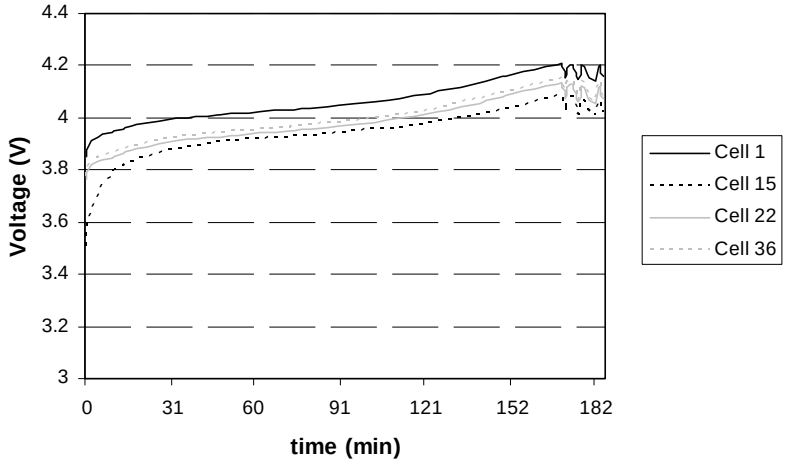

Fig 4.14: Measured cell voltages during charging

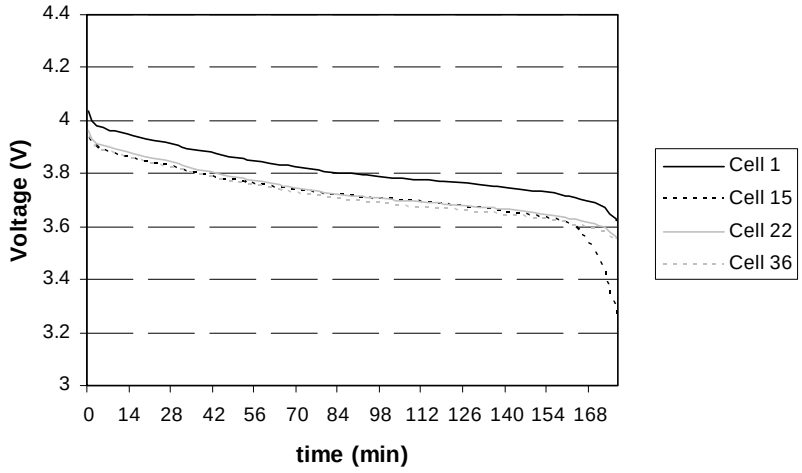

Fig 4.15: Measured cell voltages during discharging

Chapter 5 Energy management system

Aspects concerning a proposed energy management system for an EV are dealt with in this chapter. The function of the energy management system (EMS) is to control the flow of power between the storage devices and the electric motors. This system includes auxiliary storage devices, the power electronic converter used to manage the flow of power and the control circuitry and algorithm needed for the power electronic converters. Fig 5.1 shows a block diagram of the EV's energy system.

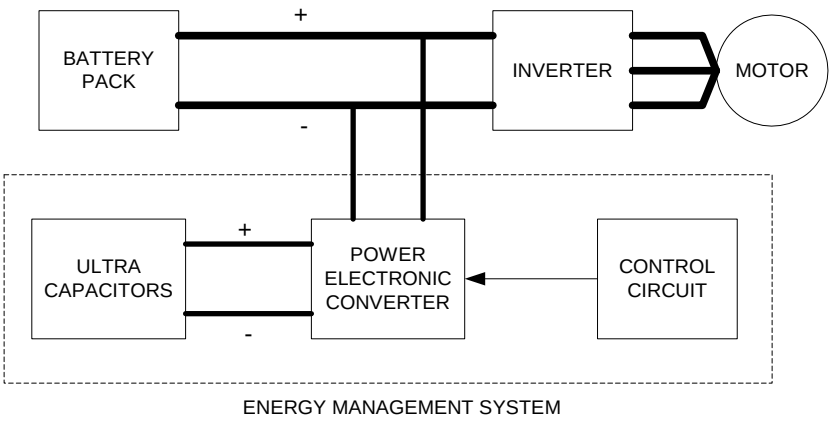

Fig 5.1: Vehicle energy system block diagram.

The beginning of the chapter starts by giving background information about the auxiliary storage devices used, i.e. ultra capacitors. The physical construction of ultra capacitors is explained and is compared to the construction of conventional capacitors. The power electronic converter used in the energy management system as well as the control algorithm for the power electronic converter is described. A system model is implemented in software and the simulation results, using this model, are presented. Finally, the results of laboratory testing of the EMS are presented.

The EMS configuration, shown in Fig 5.1, has been widely used, not only in the field of EV's [34], but in other electric applications such as hybrid vehicles [35] and even electric elevators [36]. A few negative aspects were found in the evaluation of the conventional system of Fig 5.1. In the final part of the chapter, a new energy system topology is presented and explained. The new topology was designed to eliminate some of the negative aspects and improve the energy management system as a whole.

5.1. Ultra capacitors

Ultra capacitors are also known as double layer capacitors (DLC's). Although only coming to the fore in the last decade, ultra capacitor technology has been around since the 1960's. The DLC technology was developed by the Standard Oil of Ohio Research Centre in 1961 [37]. The noticeable difference between conventional capacitors and DLC's is the high capacitance that is obtained using the technology, able to reach thousands of Farads. To some people, a 2700 F capacitor is something of a myth.

Three basic capacitor constructions exist as shown in Fig 5.2. The first of the three is the electrostatic capacitor. Electrostatic capacitors are constructed from two metal films separated by an insulating material, thus forming two electrodes with a dielectric material in between. Examples of such dielectric materials are ceramics and glass mica. These electrodes have no polarity. A uniform electric field is created in the dielectric material when a potential is placed across the electrodes. The disadvantage of electrostatic capacitors is that high capacitance can not be obtained with this construction.

Equation 5.1 is the standard equation for calculating the capacitance. Electrostatic capacitors have a relatively high d value, i.e. the distance between the charges on the plates, thus giving relatively small capacitance values.

$$C = \frac{\varepsilon_0 \varepsilon_r A_P}{d} \tag{5.1}$$

In equation 5.1, A_p is the equivalent area of the plates, ε_o is the permittivity of free space and ε_r is the permittivity of the dielectric material separating the plates.

Electrolytic capacitors are similar in construction to electrostatic capacitors except that they contain electrolytes instead of dielectric materials. Electrolytic capacitors contain two different electrolytes. One of the electrolytes is in direct contact with one of the capacitor electrodes. This electrolyte serves as an ionic conductor layer. The other electrode is made from an etched metal film. This electrode receives an electrical potential during manufacturing by immersing it in a second electrolyte. It is due to this potential that the electrodes of an electrolytic capacitor have a certain polarity. This electrolyte forms an alumina (Al_2O_3) layer on the anode of the capacitor, forming a separator barrier. The two electrodes are rolled together, each electrode pair being separated by a layer of Kraft paper. When an electric potential is placed across the electrodes of the capacitor, a uniform electric field is formed in the alumina layer and a decaying field in the cathode electrolyte according to the Poisson equation. As the alumina layer can be made a lot thinner than the dielectric layer in electrostatic capacitors, a higher

capacitance can be obtained with the electrolytic capacitor construction. On the other hand, the ionic conductor layer has a lower breakdown voltage than the dielectric material. Thus, electrostatic capacitors have a higher voltage limit than electrolytic capacitors.

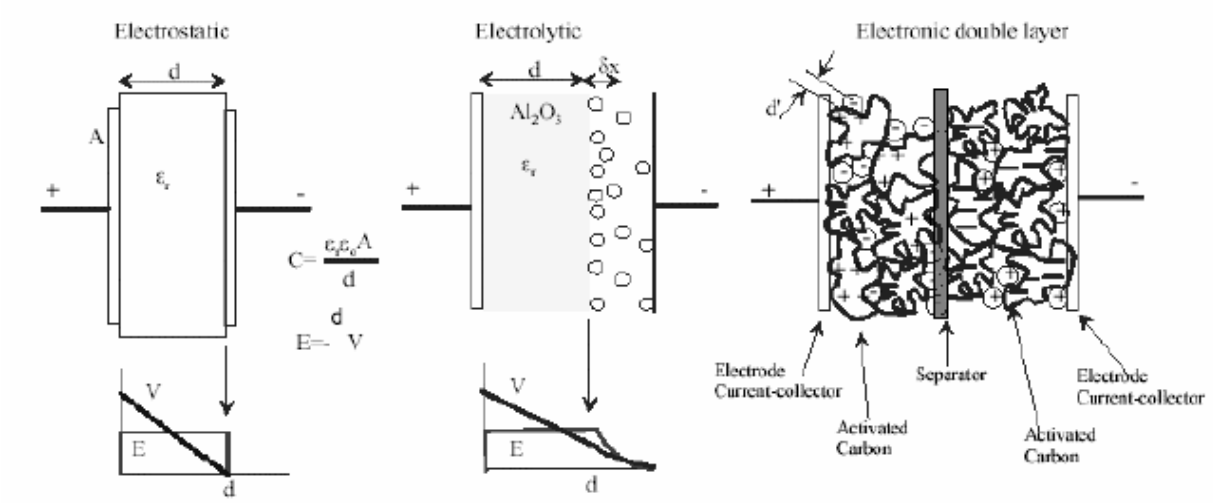

Fig 5.2: Physical construction of electrostatic, electrolytic and ultra capacitors [38].

Ultra capacitors are constructed from two almost identical layers, separated by a barrier. It is from these two layers that the name double layer capacitor comes. These layers are known as Helmholtz layers. A Helmholtz layer consists of a metal foil plate with very porous carbon layer deposited on it. This carbon is also known as active carbon because of its electric potential. The carbon is impregnated with an organic electrolyte. The polarity of the electrolyte depends on the polarity of the electrode that is required. Each of the layers serves as a capacitor on its own, but two are required for the capacitor to have two metal electrodes. Equation 5.1 shows that in order to obtain a high capacitance the surface area of the capacitor plates, A_p, needs to be increased or the distance between the charges, d, needs to be decreased. The ultra capacitor construction does both. The porous nature of the carbon causes the electrode to have an enormous surface area. The size of the pores is such that the ions in the electrolyte easily fit inside. The distance between the charges is in the order of one atomic thickness. Thus, a very high capacitance can be obtained. This extremely small distance causes the capacitors to have a very low breakdown voltage; typically around 3 V. Ultra capacitors, thus, are not suited for very high voltage applications.

Battery technology is of such a nature that it has a relatively high specific energy, but low specific power. This is shown in the Ragone plot in Fig 5.3. The Ragone plot gives the specific energy versus specific power for energy storage devices. These are also known as energy densities and power densities. Batteries have low specific power due to the fact that they rely on an electrochemical process to deliver or receive charge. Electrochemical processes need time to activate. That is why batteries are

damaged when quick power is required or delivered. Unfortunately, both a high specific energy and specific power are required for EV applications. It seems that a combination of storage devices would be needed in an EV.

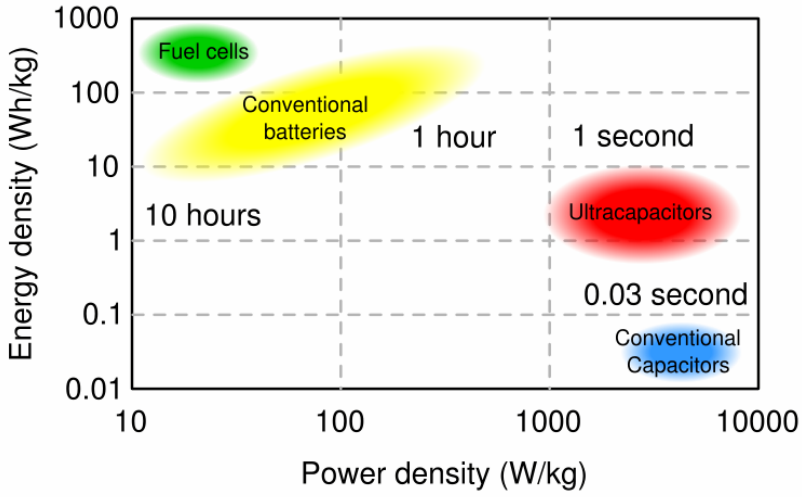

Fig 5.3: Ragone plot for energy storage devices [38].

It can be seen that capacitors make an excellent auxiliary storage device with its high specific power. Capacitors rely on an electrostatic process to supply or accept power. The electrostatic process activates almost instantaneously, unlike electrochemical processes. Electric vehicles require a reasonable amount of specific energy from their auxiliary storage devices. This makes conventional capacitors unsuitable because of their low specific energy. On the other hand, ultra capacitors, with their higher specific energy, make ideal auxiliary storage devices.

Ultra capacitors and super capacitors are sometimes used to name the same capacitor technology, but in actual fact these are two different types of capacitor technologies. Both these capacitors are known as double layer capacitors. Ultra capacitors, as mentioned, are constructed from two Helmholtz layers separated by an insulating layer. They are known as Electronic Double Layer Capacitors. The super capacitors construction on the other hand is a combination of a capacitor and a battery cell. One of the layers is a Helmholtz layer and the other, half of an electrochemical cell. Super capacitors are also known as Electrochemical Double Layer Capacitors. The half cell is added to increase the breakdown voltage of the capacitor and still retain the high capacitance. The addition of the half cell decreases the specific power of the capacitor however. Super capacitors are mainly used as main energy storage devices where batteries cannot be used. Super capacitors, thus, are not capacitors in the true sense of the word.

5.2. Capacitor sizing

It is critically important to determine the exact amount, both in size and Farads, of ultra capacitors needed for an EV application. This is crucial due to the fact that there are certain cost, volume and weight constraints when using ultra capacitors, as with battery selection. The size of the ultra capacitors is dependent on energy system specifications.

The first specification that has an impact on the sizing of the ultra capacitors is the DC bus voltage or battery voltage. In most applications the ultra capacitor maximum voltage is chosen to be lower than that of the battery voltage. It is usually chosen to be between 80 - 90% of the DC bus voltage. Ultra capacitor units are manufactured in discrete voltage values. The precise maximum voltage is chosen to match these discrete values.

Although the ultra capacitors are used for their power capability, it is still necessary to determine the energy capability required from the capacitor pack. The energy capability is the product of the peak power and the duration during which it is to be able to receive or deliver this power. The energy capability of the capacitors pack is given by:

$$E_{uc} = P_{\max} t \tag{5.2}$$

The amount of energy that can be received or delivered by a capacitor is given as

$$E_{uc} = \tfrac{1}{2} C_{uc} \left(V_{start}^2 - V_{end}^2 \right) \tag{5.3}$$

where C_{uc} is the capacitance and V_{start} and V_{end} the start and end capacitor voltages. By rewriting equation 5.3 and substituting into equation 5.2, the equation for the capacitance of the ultra capacitor pack is as follows.

$$C_{uc} = \frac{2 P_{\max} t}{\left(V_{start}^2 - V_{end}^2 \right)} \tag{5.4}$$

The ideal voltage range in which to operate the ultra capacitors is from 0 V to its maximum voltage rating. It is firstly not advisable to operate the ultra capacitors at their maximum voltage rating. If by some unforeseen circumstance the voltage is taken over this voltage, irreversible damage to the capacitors would take place. The risk of damaging the ultra capacitors is considerably reduced if a small buffer voltage is implemented. Furthermore, the minimum voltage can never be equal to zero

under normal operating conditions due to the fact that the capacitor current will strive to infinity to adhere to the power equation. It is for this reason that the ultra capacitors should first be charged to a minimum voltage, using a constant current method, before normal operation commences. The minimum operating voltage is determined by the maximum allowable capacitor current. Fig 5.4 shows a normalized plot of the amount of energy stored in a capacitor versus capacitor voltage. It can be seen that if the ultra capacitor is operated from 0.4 to 1, thus 60% of it voltage range, it can still store up to 84% of its total energy capacity.

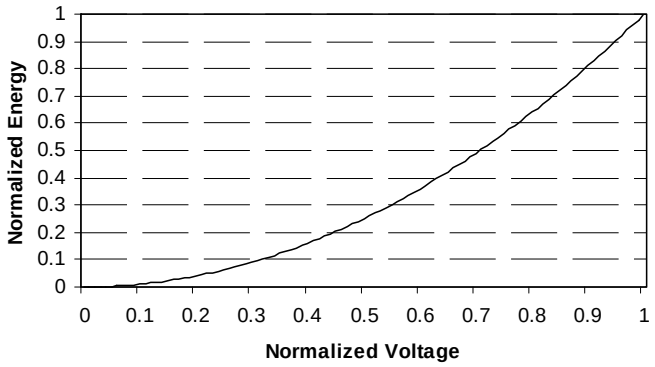

Fig 5.4: Capacitor energy versus voltage.

The next step is to determine the amount of ultra capacitor cells that are required to meet the specified maximum voltage. The equation for the number of cells required is given as:

$$n_s = \frac{V_{uc}}{V_{cell}} \tag{5.5}$$

where V_{uc} is the chosen ultra capacitor voltage limit and V_{cell} the voltage limit of the ultra capacitor cells that are used.

It is possible that the number of cells required in series can decrease the total capacitance to such an extent that the capacitance of each cell required is outside the capacitance ranges available. Capacitor sets are placed in parallel to increase the total capacitance of the capacitor pack. The equation for the number of parallel sets required is given as:

$$n_p = \frac{C_{uc}}{C_{cell}} n_s \tag{5.6}$$

where C_{uc} is the required capacitance of the ultra capacitor pack.

It can be seen from equation 5.6 that the individual cell capacitance needs to be chosen. This is a trial and error process. Aspects such as cost and weight need to be taken into account when choosing a capacitance value.

As mentioned before, the battery pack determines the maximum voltage of the ultra capacitor pack. The same battery pack chosen in Section 4.4 was used. The nominal battery voltage is 120 V. A maximum capacitor voltage of 105 V was chosen. This is 87.5% of the battery voltage. The energy specification, for the particular system, was specified as being able to deliver or receive 20 kW of power for 7 seconds. Using equation 5.2, the energy capability of the capacitor pack is given as 140 kJ.

The next step is to determine the operating voltage range of the capacitor pack. The maximum allowable capacitor current was chosen as 1000 A. Although ultra capacitors can handle these peak currents with ease, they negatively affect the other components in the system. This will be discussed at a later stage. The peak power that can be returned to the energy system of the EV is equal to the 20 kW [39]. From this power and the maximum peak current, the minimum capacitor voltage is calculated as 20 V. If a 5 V voltage buffer is implemented, the operating voltage range of the capacitor bank is from 20 - 100 V.

By using equation 5.4, the capacitance of the capacitor pack required to meet the energy capability is calculated as 29.17 F. The specific ultra capacitor units used is Maxwell's BMOD0052 E015. This unit contains series connected ultra capacitors. It has a voltage rating of 15 V and a total capacitance of 52 F. This unit was chosen as its capacitance value is in the middle of the available values. It is possible to increase or decrease the capacitance of the capacitor pack by replacing the individual cells. Seven of these units are required to meet the maximum voltage specification. By using equation 5.6, the number of parallel sets is calculated as 4 sets. Table 5.1 lists the full specification of the ultra capacitor pack, including size, weight and cost.

Units in series	7
Parallel sets	4
Total number of units	28
Unit capacitance (F)	52
Total capacitance (F)	29.7
Operating Voltage (V)	20 - 100
Energy Capacity (kJ)	142.6
Unit dimensions (mm)	218 x 85 x 44
Total Mass (kg)	19
Total Volume (l)	23
Total Cost	R 21 915.00

Table 5.1: Ultra capacitor pack specifications (Maxwell units)

The Maxwell unit given in Table 5.1 was not used during the laboratory testing of the EMS. Other capacitors manufactured by Epcos Ltd. were available at the University of Stellenbosch. These are shown in Fig 5.5. The ultra capacitor units that were used have a capacitance of 67 F and a maximum voltage of 40 V each. Two of these units were used in series. Using equation 5.3, the energy capability is calculated as 100.5 kJ. This assumes that an operating voltage of 20 - 80 V is chosen.

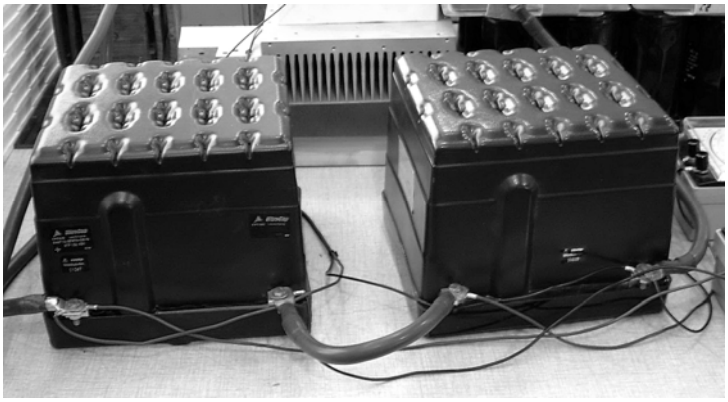

Fig 5.5: Epcos ultra capacitors.

5.3. Energy management circuit

The function of the energy management system is to control the flow of power in the energy system, in such a way as to protect the batteries from peak power as well as high rates of change in the power. Ultra capacitors, with their high specific power, can be used as an auxiliary storage device, acting as a buffer between the batteries and the electric drives.

The simplest circuit that can be implemented is by connecting the ultra capacitors in parallel with the batteries. Although this strategy buffers the battery from power surges, it is a very ineffective way of energy management. Firstly, there is no control over any of the currents and thus the power flowing in the energy system. Secondly, the capacitor voltage ranges around the DC bus voltage. Only a small region of the operating voltage and thus energy capability of the capacitors are used.

A more effective energy management circuit is obtained with the addition of a power electronic converter, as shown in Figs 5.1 and 5.6. The bi-directional DC to DC converter in Fig 5.6 allows for control of the capacitor current and thus, indirectly control of the battery current. The converter also matches the capacitor voltage to the DC bus voltage, allowing for full usage of the capacitor operating voltage range.

A buck-boost converter was chosen as converter topology. Fig 5.6 shows the circuit diagram of the energy system with the converter circuit. A buck-boost converter allows for bi-directional flow of power. The direction of flow is controlled by the switching of switches S1 and S2. Two basic switching methods exist. Fig 5.7 shows these two modes. In the first method, only one switch is switched, depending on the mode of operation that is required. When current is required to flow from the ultra capacitor pack, either to deliver power to the load or to charge the batteries, a boost converter is formed by commutating switch S2 and the diode D1. When current is required to flow to the ultra capacitor pack, a buck converter is formed by the commutating S1 and the diode D2. A power direction discriminator is required to determine the direction of power flow and thus the mode of operation that is required.

The second method of switching entails complementary commutating of the switches, hereby combining the two modes as shown in Fig 5.7. The converter is able to continuously switch between positive and negative current. This is the method used in the study of the EMS.

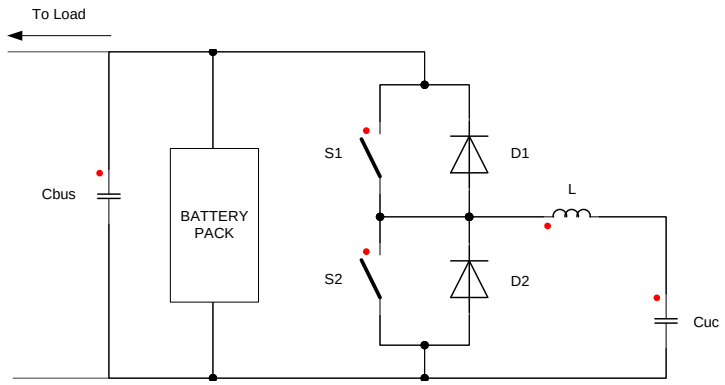

Fig 5.6: Energy system, with battery pack, power converter and ultra capacitors.

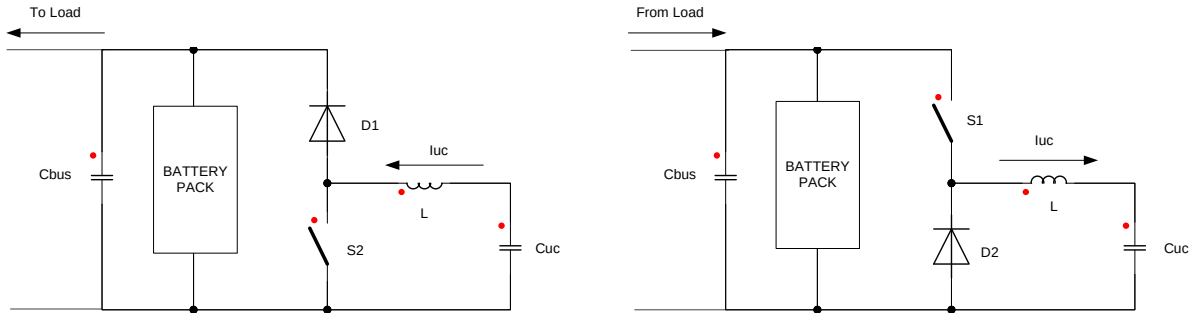

Fig 5.7: Converter in (a) boost mode, (b) buck mode.

The converter topology of Fig 5.6 is not the only topology that can be considered. Many studies have utilized other converter topologies for various reasons [40] [41]. It is the aim of the study to investigate the working of an energy management system. Once the system is to be implemented, a specific converter topology can be chosen that suits the needs of the specific application.

5.4. Control strategy

The aim of the energy management system is to control the flow of current and thus power in the energy system in such a way as to protect and prolong the lifecycle of the batteries. The battery current can, however, not be directly controlled with the presented circuit. Fig 5.8 shows the energy system and all the main currents flowing in it. It also shows the current direction used throughout the thesis. The battery and ultra capacitor charging current and a load current into the energy system are taken as positive. Thus, the load, battery and ultra capacitor current is positive during regenerative braking and negative during motoring mode. The node current equation can be obtained by applying Kirchoff's current law to node A. The equation is given as

$$i_{load} = i_{bat} + i_{con} \tag{5.7}$$

Equation 5.7 shows that the battery current, i_{bat}, can be controlled by controlling the converter current, i_{con}. Furthermore, the converter current is proportional to the capacitor current, i_{uc}, through the duty cycle of the converter. Thus, the battery current can be indirectly controlled by controlling the ultra capacitor current.

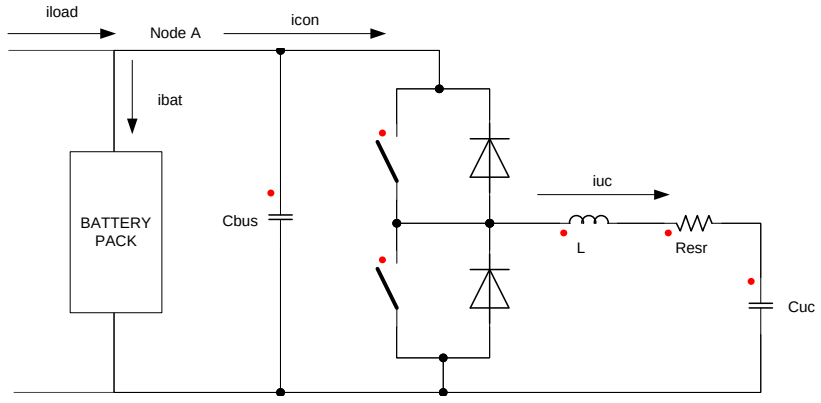

Fig 5.8: Energy system showing main currents.

Batteries, especially Lithium Ion cells, are damaged by currents higher than their rated current as well as by high rates of change in the current. These conditions occur during acceleration of the vehicle and especially during regenerative braking. The energy management system should firstly limit the battery current and secondly control the rate of change of the battery current. Fig 5.9 shows a block diagram representation of the system to achieve these. The load current is measured and used to determine the battery current reference. The battery current reference is determined by means of a limiting function followed by a delay function. The design of these is discussed in sections 5.7.1 and 5.7.2. The ultra capacitor current reference is determined from the battery current reference, according to equation 5.7. Finally, a PI controller is used to control the ultra capacitor current according to the current reference. The design of the PI controller is discussed in section 5.6.

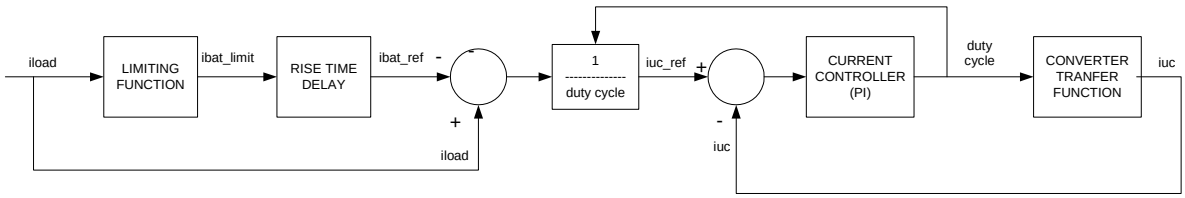

Fig 5.9: Energy management control block diagram.

5.5. EMS circuit model

A transfer function of the system is needed to be able to design the ultra capacitor current PI controller. Various methods can be used to derive the transfer function of the system. What makes this process a difficult one is the switching of the converter which adds a non-linearity to the system. A method for determining the transfer function of power converters was developed by R.D. Middlebrook and S Cuk [42]. This method is used to derive the transfer function of the power electronic converter used in the EMS.

The Middlebrook and Cuk method was developed to derive the transfer function of a power electronic converter that has one input voltage and one output variable. This output variable can either be the output current or output voltage of the converter, depending on the control strategy. The output current, i_{uc}, is the output variable. However, the converter used in the EMS has two input voltages i.e. the bus voltage, V_{bus} and the capacitor voltage, V_{uc}. The transfer function of the two input voltage circuits can be derived by applying the super positioning principle to the converter circuit. A transfer function is derived for each of the input voltages separately. The Middlebrook and Cuk method can now be applied to take the switching of the converter into account. The derivation of the transfer functions is given in Appendix D.

The equations for the capacitor current are given as:

$$I_{uc}(s) = d(s)V_{bus}\frac{\frac{1}{L}s}{s^2 + \frac{R_{esr}}{L}s + \frac{1}{LC_{uc}}} \tag{5.8}$$

when the input voltage V_{uc} is set equal to zero.

$$I_{uc}(s) = -V_{uc}\frac{\frac{1}{L}s}{s^2 + \frac{R_{esr}}{L}s + \frac{1}{LC_{uc}}} \tag{5.9}$$

when the input voltage V_{bus} is set equal to zero.

The super positioning principle is applied by adding equations 5.8 and 5.9 at the same time. The ultra capacitor current function now becomes:

$$I_{uc}(s) = [d(s)V_{bus} - V_{uc0}]\frac{\frac{1}{L}s}{s^2 + \frac{R_{esr}}{L}s + \frac{1}{LC_{uc}}} \tag{5.10}$$

It can be seen from equation 5.10 that the function has a zero at the origin of its root locus plot. This zero acts as a differentiator. A prediction can be made concerning the open loop step response of the system. The differentiator will cause an extremely high overshoot in the capacitor current. The exact value of this overshoot peak can be found by obtaining the step response of the system of a software package.

In equation 5.10, the term, $d(s)V_{bat} - V_{uc}$, is equal to the voltage across the inductor and the equivalent series resistance. There are thus two conditions where the ultra capacitor current will be equal to zero. The first is if the converter switches are left open and the other if the voltage across the inductor is equal to zero. The voltage across the inductor is equal to zero when $d(s)V_{bus}$ is equal to V_{uc} and thus $d(s)$ equal to V_{uc}/V_{bus}.

Equation 5.11 is multiplied by the term V_{bust}/V_{bus}, which is the same as multiplying the equation with one, becoming:

$$I_{uc}(s) = V_{bus}\left[d(s) - \frac{V_{uc}}{V_{bus}}\right]\frac{\frac{1}{L}s}{s^2 + \frac{R_{esr}}{L}s + \frac{1}{LC_{uc}}} \tag{5.11}$$

The input to the system is the duty cycle of the converter, d(s), as shown in Fig 5.9. Fig 5.10 shows the block diagram implementation of equation 5.11 as implemented in MatLab/Simulink.

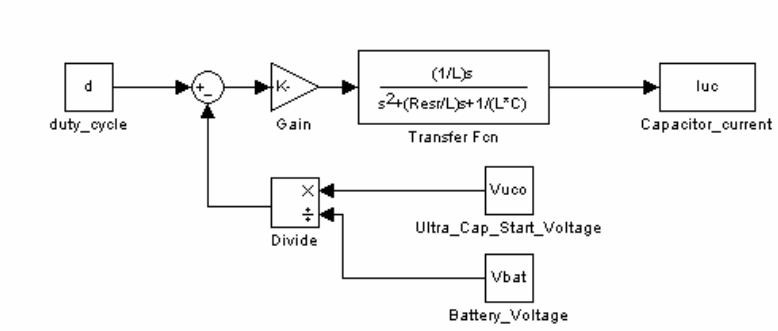

Fig 5.10: MatLab/Simulink block diagram of equation 5.11.

It must be possible to be able to calculate the battery current by using the model. The battery current is calculated with the node equation, i.e. equation 5.8. This equation can be rewritten to calculate the battery current using the ultra capacitor current. The equation for the battery current, in the s domain, is implemented in Fig 5.11 and is given as:

$$I_{bat}(s) = I_{load}(s) - d(s)I_{uc}(s) \tag{5.12}$$

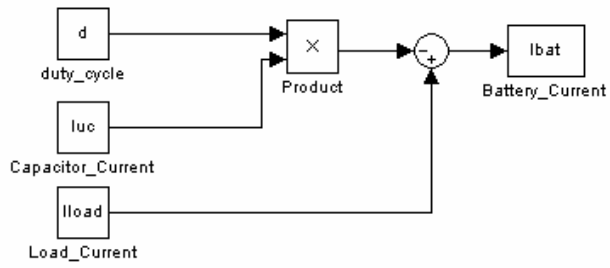

Fig 5.11: MatLab/Simulink block diagram to calculate battery current.

Many cell models exist for the different battery technologies. Each of these models varies in accuracy and complexity [44] [45]. The Thevenin equivalent model is used to represent the battery in this thesis, as shown in Fig 5.11. This model consists of a voltage source, V_{bat}, and resistance, R_{in}. These are known as the nominal cell voltage or open circuit voltage and the internal resistance of the cell. Even though this is the simplest cell model that can be used, the values of the components are complex. Both these values are dependent on factors such as cell temperature and especially the SOC of the cell. It has been decided, for simplicity, to keep the values of the open circuit voltage and the internal resistance constant. The simulation durations are short in comparison to one discharge cycle of the cell and battery pack. Thus, the values of V_{bat} and R_{in} will in actual fact appear to be constant during this time.

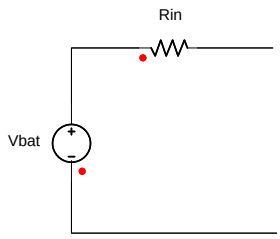

Fig 5.11: Thevenin battery model used in simulation.

It can be seen from Fig 5.12 that the cell terminal voltage and thus the converter bus voltage is dependant on the battery current. The cell terminal voltage can be calculated as follows:

$$V_{bus} = V_{bat} + R_{in} I_{bat} \tag{5.15}$$

5.6. Controller design

To illustrate the need for closed loop control of the converter circuit an investigation can be made into the open loop response of the system. A few predictions about the open loop response can be made by observing the transfer function of the system given by equation 5.11. It can be seen, from the transfer function, that the system contains a zero at the origin. This zero acts as a differentiator that causes extremely high overshoot in the open loop response of the system. The exact value of the overshoot can be obtained by implementing the system model in a software package.

Throughout the chapter simulations are performed using two software packages. The first package that is used MatLab/Simulink. This package allows for block diagram simulation of the system. It also has the necessary mathematical tools required for the design of the controllers. The second package used is Simplorer. This package was designed to be able to simulate circuits that use power electronic

switches. The results obtained from Simplorer shows the switching effects, which are not seen in the MatLab/Simulink results.

Fig 5.13 shows the open loop response of the system. The capacitor voltage is equal to zero. The figure shows the extremely high overshoot in the ultra capacitor current, estimated at 2050 A. The following parameters were used:

L : 350 μH

R_{esr} : 28 mΩ

C_{uc} : 33.5 F

There is good correlation between the MatLab/Simulink results, Fig 5.13a, and the Simplorer results, Fig 5.13b. This confirms the accuracy of the transfer function derived in Section 5.5. Fig 5.14 shows the ripple that is found on the capacitor current due to the switching effect.

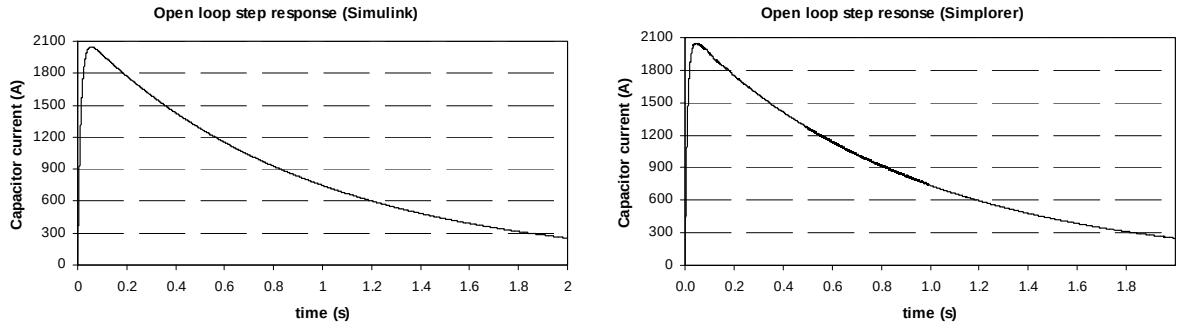

Fig 5.13: Open loop response of system using (a) MatLab/Simulink and (b) Simplorer.

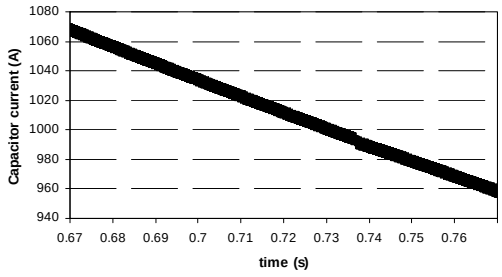

Fig 5.14: Capacitor current ripple

5.6.1 Ultra capacitor current controller

It can be seen from Fig 5.12 that closed loop control of the ultra capacitor current is crucial. The best control method is through the use of a PI controller. Fig 5.15 highlights this part from Fig 5.9. A PI controller was chosen so that cancellation between the plant differentiator and the controller integrator takes place. The MatLab software has the required tools for designing the required PI controller. MatLab's root locus tool is used. The system transfer function is imported into the root locus tool. Equation 5.11 is used as the system transfer function.

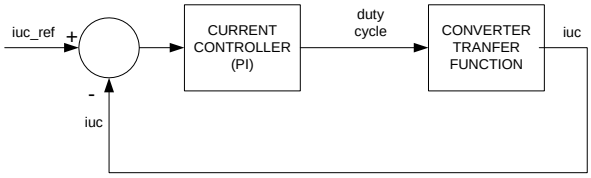

Fig 5.15: Block diagram of ultra capacitor controller with converter

The controller was designed so that the system would have a step response that has a rise time of τ = 100 ms. It is important that no overshoot occurs in the closed loop current response of the system. This is due to the fact that the overshoot in the capacitor current can be of such a magnitude as to cause damage to the capacitors and especially the other components in the EMS circuit. The transfer function of the designed PI controller is as follows:

$$C_{uc}(s) = 0.05\left(0.033 + \frac{1}{s}\right) \tag{5.16}$$

Fig 5.16 shows the closed loop step response of the system for a unit step input. The required closed loop response is obtained with the designed PI controller.

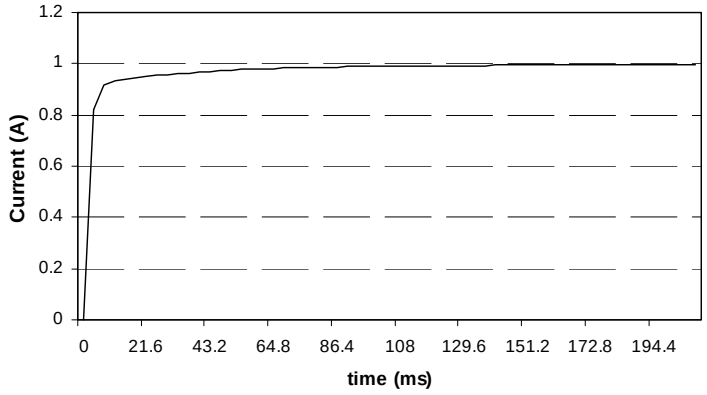

Fig 5.16: Closed loop step response of system.

The controller designed so far does not take into account the fact that the ultra capacitors have a voltage limit. A mechanism must be built into the control system to reduce the capacitor current to zero when the ultra capacitor voltage limit, V_{uc_lim}, is reached. It can be seen from equation 5.11 that the capacitor current will be equal to zero if the converter duty cycle is equal to the ratio between the ultra capacitor voltage and the bus voltage. Thus, a limiting function is placed at the output of the PI controller. The duty cycle, d_{lim}, which ensures that the maximum ultra capacitor voltage is not exceeded, is given as:

$$d_{\lim it} = \frac{V_{uc\_\lim}}{V_{bus}} \tag{5.18}$$

A problem that occurs when a limiting function is placed in a PI control loop is the so called integrator wind-up. This occurs when the output of the PI controller surpasses the limit. The integrator of the PI controller keeps integrating the error causing an ever increasing output of the PI controller. At a certain stage, the actual value is able to meet the reference signal. Although the error signal becomes zero, the output of the PI controller still has a high value and must integrate 'down'. This adds unwanted delay to the response of the system. The solution to the problem is to switch off the integrator once the limit of the limiting function is reached, changing the PI controller into a proportional controller. No delay occurs and the integrator is switched back on if no limiting is done.

It is important to notice the difference in the response of the system due to the limiting of the converter duty cycle. Fig 5.17 shows the response of the system with and without the implementation of the limiting function. It can be seen from Fig 5.17a that the capacitor current starts to fall away once duty cycle limit is reached, at t = 2.5 seconds. Fig 5.17b shows that the voltage limit of the capacitor has not been reached. At this point in time there is still a voltage drop across the inductor and series resistance. The capacitor current starts decreasing exponentially until the capacitor voltage limit is reached, at which the capacitor current is zero. The ultra capacitor voltage limit was set at 80 V. The starting capacitor voltage was set at 40 V. This was done to shorten the simulation time as the voltage limit is reached sooner with a high capacitor start voltage. A reference current of 400 A was given. The results show that the system reaches the reference current within the required time. Fig 5.15b shows that the limiting function does not allow the capacitor voltage limit to be crossed. There is an agreement between the results obtained from MatLab/Simulink and Simplorer.

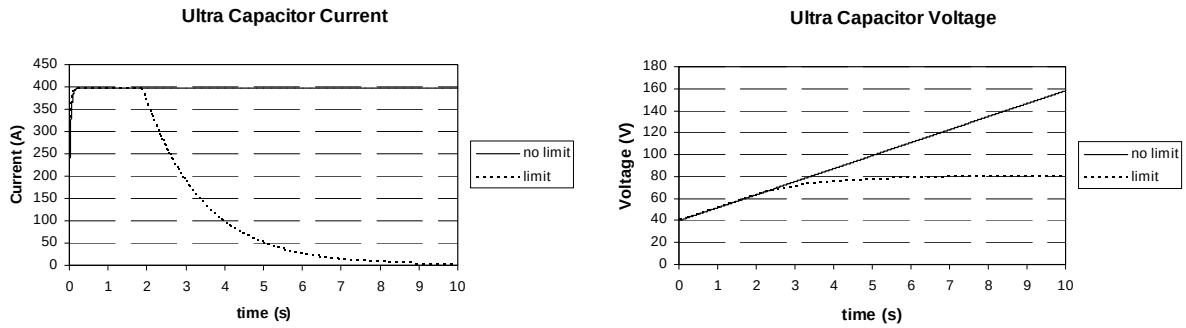

Fig 5.17: Simulated capacitor (a) current and (b) voltage for with and without limiting function.

5.6.2 Battery current controller

The next step in the development of a control algorithm for the energy management system is the design of the battery current controller. Fig 5.18 highlights the parts of Fig 5.9 that are discussed in this section. The ultra capacitor current reference is ultimately determined from the measured load current.

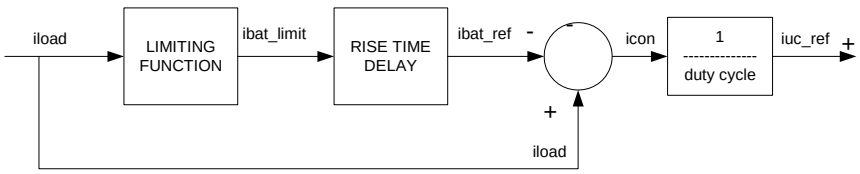

Fig 5.18: Block diagram of functions used to determine the ultra capacitor current reference.

The system that determines the ultra capacitor current is divided into three parts. The first part determines if the load current is within specified battery current limits. The second part adds a delay in the rise time of the battery current. The output of this block is a battery current reference. The last part uses this battery current reference to calculate the ultra capacitor current reference by using the node equation 5.12. The equation for the ultra capacitor current reference is given as:

$$I_{uc}^{*} = \frac{I_{load}(s) - I_{bat}^{*}(s)}{d(s)} \qquad (5.16)$$

A. Limiting function

It is the function of the energy management system to keep the battery current within the operational ranges of the battery pack and thus limit the amount of power flowing in and out of the battery pack. This is achieved by the first block seen in Fig 5.9, i.e. the limiting function. The measured load current is checked to verify whether it is within the specified limits. A battery current reference is determined accordingly. The load current check is as follows:

$$\text{if} \quad I_{load} \le I_{neg\_limit} \quad \text{then} \quad I^*_{bat} = I_{neg\_limit}$$

$$\text{if} \quad I_{load} \ge I_{pos\_limit} \quad \text{then} \quad I^*_{bat} = I_{pos\_limit}$$

$$\text{if} \quad I_{neg\_limit} \le I_{load} \le I_{pos\_limit} \quad \text{then} \quad I^*_{bat} = I_{load}$$

Fig 5.19 shows the MatLab/Simulink implementation of the load current checker.

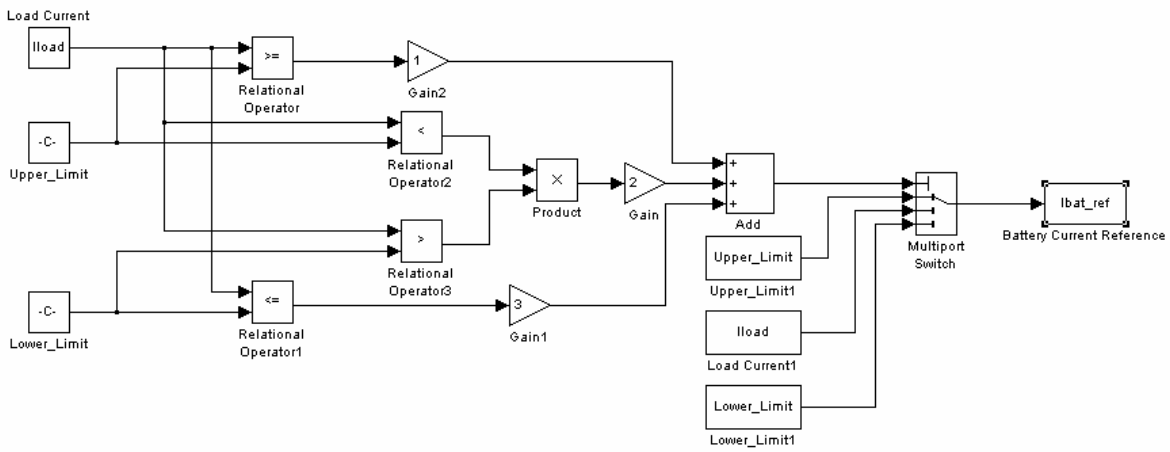

Fig 5.19: Load current checker.

The operation of the limiting ability of the energy management system is shown through simulation results. A step input was used for the load current. This is a condition of the load current that can occur during fast acceleration and regenerative braking. An ideal step function could not be used in the simulation due to the fact that the software package is not always able to solve the system for such an input. Rather a quasi-step input was used. This is a function containing a very steep leading slope. This function resembles the actual load current as ideal steps do not occur in the real vehicle system. Some of the results are shown in Fig 5.20 and 5.21. Simulations were done for a positive and negative load current. It must be remembered that these results are of the system without the rise time delay function seen in Fig 5.9. Only current limiting is preformed.

The system parameters are the same as in the previous sections. An ultra capacitor initial voltage, V_{uc0}, equal to 10 V was chosen during positive load current and 60 V during negative load current. The limiting values used are as follows:

I_{pos_limit} = 30A

I_{neg_limit} = -30A

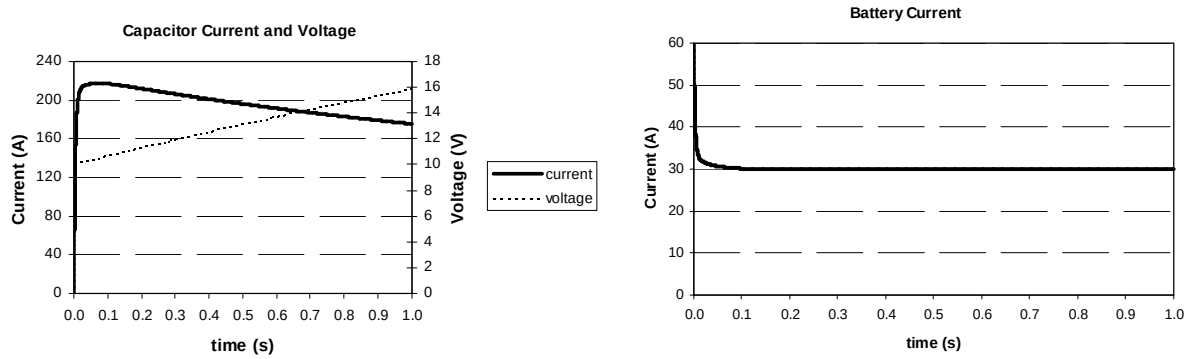

Fig 5.20: Simulated (a) capacitor current and voltage and (b) battery current (60 A).

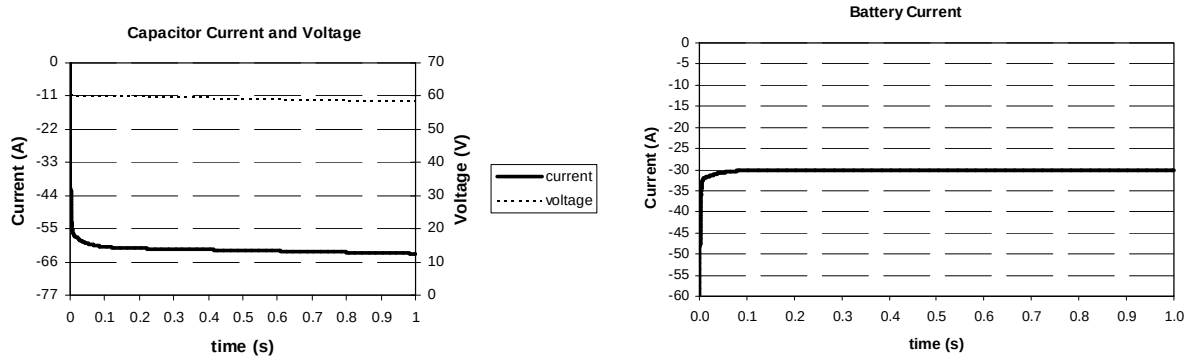

Fig 5.21: Simulated (a) capacitor current and voltage and (b) battery current (-60 A).

For the results shown in Fig 5.20 and 5.21, a step load current of 60 A and -60 A respectively at t = 0 seconds were used. At that moment the battery current jumps from 0 to 60 A and -60 A depending on if the load current is positive or negative. This is due to the reaction time of the ultra capacitor current controller. The system cannot respond fast enough to the rising edge of the load current. This is in actual fact a lot faster than the rising edge in the load current in an actual vehicle system. It can be seen that the battery current reaches the limit of 30 A and -30 A at approximately t = 100 ms.

The reaction of the system to a sinusoidal load current was also simulated. Fig 5.22 shows the response of the system to such a sinusoidal load current. The load current had amplitude of 60A and a frequency of 1 rad/s.

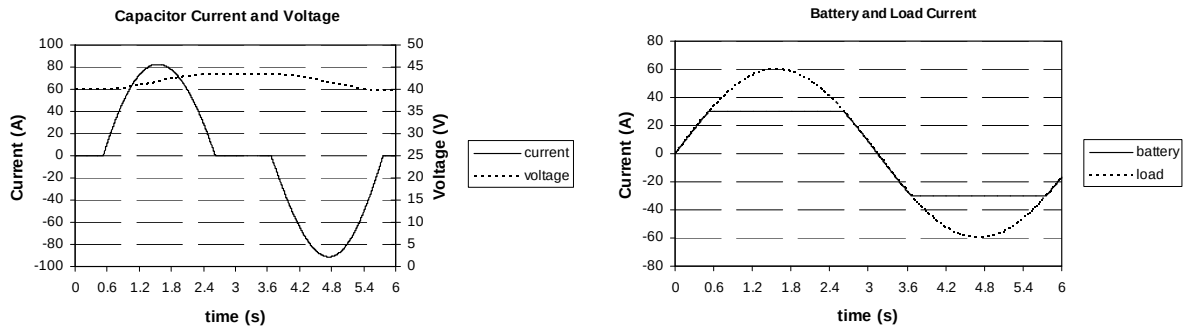

Fig 5.22: Limiting response with sinusoidal load current.

B. Battery current rise time delay

A lithium cell is not only damaged by excessive current, but also by quick changes in the battery current as well. It is the function of the EMS to control the rise time of the battery current. This is achieved by adding a simple filter function after the load current checker, as seen in Fig 5.9 and 5.18. The filter function has the added benefit of removing high frequency content from the battery current. A first order filter function was chosen. The equation of the filter function is given as:

$$H(s) = \frac{a}{s+b} \tag{5.18}$$

A rise time in battery current of roughly 1 second was chosen for when a unit step is applied as input. This requires that the filter function have a pole at s = -5, thus b = 5. Furthermore, it is required that the function has unity DC gain. If the final value theorem is applied to the function, a must be equal to b to obtain a unity DC gain. Fig 5.23 shows the response of the filter function to a unit step. A rise time of 1 second is obtained.

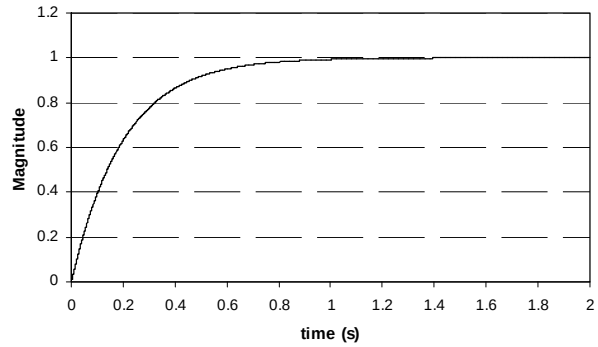

Fig 5.23: Step response of filter function.

Fig 5.24, 5.25 and 5.26 shows the simulation results when the filter function is added to the system. The same load current is introduced at t = 0 seconds, i.e. 60 A and -60 A step, as in the limiting function simulations. The results show that the energy management system controls the rise time of the battery current to 1s.

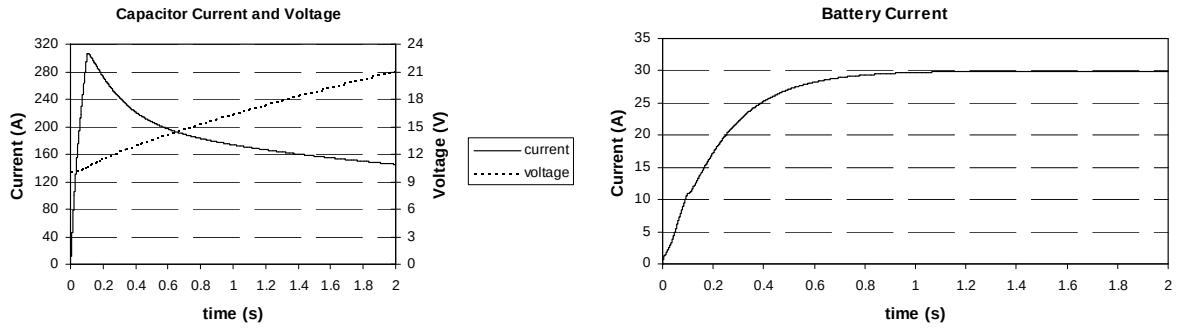

Fig 5.24: Simulated (a) capacitor current and voltage and (b) battery current (60 A).

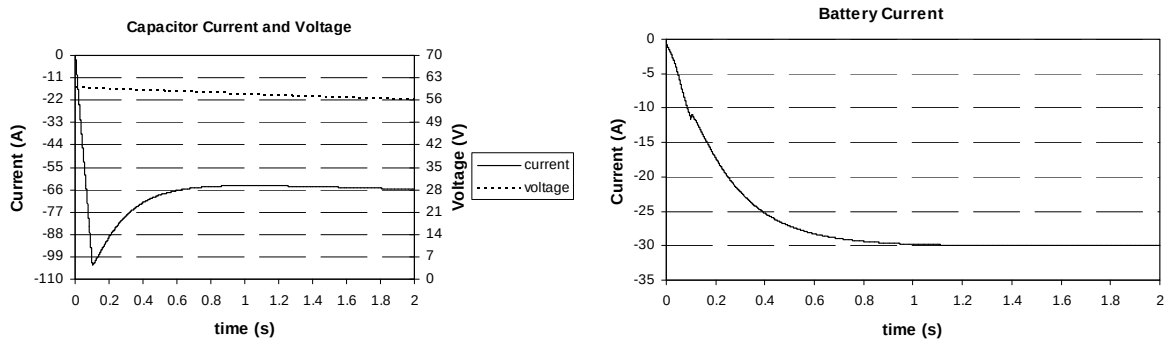

Fig 5.25: Simulated (a) capacitor current and voltage and (b) battery current (-60 A).

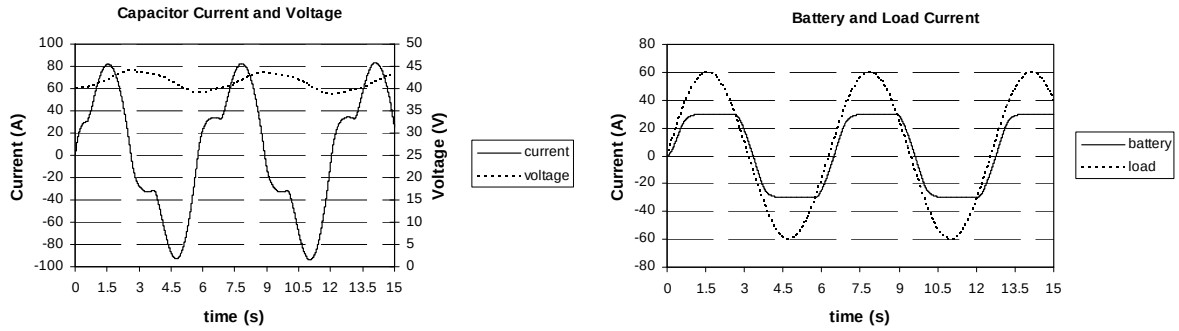

Fig 5.26: System response with sinusoidal load current

The previous simulation results show the response of the system over a short period. Simulations were also done over a full charging cycle of the ultra capacitors, shown in Fig 5.27 and 5.28. A load current of 200 A was chosen for the simulation. The load current is equal to 200 A, in the actual system, when the electric drive returns full power to the EV's energy system during regenerative braking. Fig 5.27 shows the ultra capacitor current and voltage for the system without and with the filter function. It can be seen that the capacitor current has a higher peak when the filter function is implemented than without. This is of course due to the larger amount of current needed to be diverted to the capacitors to allow for the rise time in the battery current. Fig 5.28 shows the battery current as a function of time, again for both cases. It is found that the addition of the shaping function shortens the time taken for the capacitor to reach its limit by approximately 250 ms.

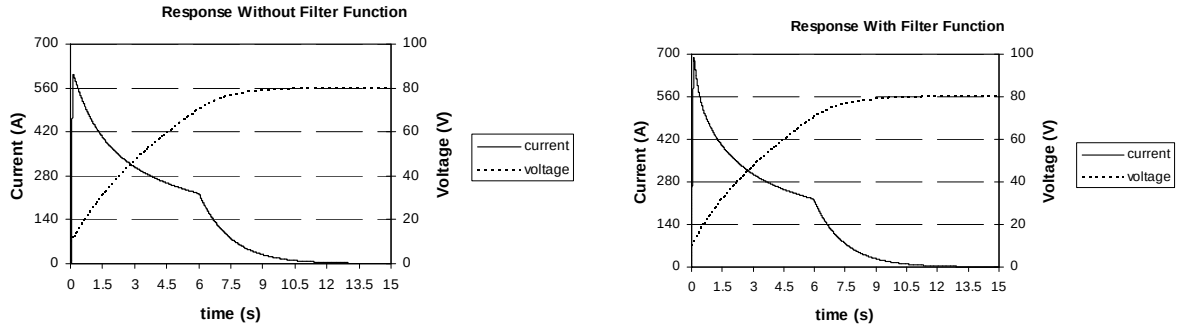

Fig 5.27: Ultra capacitor current and voltage with positive load current (200 A)

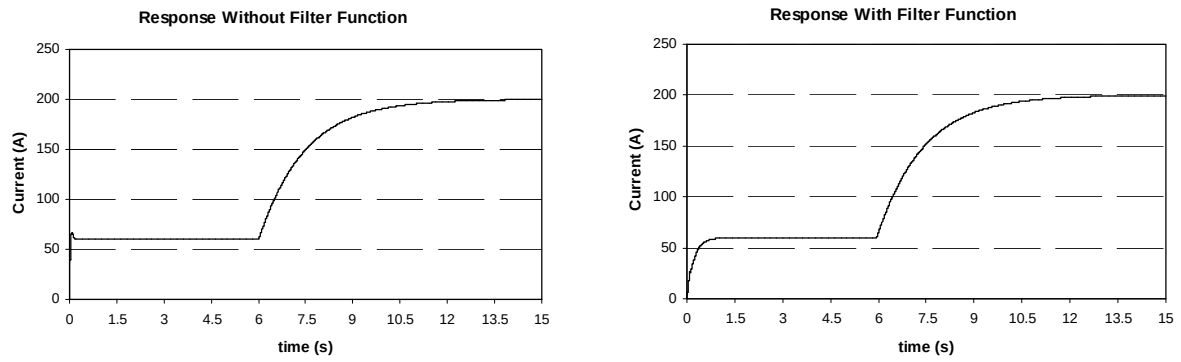

Fig 5.28: Battery current with positive load current (200 A)

5.7 EMS laboratory testing

In the previous section, the control algorithm for the energy management system was derived. The operation of the system was verified through simulation. It is important that these be verified by practical measurements. This section firstly presents the practical setup used to perform these practical measurements. Fig 5.29 shows a diagram of this setup. A few of the components used in the setup are discussed. The section presents some of the practical results used to verify the operation of the energy management system.

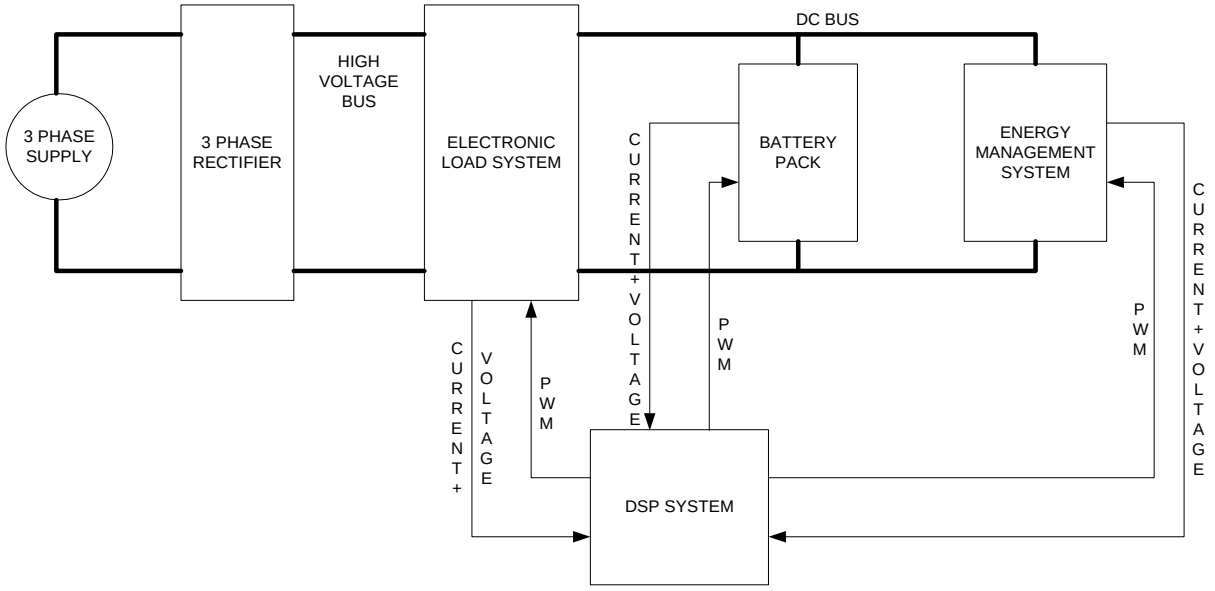

Fig 5.29: Block diagram of EMS laboratory test setup

5.7.1 Setup components

The DSP system seen in Fig 5.27 plays a crucial role in the practical measurements. The DSP system is where the control algorithm is implemented. The system is equipped with a number of analogue inputs, each connected to an ADC. These are used to read the current and voltage measurements from the measurement circuits. The DSP system is also equipped with a number of optical outputs. These outputs are used to deliver the PWM signals to all the converters in the practical setup. The system also has several buttons and analogue outputs. These are used during the debugging process of the control program. The signals from the analogue outputs can be displayed by means of an oscilloscope. Any of the control program variables can be displayed in this way.

As mentioned before, the current and voltage measurements are read from measurement circuits. These circuits have been designed specifically for the DSP system. The voltage measurement circuit is a simple differential probe with measurement ratio determined by two resistances with values equal to 4.7 kΩ and 2.16 MΩ respectively. As these resistances have tolerances, calibration of the measurement circuits is preformed in the control program. The current is measured using a LEM current transducer [45].

The current measurement circuit measures the secondary current from the transducer. The LEM module used has a winding ratio of 1:2000. The current measurement circuit consists of a resistance and a unity gain op-amp. The circuit thus converts the output current from the transducer to a voltage. The value of the resistance must be chosen so that the voltage across it is within the range -2.5 V < $V_{measured}$ < 2.5 V. This ensures that the voltage is within the limits of the ADC's, which is 0 V < V_{ADC} < 5V. The circuit must be able to measure positive and negative current, but the ADC can only sample positive voltage. The voltage across the measurement resistance is given a 2.5 V offset so that negative current can be measured. It must be remembered that this offset must be removed from the measurement in the control program. The measuring resistance, $R_{measure}$, is dependent on the maximum current measured, I_{max}, the winding ratio of the transducer, wr, and the voltage limit of the ADC's, $V_{max,}$ The required resistance is calculated as follows:

$$R_{measure} = \frac{V_{\max} wr}{I_{\max}} = \frac{2.5 * 2000}{330} = 15.15\Omega \qquad (5.19)$$

A resistance value of 15 Ω was chosen. The maximum measured current was taken as 330 A. As shown in the simulation results, the capacitor current can exceed 1000 A. It was decided to perform downscaled testing of the energy management system. The maximum current was near 300 A during the tests.

The control program implementing the control algorithm of the energy management system was structured having a main routine and three interrupt procedures. The main routine contains initialization code followed by an endless loop. The initialization code sets up the ADC's as well as the DSP internal timer. The timer is used to generate an interrupt at a fixed frequency. The period of the timer is chosen as 100 μs, the same frequency as the switching of the converter. One of the interrupt procedures are executed, depending on the state scheduled. The three states are the "Wait", "Run" and "Error" states. During the Wait state the measurements from the measurement circuits are calibrated after which the program waits for a start signal from the user. No PWM outputs are enabled during this state. Once the start signal is received, the program goes over to the Run state. It is during this state that the operation of the system occurs. Thus, the control algorithm is executed into the Run state procedure. An error state is also implemented. The control program goes in the Error state if certain conditions occur. These are specified by the programmer. It is advisable that no PWM signals are given during this state. The FPGA used in the system has it own Error state. The hardware in the FPGA performs an error check each interrupt cycle. These include over current and voltage as well as PWM integrity. The PWM "watch dog" ensures that the PWM signals receive a value from the control program each cycle. Fig 5.27 is a flow diagram of the control program.

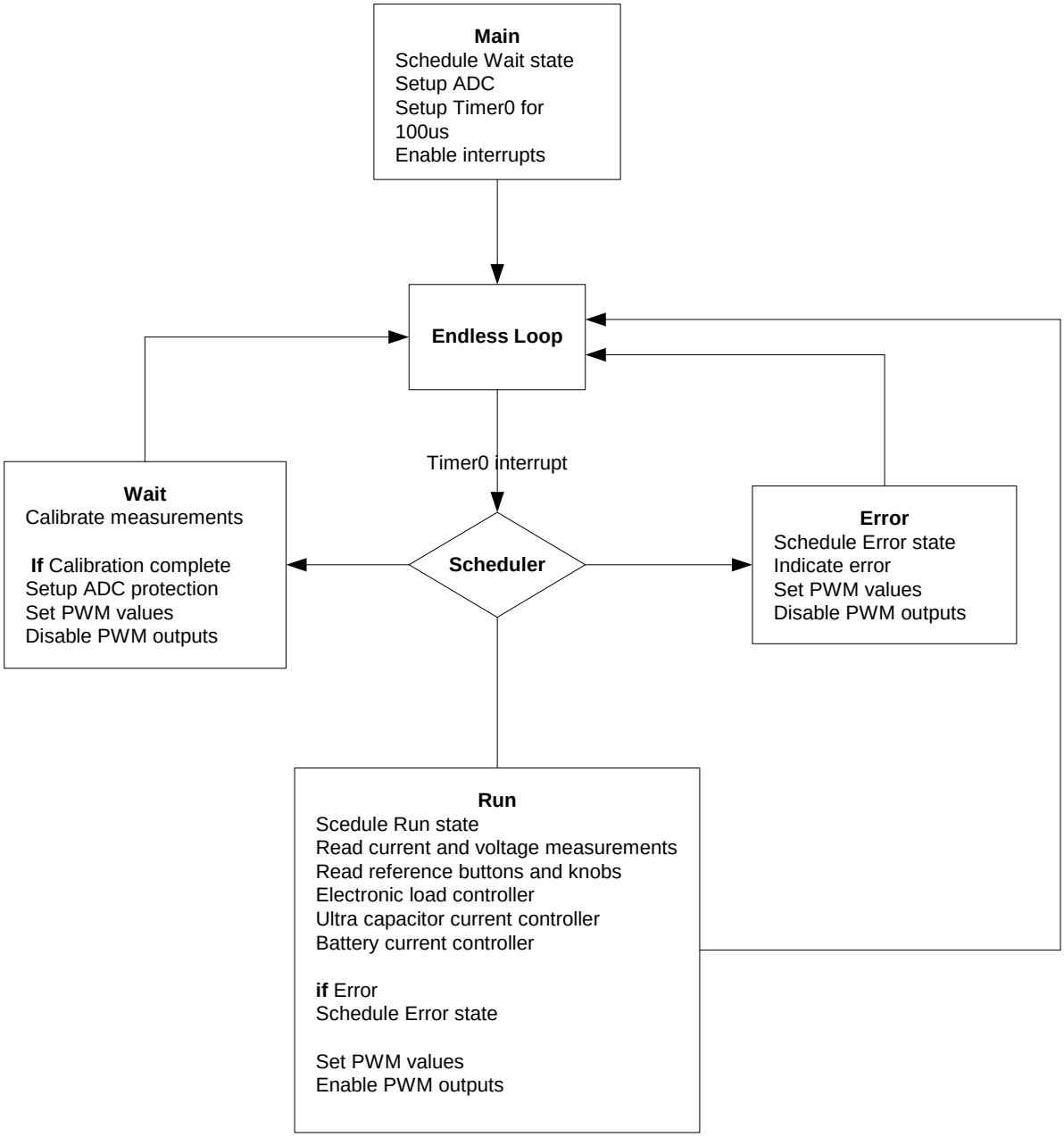

Fig 5.30: Control program flow chart.

5.7.2 Other considerations

As mentioned, the EMS that is studied will ultimately be implemented in an EV system. The specifications of this energy system are such that the system can be seen as a low voltage, high current system. The bus voltage was chosen as 120 V as seen in section 4.4. This is in contrast to the high voltage, low current systems used in other research [6] [45]. These systems have a bus voltage as high as 300 V. It is one of the aims of the study to determine if it is possible to have an effective EMS in a low voltage, high current energy system. It is estimated that the ultra capacitor current will be high in such an energy system. Specific IGBT modules were chosen that had a current rating of 1200 A, to ensure that the power electronic converters would not be damaged during the testing of the EMS. These modules have been packaged at the University of Stellenbosch into a single phase arm circuit for experimental purposes. These circuits include the IGBT driver circuits with optical PWM inputs, bus capacitors and snubber capacitors. A photo of such a circuit is shown in Appendix E.

Fig 5.6 shows that the converter also contains a smoothing inductor. Ideally, the ultra capacitor current should be smooth. It is, however, not possible due to the switching of the converter. It is the function of the inductor to minimize the capacitor current ripple. The maximum allowable capacitor current ripple is an important design variable. High current ripple can lead to excessive EMI or even unwanted mechanical vibration. The equation for the maximum current ripple is given by

$$i_{uc\_\max\_ripple} = \frac{V_{bus}}{4 f_s L} \tag{5.8}$$

where V_{bus} is the converter bus voltage, f_S is the switching frequency of the converter and L the inductance of the smoothing inductors. A max current ripple of 10 A is chosen. This is very small in comparison with the maximum capacitor current. After a bus voltage of 120 V and a converter switching frequency of 10 kHz were considered, the needed inductance is calculated as 300 μH. This is considerably smaller than that in other systems [34]. Although the inductor is small in inductance, it is possible that it is still a physically large component. It must be able to carry the high capacitor current. This means that a) large conductors are needed to be able to carry the high currents; b) an expensive inductor core or a coreless inductor is required to prevent core saturation. The design of a converter inductor must not be underestimated, especially in a low voltage, high current system.

It must be remembered that the inductor and the ultra capacitors have an equivalent series resistance (ESR). This resistance must be taken into account when deriving a model for the converter and was added to the circuit diagram as shown in Fig 5.8.

5.7.3 Electronic load system

The load that is connected to the energy system when implemented in an EV is the electric drive system. The electric drive system consists of an inverter and electric motor. The number used depends on the drive train of the vehicle. This electric drive system acts as a bi-directional load. It draws power from the energy system when in motoring mode and delivers power back to the energy system when in braking or generator mode. Thus, a more realistic load to use in laboratory testing of the energy management system operation is an electric drive system. However, this is very cumbersome to setup. The electric drive must have its own load system as well as control system, making this a very impractical setup. An alternative option is to use a bi-directional electronic load to test the energy management system, as shown in Fig 5.29. This is a simply controlled power electronic converter.

The same circuit and control design techniques used to design the converter in the energy management system are used to design the electronic load. This particular circuit will also allow different load current waveforms to be generated, such as dc and sinusoidal currents. Fig 5.31 shows the circuit used for the electronic load. The high side bus voltage, V_d, is chosen a few times higher than the battery voltage. As mentioned before, the vehicle system that the electronic load has to simulate is a low voltage, high current system. Thus, the electronic load needs to deliver a high current, in the order of 200 A. A relatively small input current is needed due to the low duty cycle of the converter. The high side voltage is obtained from a three phase rectifier, as shown in Fig 5.31.

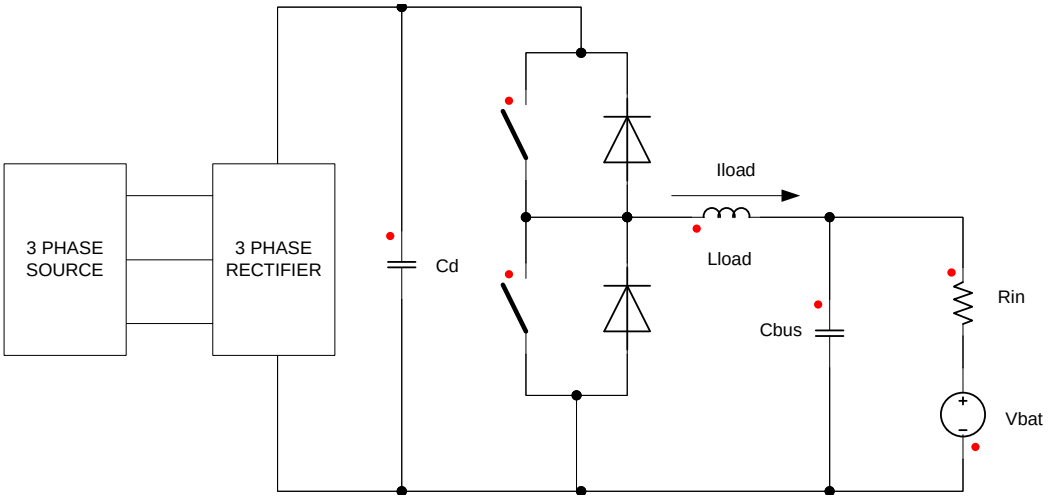

Fig 5.31: Circuit diagram of electronic load system and battery pack.

Fig 5.32 shows the block diagram of the electronic load system. As with the control of the ultra capacitor current in section 5.6.1, a single control loop is used to control the load current.

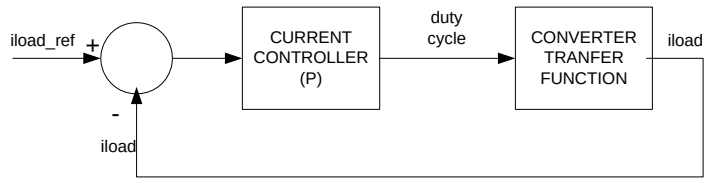

Fig 5.32: Block diagram of electronic load system.

The transfer function of the system in Fig 5.31 is required to design the control algorithm for the electronic load system. The same method used to derive the transfer function for the converter in the energy management system is used to derive the electric load transfer function i.e. the Middlebrook and Cuk method. The electronic load system has two inputs, V_d and V_{bat}. The super positioning principle is used to obtain the function of the load current for each of the inputs. The functions for the load current are given as:

$$I_{load} = d(s)V_d \frac{\frac{1}{L_{load}}s + \frac{1}{L_{load}R_{in}C_{bus}}}{s^2 + \frac{1}{R_{in}C_{bus}}s + \frac{1}{L_{load}C_{bus}}} \tag{5.20}$$

when the input voltage V_{bat} is set equal to zero.

$$I_{load} = -V_{bat} \frac{\frac{1}{L_{load}R_{in}C_{bus}}}{s^2 + \frac{1}{R_{in}C_{bus}}s + \frac{1}{L_{load}C_{bus}}} \tag{5.21}$$

when the input voltage V_d is set equal to zero.

By applying the super positioning principle, the function for the load current is given as:

$$I_{load}(s) = d(s)V_d \frac{\frac{1}{L_{load}}s + \frac{1}{L_{load}R_{in}C_{bus}}}{s^2 + \frac{1}{R_{in}C_{bus}}s + \frac{1}{L_{load}C_{bus}}} - V_{bat} \frac{\frac{1}{L_{load}R_{in}C_{bus}}}{s^2 + \frac{1}{R_{in}C_{bus}}s + \frac{1}{L_{load}C_{bus}}} \tag{5.22}$$

As can be seen from Equation 5.22, it is extremely difficult to obtain a transfer function that is the product of a voltage difference and a dynamic term, as was the case for the converter used in the EMS. It was found that a certain assumption could be made to obtain such a function. The following assumption was made:

$$I_{load} = \left(d(s)V_d - V_{bat}\right)\frac{\frac{1}{L_{load}}s + \frac{1}{L_{load}R_{in}C_{bus}}}{s^2 + \frac{1}{R_{in}C_{bus}}s + \frac{1}{L_{load}C_{bus}}} \tag{5.23}$$

This assumption was verified by investigating the response of equations 5.22 and 5.23 to a unit step duty cycle input, *d(s)*. The parameters used are: L_{load} = 1.1 mH; C_{bus} = 13.2 mF; R_{in} = 40 mΩ; V_{bat} = 20 V. Fig 5.33 shows the step responses of the two equations. It can be seen that the two are virtually identical. Thus, the function for the load current can be expressed by Equation 5.23.

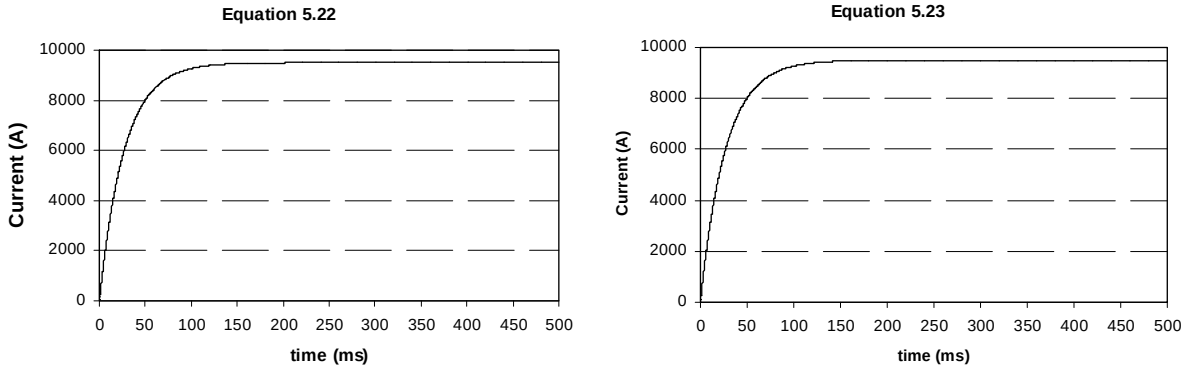

Fig 5.33: Response of (a) equation 5.22 and (b) equation 5.23 to unit step.

Equation 5.23 is imported into MatLab's root locus tool. The root locus tool is used to design the controller for the load current. As shown in Fig 5.32, a proportional controller is designed to obtain the required load system response. Fig 5.34 shows the block diagram of the control system as implemented in MatLab/Simulink. It was found that a proportional gain of 10 gives the required response.

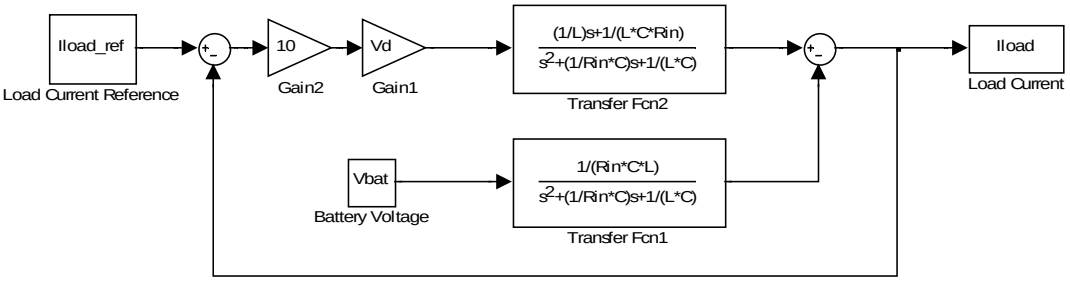

Fig 5.34: MatLab/Simulink block diagram of electronic load system.

The load system is simulated in Simplorer to see the effect that the switching has on the response of the system. Fig 5.35a shows the current delivered by the load, approximately 200 A. This current contains a high current ripple. On the other hand, Fig 5.35b shows the battery current. It can be seen that the current is smoothed by the bus capacitors. Although slightly higher than the required current, the current obtained by the load system is acceptable.

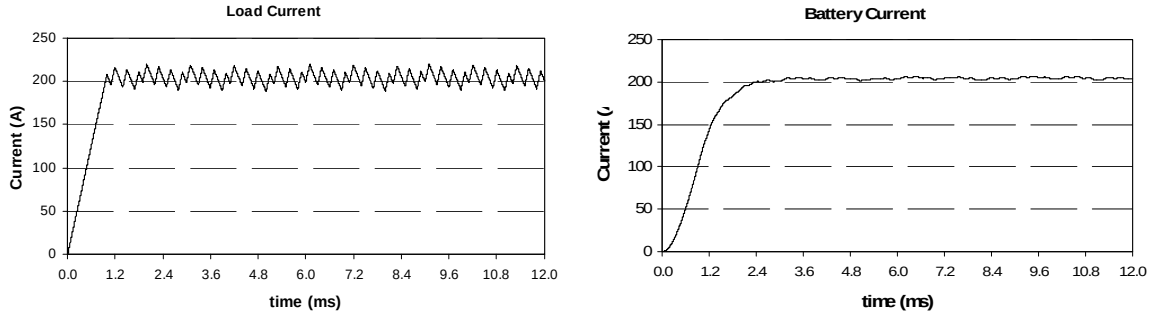

Fig 5.35: Simplorer results of a) load current and b) battery current.

The DC voltage, V_d, and current on the high voltage side of the load system is obtained from a three phase rectifier. The rectifier blocks the negative load current. A dumping circuit was added to the load system to deal with the negative load current. Fig 5.36 shows this circuit. The dumping circuit consists of a converter and a resistor. No other components were used to keep the control of the dumping circuit simple. The duty cycle of the converter is chosen to be proportional to the capacitor over voltage. The converter is thus not switched if the capacitor voltage is below the specified limit. A function was also added that halts the operation of the system if the capacitor voltage becomes too high.

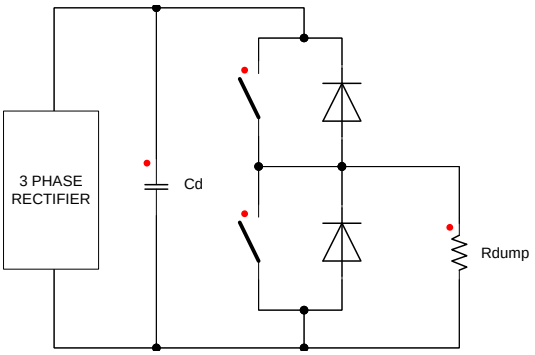

Fig 5.36: Load dumping circuit

The operation of the electronic load system was verified through measurements. Fig 5.37 shows the response of the system measured for both positive and negative current, being 20 A and -20 A respectively. It can be seen that the load current follows the current reference. A rise time in the load current, of approximately 150 ms is obtained. The electronic load system was also used to generate a sinusoidal load current, as shown in Fig 5.38.

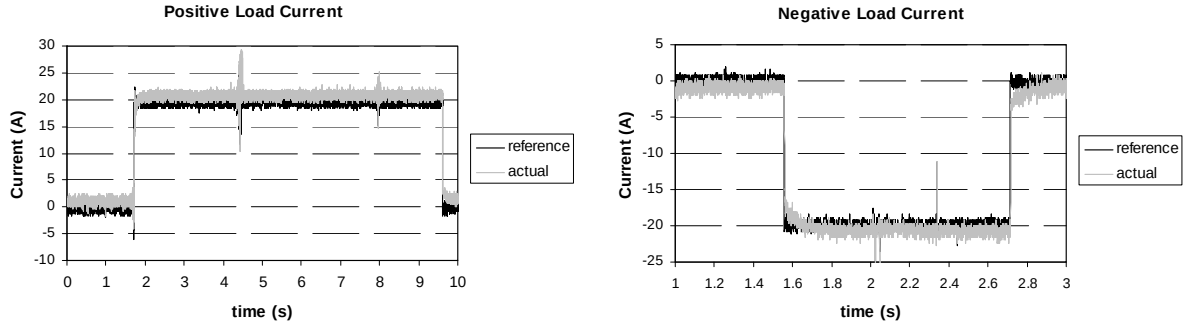

Fig 5.37: Practical results of electronic load for positive and negative load current.

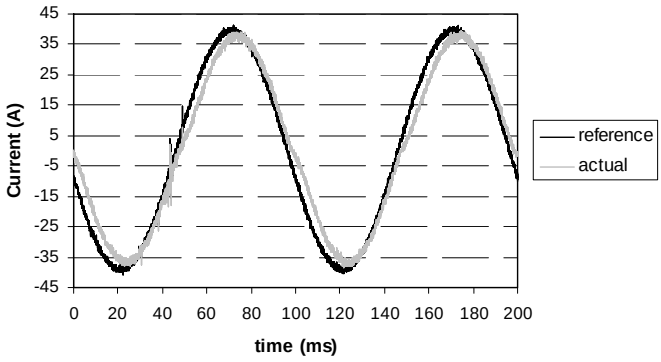

Fig 5.38: Sinusoidal load current.

5.7.4 Practical measurements

In this section a few of the laboratory measurements of the operation of the EMS are given. The system was however not tested to its full capability. Full testing of the EMS requires a load current of 200 A. The testing was downscaled mainly due to limited current capability of the three phase source and rectifier. The rectifier current was measured in excess of 30 A during testing with a load current of 60 A. Although not at full capability, the tests provide valuable results to verify the operation principle of the EMS.

It must be mentioned that the measurements presented contain large amounts of noise. The main contributor to this noise is the switching of the power electronic converters. Furthermore, coreless inductors were used to ensure that inductor core saturation does not take place. These also generate EMI. A photo of these coreless inductors can be found in Appendix E.

A. Capacitor current control

The first step to take is the testing of the ultra capacitor current loop, as designed in section 5.6.1. Fig 5.39 shows the measured results with a 40 A and -40 A ultra capacitor current command respectively. Fig 5.40 shows the capacitor current rise time to be 120 milliseconds. These results compare well with the results obtained from simulation in section 5.6.1, Fig 5.16.

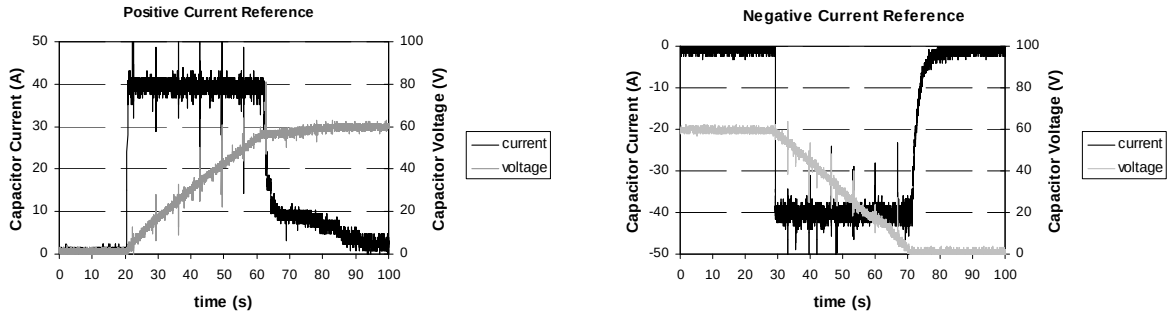

Fig 5.39: Ultra capacitor current and voltage for positive and negative current commands.

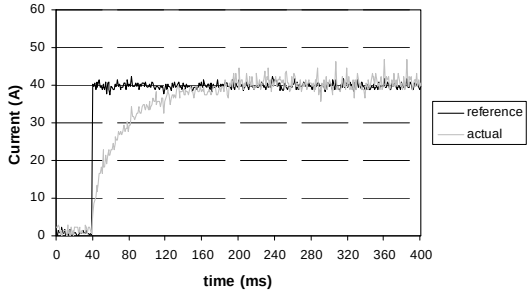

Fig 5.40: Ultra capacitor current rising edge.

B. Limiting Function

The next set of measurements show the battery current limiting operation of the EMS, as designed and simulated in section 5.6.2 A. A step load current could not be used during this test as this could possibly damage the expensive battery cells. The load current was be increased or decreased by a reference knob on the DSP system to ensure that the current rise time did not damage the cells. A maximum load current of 60 A (braking mode) and -60 A (motoring mode) was chosen. This ensured that the rectifier current stayed within its limits. The battery current limit was set the same as in the simulations i.e. 30A and -30A. Fig 5.41 shows the battery current for both positive and negative load current. The noise mentioned can be seen in the measurements.

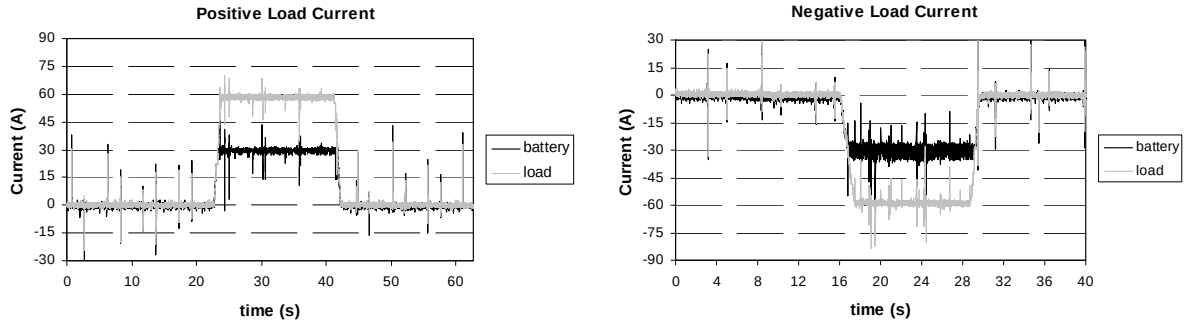

Fig 5.41: Battery and Load current during positive (braking) and negative (motoring) load current.

Fig 5.42 shows the ultra capacitor current and voltage during the limiting operation of the energy management system. These results were measured over one charge or discharge cycle of the capacitors. These results are in agreement with the results obtained from the simulation results shown in section 5.6.2 A.

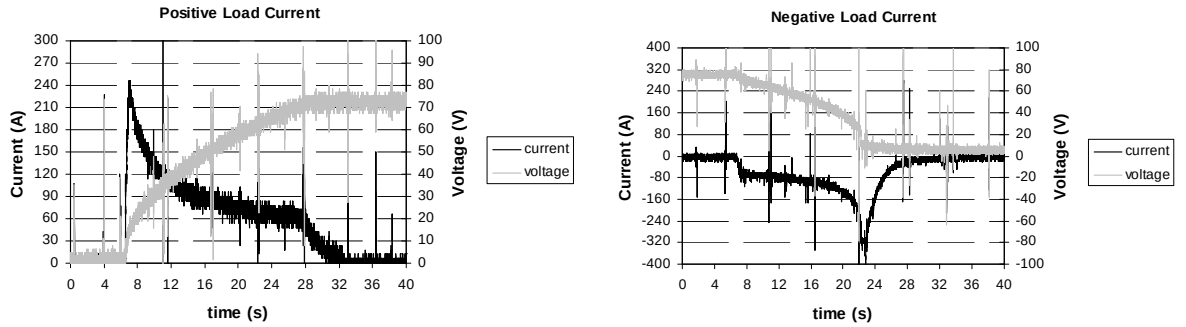

Fig 5.42: Capacitor current and voltage for positive (braking) and negative (motoring) load current.

C. EMS testing

The next results show the operation of the EMS with the addition of the filter function to determine the rise time of the battery current. Fig 5.43 shows the battery current for both positive (braking) and negative (motoring) load current. The results show a battery current rise time of 1 second, as was designed in section 5.6.2 B. The results compare extremely well with the simulation results and the operation of the EMS is better than expected.

Fig 5.43b shows that the battery current contains a higher amount of current ripple for negative load current than for positive load current. The extra noise is mainly added by the electronic load dumping circuit that only operates during negative load current.

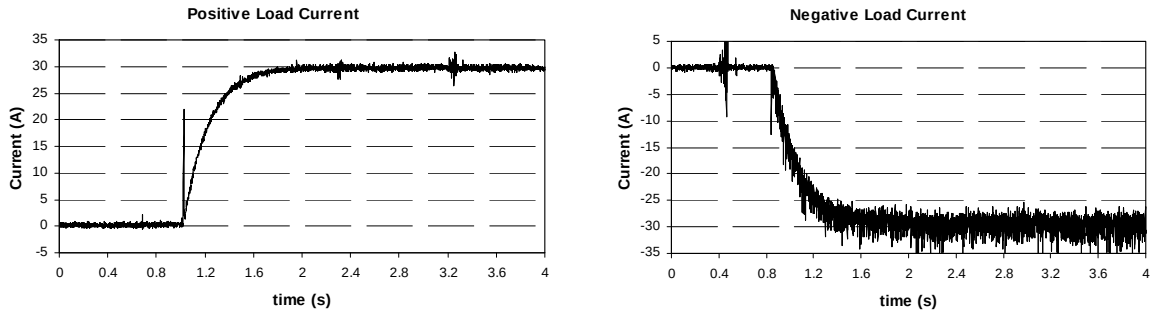

Fig 5.43: Battery current for positive (braking) and negative (motoring) load current.

Fig 5.41 shows the ultra capacitor current for both positive and negative load currents. These results compare well with the simulation results. The peak capacitor currents witnessed in the practical measurements are close to those seen in the simulation results of Fig 5.24a and 5.25a.

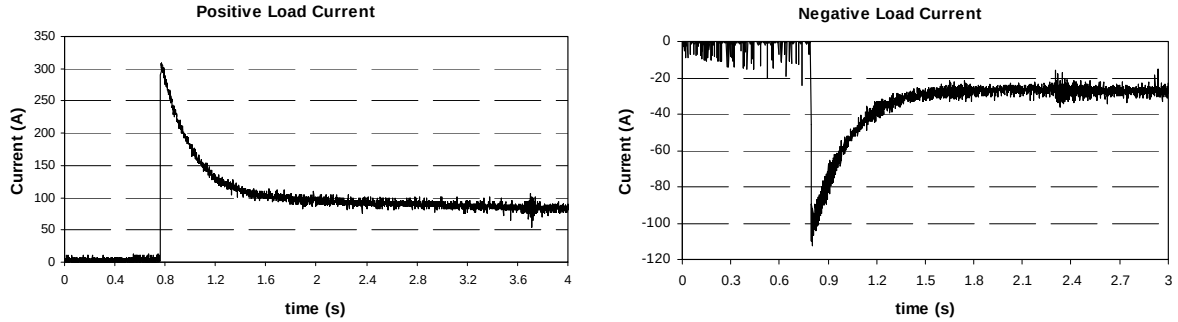

Fig 5.44: Ultra capacitor current for positive and negative load currents.

As mentioned in section 5.2, two separate ultra capacitor units were used during the practical measurements. The voltage across each unit was monitored during all practical measurements. It was found that the one unit charged more quickly than the other. This resulted in the one unit having a higher voltage than the other. Charge was not equal between the two units. This is a major concern when using multiple ultra capacitor units in series. This difference in charge can lead to under utilization of the operation voltage range of the capacitors as well as possible overcharging of one of the units. A solution to the problem is the implementation of a charge equalization circuit [20] [46]. This circuit can either be a passive resistance circuit or an active switching circuit. Maxwell ultra capacitor modules have this circuit built in. The units cater for internal charge equalization as well as for charge equalization between modules.

5.8 Novel energy system configuration

The energy system configuration covered in the previous section of the chapter is a conventional system used in other EV's [21] [47]. The conventional energy system configuration has its disadvantages, especially in low voltage, high current energy systems. Some of these disadvantages can be solved by swapping around some of the energy system components. This section presents such a new system configuration. The operation of the new system is explained and the advantages and disadvantages of the new configuration are given. The section ends with a comparative study between the conventional system and the new proposed system.

Fig 5.45a shows the conventional system. The battery pack is directly connected to the drive system, with the battery voltage forming the DC bus voltage. Only small variations in this voltage occur, depending on the state of charge of the cells. A set of electrolytic capacitors are connected in parallel to the inverter. Furthermore, a converter with ultra capacitors is connected in parallel to the battery pack and inverter, as shown in Fig 5.54a. The converter is used to control the ultra capacitor current and thus the battery current. The converter has the added function of matching the ultra capacitor voltage to the bus voltage, enabling the use of the voltage range of the ultra capacitors.

The new energy system configuration simply swaps the battery pack and the ultra capacitors around, as shown in Fig 5.45b. The bus voltage is now determined by the ultra capacitor voltage. It ranges from somewhat higher than the battery pack voltage to almost the maximum ultra capacitor limit. This configuration presents a few advantages as well as disadvantages compared to the conventional system.

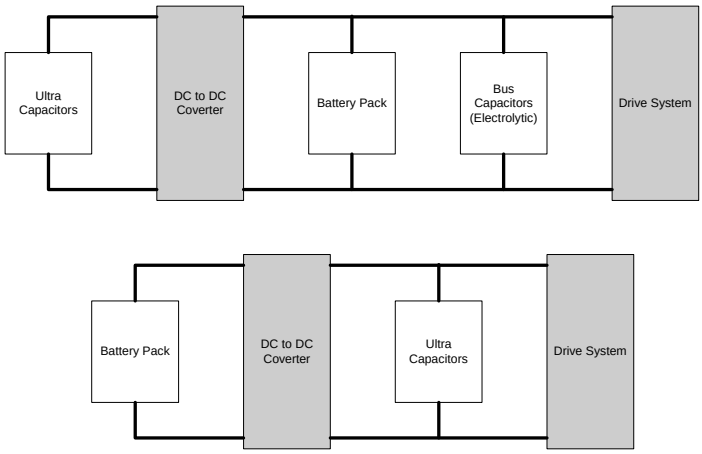

Fig 5.45: (a) Conventional and (b) proposed energy system.

By putting the ultra capacitors in parallel with the drive system, the electrolytic capacitors can be removed from the system. This is a major advantage. Electrolytic capacitors are extremely sensitive components, especially to temperature changes and vibration. Both these conditions are found in EV applications. The failure of the electrolytic capacitors could lead to short circuiting of the battery pack and drive system, causing damage. On the other hand, ultra capacitors are not sensitive to temperature, having an operating range of -20 to 120 degrees Celsius, and are not sensitive to vibration. They also have a higher cycle life than electrolytic capacitors. The volume of the drive system is also dramatically reduced by removing the electrolytic capacitors. Electrolytic capacitors also require a soft-start circuit. The inrush current that occurs when the capacitors are connected to the battery pack can damage the capacitors. This is not the case with ultra capacitors.

The main aim of the EMS is to control the battery current. In the conventional system the battery current is indirectly controlled by controlling the ultra capacitor current, as seen in Fig 5.46a. The control algorithm used to achieve this requires a minimum of five measurements; three current and two voltage measurements. The control algorithm of the energy management system can be simplified with the implementation of the proposed system. The system allows for direct control of the battery current, as can be seen from Fig 5.46b. The number of measurements is also reduced to three; two current and one voltage measurement. Full battery current control allows for optimum operation of the battery pack, increasing the performance and the life cycle of the cells. The proposed system is ideal for any system that utilizes very low specific power storage devices, including fuel cells.

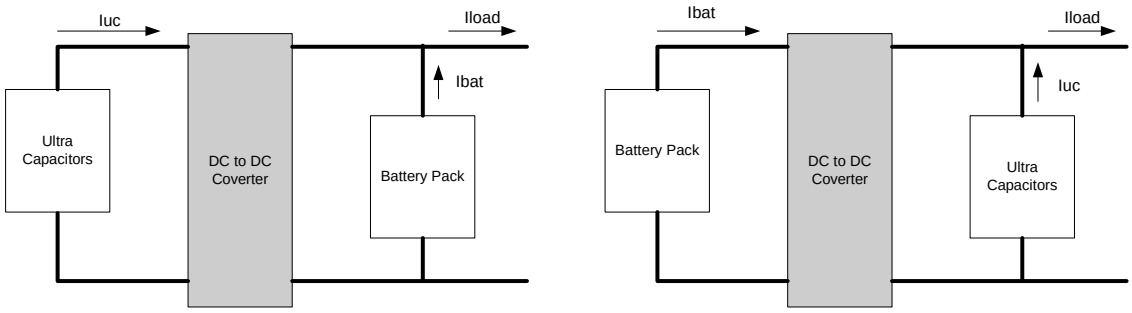

Fig 5.46: Energy system currents in (a) conventional and (b) proposed system.

The proposed system configuration has the benefit of protecting the battery pack. The converter used to connect the battery pack to the inverter not only allows for control of the battery current but also buffers the battery during high magnitude and frequency current. Although the energy management performs this task in the conventional system, it is not able to protect the battery during all situations. The converter also allows the battery pack to be isolated from the rest of the system if the need arises. It was found that the ultra capacitor current in the conventional system is extremely high. This is especially true for a low voltage, high current system. The current can exceed 1000A during certain conditions. These high currents are not experienced in the proposed system. High currents have an effect on device selection. High current power electronic devices are needed as well as a power inductor that is still able to operate under these high currents. The conductors of the inductor must be able to carry such current. Special inductor design is needed as core saturation must be avoided when the inductor is rated for high current. The power inductor will be an expensive component of the converter. Lower current requires lower rated current components leading to possible cost, weight and volume reduction.

During the experiments described in chapter 4 it was found difficult to meet the voltage requirements of the drive system without over sizing the energy capability of the battery pack. The proposed system allows the choice of an optimum battery pack as the converter matches the battery pack voltage to the drive system bus voltage. Cells with the best specific energy rating can be obtained without any consideration of voltage requirements. The cells can be placed in any configuration.

It is known that the torque of electric motors decrease at high speed, especially the permanent magnet motors purposed for the EV's. This is due to the high back EMF being generated at high speed. One of the factors that determine the maximum speed of the vehicle is the DC bus voltage. It is thus possible to increase the maximum speed of the vehicle by increasing the bus voltage. The new proposed system allows for control of the DC bus voltage. The bus voltage can be increased in certain situations, i.e. during high speed vehicle overtaking. The control of the DC bus voltage also allows it to be decreased at low speed operation. By so doing, it is possible to increase the efficiency of the inverter(s).

A real concern in the proposed system, with the removal of the electrolytic capacitors, is the stray inductance added to the system due to the DC bus connections. This is especially true for multi-inverter systems, as is the case with a vehicle having in wheel propulsion. Fig 5.47a shows such a topology. A few options exist to solve this problem. The ultra capacitor pack can be split up so that a set can be placed as close as possible to each inverter, as seen in Fig 5.47b. A second possible option is to place small, high frequency filter capacitors at the inverters.

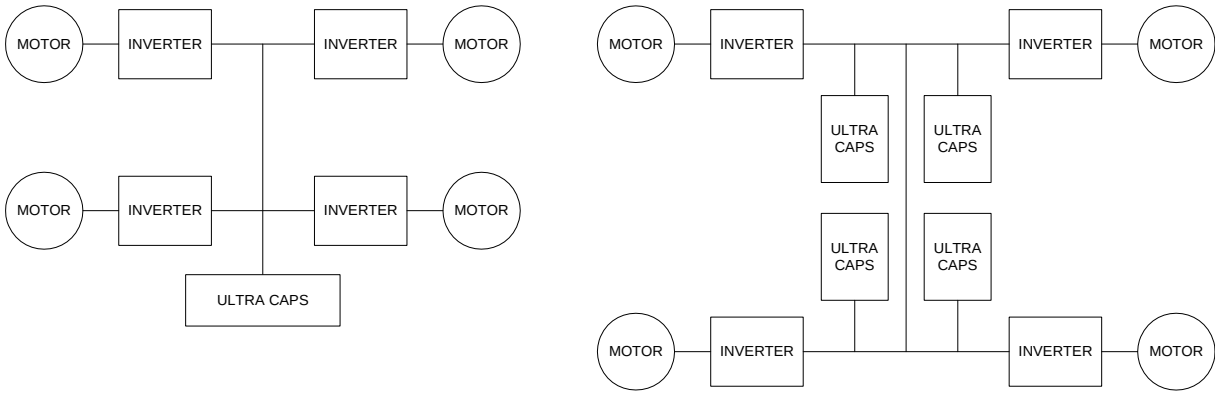

Fig 5.47: Energy system with (a) single ultra capacitor and (b) split ultra capacitor pack.

The main disadvantage of the proposed system is the DC to DC converter between the battery pack and the drive system. The series converter decreases the total efficiency of the energy system. Special attention is needed in the design of this power electronic converter in the EV system. Extraordinary high efficiency converters are required. The converter used in the proposed system adds cost and time to the design of the system. It is this added efficiency that might prevent the use of the proposed system in a specific application.

A comparative study was done between a conventional system and the proposed system. A comparison was done on aspects such as weight and cost. Table 5.2 lists the results of the comparison. Certain components were kept the same for both the systems, i.e. the battery pack, the motors drives and converter. The ultra capacitor units chosen for the study was Maxwell's BPAK0058 and BPAK0020 units. Table 5.2 shows that the ultra capacitor pack needed for the proposed system costs more, has a larger volume and a larger mass, in comparison to the ultra capacitor pack needed for the conventional system. The real benefit of the system can only be seen in the savings made in the system as a whole. The total savings in mass, volume and cost are shown in Table 5.3.

	Conventional	Proposed
Ultra Capacitors		
# Cells in Series	6	20
# Parallel Sets	4	4
# Cells in Total	24	80
Cell Capacitance	58 F	20 F
Total Capacitance	38.7 F (36.4)	4 F (3.7)
Unit Dimensions	216 x 69 x 38	178 x 52 x 32
Total Mass	13.6 kg	18.4 kg
Total Volume	13.6 litre	25.12 litre
Total Capacitor Cost	R 19 656.00	R 22 593.00
Operating Voltage	20 - 90 V	120 - 300 V
Total Capacitor Energy	149 kJ (140)	151.2 kJ (140)
Electrolytic Capacitors		
Unit Dimension (4 capacitors)	85 x 85 x 170	0
Total Mass	15 kg	0
Total Volume	19.7 litre	0
Total Cost	R 8 000.00	R 0.00
Power Inductor		
Mass	12 kg	4 kg
Volume	0.015 litre	0.005 litre
Cost	R 2 500.00	R 1 000.00
System (exl. Common Parts)		
Total Mass	43.32 kg	22.4 kg
Total Volume	39.37 litre	25.2 litre
Total Cost	R 30 156.00	R 23 593.00

Table 5.2: Comparative study between conventional and proposed system.

System (exl. Common Parts)	Proposed
Mass	20.92 kg less
Volume	14.17 litre less
Cost	R6 563.00 less

Table 5.3: Total saving when using proposed system.

Chapter 6 Conclusions and recommendations

Conclusions and recommendations regarding research work completed during the ongoing development of an electric vehicle and dealt with in this thesis are presented in this chapter. It deals with three distinct areas of the vehicle i.e. the suspension system, the traction control system and the energy system. The four overhead questions that were answered in this thesis, each falling into one of these aspects are:

- What effect has the added mass of an in-wheel motor on the safety, stability and comfort of a electric vehicle?
- What are the traction control requirements for an electric vehicle?
- How is the optimum battery pack size chosen for an electric vehicle?
- How is an auxiliary storage device added to the energy system and controlled to form an energy management system?

The effect of the added wheel mass was investigated through frequency analysis and simulation of the system. A vehicle model was derived for use in the frequency analysis and simulation. The investigation took on the form of a comparative study between a standard vehicle and a hub driven vehicle. The frequency analysis gave an indication of the stability of the vehicles. More importantly, it helped to determine if both vehicles' natural frequencies are within the comfort range. Simulation results of the two vehicles were compared to determine if there are any major differences in the response of the vehicles. Different road inputs were used in the simulations.

The concept of a traction control system for an electric vehicle is presented in this thesis. The components that make up a system as well as the minimum requirements of a traction control system are discussed. Various forms of traction control systems are also discussed. The systems are given in the form of a step by step evolution of a traction control system. It points out the fact that a wide range of control systems can be used, ranging from simple to very complex ones. A vehicle model is derived for simulation purposes. Simulation results are shown of the response of the vehicle to applied wheel torque. These results point out the need for a traction control system.

Two methods of choosing or calculating the optimum battery pack for an electric vehicle are given. All aspects that influence the size of the battery pack are mentioned as well as the equations that determine the size. A few size options are presented using each of the methods. A battery choice, for the specific vehicle under development is presented. The charge and discharge curves during one charge-discharge cycle are presented to illustrate the voltage characteristics of the Lithium based cells used.

The foundation is laid for the development of an energy management system for an EV. A system was designed, utilizing ultra capacitors as auxiliary storage device. A basic control strategy and program was developed to illustrate the operation of an energy management system. The testing of the energy management system required the development of a controlled electronic load. The control algorithm for this load was also developed. Although not tested at full capability, the results obtained from practical measurements give a clear picture of the working of the energy management system.

A completely new configuration of the energy system of the vehicle is presented. This configuration was developed to solve some of the problems encountered during the study of the conventional system. A comparative study was done between a conventional system and the new configuration. The comparison was done from a cost, weight etc. point of view and not a performance one.

6.1. Conclusions

From the results obtained during the completions of the project the following conclusions can be drawn for each of the aspects covered:

Suspension analysis:

- The frequency response analysis shows that the standard vehicle as well as the hub driven vehicles are stable systems. The natural frequencies calculated fall within the acceptable comfort ranges.
- The simulation results show that the displacement of the sprung and unsprung mass of the hub driven vehicle does not differ much from that of the standard vehicle. The vibrations experienced by the sprung mass and thus the occupants of the vehicle are not worsened by the addition of the hub motor to the unsprung mass.
- The forces exerted on the unsprung mass of the hub driven vehicle are comparable with those of a standard vehicle.
- It is the author's opinion that the study shows that hub motors can be used as propulsion for electric vehicles without affecting the stability, safety and comfort of the vehicle.

Traction control system:

- A traction control system is a necessity in an electric vehicle, in one form or another.
- Traction control systems have varying complexity. The precise strategy used is mainly dependent on the vehicle operating condition (off road, high speed etc.) and the designer of the traction control system.

Battery selection:

- Two methods exist for the calculation of the battery pack size. The method used is dependant on whether the motor specifications have already been fixed.
- The voltage requirements of the drive system (motor and inverter) play a major role in the size of the battery pack. It is usually this voltage requirement that leads to over sizing of the battery pack energy capability.
- It is difficult to obtain a battery pack without over- or under sizing the energy capability thereof of without the use of power electronics.

Energy management system:

- In some cases, energy systems require the addition of auxiliary storage devices depending on the battery technology used. Peak power conditions observed during the operation of the vehicle and which can potentially damage the cells, require a storage device. The auxiliary storage serves as a buffer for this peak power. It was found that ultra capacitors are ideal as auxiliary storage devices.
- The transfer functions for both the EMS and electronic load were derived. It was found that a transfer function for a converter with two voltage sources can be derived by using the Middlebrook and Cuk method with the super positioning principle. These transfer functions closely describe the behaviour of the converter and were successfully used to design the control algorithm for the converters.
- The ultra capacitor current can be successfully controlled with a power electronic converter. Although an indirect method, the battery current can be successfully shaped and limited by an energy management system using an auxiliary storage device such as ultra capacitors.
- The ultra capacitor peak current is extremely high in a low voltage, high current system. This high current presents its share of problems.

6.2. Recommendations

Certain issues were raised during the completion of this study. Limitations were placed on certain aspects of the study. A few recommendations for the future development of the EV as well as future topics of study are as follows:

Suspension analysis:

- A simple quarter vehicle model was used in the study of the effect of the added wheel mass. This model does not take the interaction of all four wheels into account. It might be necessary to obtain a four wheel vehicle model and the same study conducted using this model.
- Although the force analysis showed that the forces exerted on the unsprung mass of a hub driven vehicle are comparable to those of a standard vehicle, the study did not show if this is acceptable. A study into the physical structure of the hub motor is required to make this conclusion.
- The study does not determine the effect the added wheel mass has on the handling of the vehicle. It is recommended that such a study be preformed.

Traction control system:

- The thesis presents the overview of traction control in general. No developments of a actual traction control system is covered in the thesis. An area for future study is the development of a traction control system for the EV under development. This also includes the implementation thereof.

Battery selection:

- During mass production of an EV, the cells chosen for a specific vehicle should be selected after the cells have gone through the charge-discharge cycle. Results of the charge-discharge show that varying cell voltages occur within a pack, even before it has been used. Selecting cells of almost equal voltage ensures more equal voltage distribution during use of the battery and improved performance and storage capability of the battery pack.

Energy management system:

- The high ultra capacitor current is of great concern in the energy management system. This high current generates a few problems such as complicated and expensive converter components as well as high levels of EMI. Ways have to be found to decrease the ultra capacitor current without limiting the capability of the energy management system.

- The physical design of the power inductor used in the energy management system has not been dealt with in this thesis. The design of this component is often underestimated. The inductor must be designed to minimize the cost and weight implications thereof. The power inductor is a definite area of investigation in a high current system.
- A standard converter topology was used in the energy management system. High efficiency systems are required in a system such as an EV that are solely dependent on battery power. It is possible that a different converter topology will deliver a higher efficiency system.
- A very basic control program was used to control the energy management system. Upgrading of this program is required. It is possible that a better control program can be written to improve the performance of the energy management system.
- Limited testing of the energy management system was performed due to limitations placed on the testing by the test equipment. A full capability testing is required as well as implementation of the system on the vehicle. The impact of the energy management system on the range of the vehicle could not be determined from the results obtained in this thesis.
- The switching of the power electronic converters such as the inverter and the converter of the energy management system adds switching ripple to the battery current. This current ripple can be detrimental to the health and performance of the cells. An area of future investigation is to determine the amount of current ripple that is added by the power electronics as well as determining the acceptable level for this ripple.
- A new configuration for the energy system of an electric vehicle is presented in this thesis. Only the configuration concept as well as a broad comparison is given. A full evaluation of the operation and performance of the new configuration is required. A complete study on the full extent of the advantages and disadvantages of the new configuration over the conventional system is required.

References

[1] **Larminie** J. and **Lowry** J., "Electric Vehicle Technology Explained", John Wiley & Sons Ltd, 2003

[2] **Kirch** D., "The Electric Car and the Burden of History: Systems Rivalry in the United States, 1890 - 1996", P.hD. Dissertation, Stanford University, 1996

[3] **Goldstein** D., "Out of Gas", W.W. Norton, 2004

[4] **Yuan** G. and **Gladkov** A.: "Testing of a 17 kW In-wheel Propulsion System for Electric Vehicles", 21st Electric Vehicle Symposium (EVS21), (Monaco), April 2005

[5] PML QED Mini Specification, PML Flightlink Ltd, Alton, United Kingdom

[6] **Terashima** M., **Ashikaga** T., **Mizuno** T., **Natori** K., **Fujiwara** N. and **Yada** M.: "Novel Motors and Controllers for High-performance Electric Vehicle with Four In-wheel Motors", IEEE Transactions on Industry Electronics, Vol. 44, No. 1, 1997

[7] **Ohnuma** N., **Fukasawa** T., **Tanebe** T. and **Misoe** E.M..: "Essential Measures to Prevent Global Warming: A Development of Technology for Implementing Lithium-ion Battery for Traction System of Lightweight EV's", 21st Electric Vehicle Symposium (EVS21), (Monaco), April 2005

[8] **Shimamura** O., **Abe** T., **Saito** T., **Itou** T., **Kinoshita** T., **Watanabe** K., **Horie** H., **Sugawara** H., **Hirata** N. and **Miyamoto** T.: "Development of a High Power Compact Lithium-ion Battery System", 21st Electric Vehicle Symposium (EVS21), (Monaco), April 2005

[9] **Misselhorn** W.E., "Verification of Hardware-in-the-loop as a Validation Testing Method for Suspension Development", M.Eng Dissertation, University of Pretoria, November 2004

[10] **Kader** A., **Dobos** A. and **Cullinan** M.: "Speed Bump and Suspension Analysis, Linear Physics Laboratory Experiment 4", 2004

[11] **Hori** Y., **Toyoda** Y. and **Tsuruoka** Y.: "Traction Control of Electric Vehicle: Experimental Results using the Test EV 'UOT Electric March' ", IEEE transactions on Industry Applications, Vol. 34, No. 5, 1998

[12] **Sakai** S., **Sado** H. and **Hori** Y.: "Novel Skid avoidance Method without Vehicle Chassis Speed for Electric Vehicle", University of Tokyo, 2004

[13] **Sakai** S., **Sado** H. and **Hori** Y.: "Motion Control in an electric Vehicle with Four Independently Driven In-wheel Motors", IEEE transactions on Mechatronics, Vol. 4, No. , March 1999

[14] **Sakai** S., **Kitagawa** K. and **Hori** Y.: "Novel Skid avoidance Method without Vehicle Chassis Speed for Electric Vehicle", University of Tokyo, 2004

[15] **Chan** C.C., and **Chau** K.T.: "Modern Electric Vehicle Technology". Oxford science Publications, 2001

[16] **Mazza** P. and **Hammerschlag** R.: "Wind-to-wheel Energy Assessment", Institute for Lifecycle Environmental Assessment, 2000

[17] **Bohlen** O., **Blanke** H., **Buller** S., **Fricke** B., **Hammouche** A., **Linzen** D., **Thele** M., **De Doncker** R.W. and **Sauer** D.U.: "Battery Monitoring for Automotive Batteries is not a Miracle – Some Practicable Algorithms to Identify State-of-function Parameters", 21st Electric Vehicle Symposium (EVS21), (Monaco), April 2005

[18] **Chan** M.S.W., **Chau** K.T. and **Chan** C.C.: "Low-cost Hardware Implementation of Lithium-ion Battery Capacity Indicator", 21st Electric Vehicle Symposium (EVS21), (Monaco), April 2005

[19] **Wenhua** H., **Quanshi** C., **Zhenyang** F. and **Xiaodong** H.: "Development of a Battery Management System for Ni/NH Batteries in Hybrid Electric Vehicle", 21st Electric Vehicle Symposium (EVS21), (Monaco), April 2005

[20] **Jeong** J., **Lee** H., **Kim** C., **Choi** H and **Cho** B.: "A development of an Energy Storage System for Hybrid Electric Vehicles Using Supercapacitors", 21st Electric Vehicle Symposium (EVS21), (Monaco), April 2005

[21] **Lhomme** W., **Delarue** P., **Barrade** P., **Bouscayrol** A. and **Rufer** A.: "Design and Control of a Supercapacitor Storage System for Traction Applications", IEEE Industry Applications Conference, 2005

[22] **Hutak** P. and **Vorel** P.: "A Traction Drive with a Battery and Ultracapacitor"

[23] **Inman** D.J.: "Engineering Vibration", 2nd edition, Prentice Hall International Inc, 2001

[24] **Visagie** J.: "Heavy Hub Ride and Comfort Test", Optimal Energy Ltd, 2006

[25] **Jia** Y.: "Robust Control with Decoupling Performance for Steering and Traction of 4WS Vehicle Under Velocity-varying Motion", IEEE transactions on Control Systems Technology, Vol. 8, No.3, May 2000

[26] **Tseng** H.E., **Ashrafi** B., **Madau** D, **Brown** T.A. and **Recker** D.: "The development of Vehicle Stability Control at Ford", IEEE transactions on Mechatronics, Vol. 4, No.3, September 2000

[27] **Sakai** S. and **Hori** Y.: "Stable Lateral Control with Motor-controlled Wheels", 19th Electric Vehicle Symposium (EVS19), (Korea), 2003

[28] **De Kock** H.W., "Dynamic Control of the Permanent Magnet Assisted Reluctance Synchronous Machine with Constant Current Angle", M.Sc.Eng Dissertation, University of Stellenbosch, November 2005

[29] **Saitoh** T., **Hwa** T.C. and **Hori** Y.: "Realtime Generation of smart Speed Pattern for EV's taking Driver's Command Change into Account", IEEE 8th International Workshop on Advanced Motion Control, 2004

[30] **Li** L., **Kodama** S., and **Hori** Y.: "A Novel Skid-prevention Controller Based on Smart Speed Pattern Generator", 21st Electric Vehicle Symposium (EVS21), (Monaco), April 2005

[31] **Serway** R.A., **Beichner** R.J.: "Physics for Scientists and Engineers", Fifth Edition, Saunders College Publishing, 2000

[32] **Hibbeler** R.C.: "Engineering Mechanics Dynamics", SI Edition, Prentice Hall Inc, 1997

[33] **Sakai** S., **Uchida** T., **Okano** T, **Hwa** T.C. and **Hori** Y.: "4 Wheel Motored Vehicle 'UOT Electric March II – Experimental EV for Novel Motion Control Studies", IEEE transactions on Industrial Electronics, Vol. 51, No.5, October 2004

[34] **Ortuzar** M., **Moreno** J. and **Dixon** J.: "Implementation and Evaluation of an Ultracapacitor-based Auxiliary Energy System for Electric Vehicles", IEEE transactions on Industrial Electronics

[35] **Barrade** P., **Destraz** B. and **Rufer** A.: "Hybrid Vehicle in Railways Applications: Supercapacitive Energy Storage for Diesel-electric Locomotives", Vehicle Power and Propulsion Symposium, (France), 2004

[36] **Rufer** A. and **Barrade** P.: "A Supercapacitor Based Energy-Storage System for Elevators with Soft Commutated Interface", IEEE transactions on Industrial Applications, Vol. 38, No.5, September / October 2002

[37] **Miller** J.M.: "Ultra Capacitors Challenge the Battery", Article published by World and I, http://www.worldandi.com, June 2004

[38] http://en.wikipedia.org/wiki/supercapacitors Wikipedia online encyclopedia

[39] **Rix** A.J.: "Electrical Vehicle and Drive Specifications" University of Stellenbosch, February 2006

[40] **Wu** T. and **Chen** Y.: "Modelling PWM DC/DC Converters out of Basic Converter Units", IEEE transactions on Power Electronics, Vol. 13, No.5, September 1998

[41] **Jeong** J., **Lee** H., **Kim** C., **Choi** H. and **Cho** B.: "A development of an Energy Storage System for Hybrid Electric Vehicles using Supercapacitors", 19th Electric Vehicle Symposium (EVS19), (Korea), 2003

[42] **Middlebrook** R.D. and **Cuk** S.: "A General Unified Approach to Modeling Switching-converter Power Stage", Paper 5.2, Modern Power Electronics – Technology, Evolution ans Application, pp 297 – 313, Edited by Bose B.K

[43] **Mohan** N., **Undeland** T.M. and **Robbins** W.P.: "Electric Vehicle Technology Explained", Second Edition, John Wiley & Sons Ltd, 1995

[44] http://www.thermoanalytics.com/support/publications/batterymodelsdoc.html "Battery Modelling"

[45] **Stiegeler** M., **Frey** T., Rohr S. and **Kabza** H.: "Battery Management System for Lead Acid Battery with Calibration using Charge- and Discharge- Rest Voltage Characteristics", 21st Electric Vehicle Symposium (EVS21), (Monaco), April 2005

[46] **Dixon** J.W., **Ortuzar** M. and **Wiechmann** E.: "Regenaritive Braking for an Electric Vehicle using Ultracapacitors and a Buck-boost Converter", 17th Electric Vehicle Symposium (EVS17), (Canada), October 2000

[47] **Barrade** P. and **Rufer** A.: "Key Developments for Supercapacitive Energy Storage: Power Electronic Converters, Systems and Control", 2nd Boostcap Meeting, (Switzerland), 2001

[48] Lithium-ion Cell and Charging Brochure, Thundersky Lithium Battery Limited

Appendix A Suspension frequency analysis equations

The dynamic equation as given by equations 2.5 and 2.6 are:

$$M_S\ddot{x}_1 = K_S(x_2 - x_1) + B_S(\dot{x}_2 - \dot{x}_1) - K_T(x_1 - w) - B_T(\dot{x}_1 - \dot{w}) - M_S g$$
$$M_V\ddot{x}_{21} = -K_S(x_2 - x_1) - B_S(\dot{x}_2 - \dot{x}_1) - M_V g$$

These equations are rearranged as follows to obtain the dynamic equations in matrix (A.1) form:

$$M_S\ddot{x}_1 - K_S x_2 + (K_S + K_T)x_1 - B_S\dot{x}_2 + (B_S + B_T)\dot{x}_1 = K_T w - B_T\dot{w} - M_S g$$
$$M_V\ddot{x}_2 + K_S x_2 - K_S x_1 + B_S\dot{x}_2 - B_S\dot{x}_1 = -M_V g$$

$$\begin{bmatrix} M_S & 0 \\ 0 & M_V \end{bmatrix}\begin{bmatrix} \ddot{x}_1 \\ \ddot{x}_2 \end{bmatrix} + \begin{bmatrix} B_S + B_T & -B_S \\ -B_S & B_S \end{bmatrix}\begin{bmatrix} \dot{x}_1 \\ \dot{x}_2 \end{bmatrix} + \begin{bmatrix} K_S + K_T & -K_S \\ K_S & K_S \end{bmatrix}\begin{bmatrix} x_1 \\ x_2 \end{bmatrix} = \begin{bmatrix} K_T \\ 0 \end{bmatrix}\begin{bmatrix} w_1 \\ w_2 \end{bmatrix} + \begin{bmatrix} -B_S \\ 0 \end{bmatrix}\begin{bmatrix} \dot{w}_1 \\ \dot{w}_2 \end{bmatrix} + \begin{bmatrix} M_S g \\ M_V g \end{bmatrix}$$

The mass normalized stiffness matrix is required to calculate the eigenvalues of the system. The equation for the mass normalized stiffness matrix is given as:

$$\tilde{K} = M^{\frac{1}{2}} K M^{-\frac{1}{2}}$$

$$\tilde{K} = \begin{bmatrix} \sqrt{M_S} & 0 \\ 0 & \sqrt{M_V} \end{bmatrix}\begin{bmatrix} K_S + K_T & -K_S \\ -K_S & K_S \end{bmatrix}\begin{bmatrix} \frac{1}{\sqrt{M_S}} & 0 \\ 0 & \frac{1}{\sqrt{M_V}} \end{bmatrix} = \begin{bmatrix} \frac{K_S + K_T}{\sqrt{M_S}} & -\frac{K_S}{\sqrt{M_S}} \\ -\frac{K_S}{\sqrt{M_V}} & \frac{K_S}{\sqrt{M_V}} \end{bmatrix}\begin{bmatrix} \frac{1}{\sqrt{M_S}} & 0 \\ 0 & \frac{1}{\sqrt{M_V}} \end{bmatrix}$$

$$\tilde{K} = \begin{bmatrix} \frac{K_S + K_T}{M_S} & -\frac{K_S}{\sqrt{M_S M_V}} \\ -\frac{K_S}{\sqrt{M_S M_V}} & \frac{K_S}{M_V} \end{bmatrix} \qquad \text{(A.2)}$$

Substituting the parameters of the two vehicles into the above equation, the mass normalized stiffness matrices for the two vehicles are:

$$\tilde{K}_{ST} = \begin{bmatrix} 3540 & -371.463 \\ -371.463 & 128.358 \end{bmatrix}; \qquad \tilde{K}_{HD} = \begin{bmatrix} 1380 & -259.299 \\ -259.299 & 156.364 \end{bmatrix}$$

The natural frequencies of the system are calculated from the eigenvalues of the mass normalized stiffness matrix. The eigenvalues are calculated as follows:

$$\det\left(\widetilde{K}-\lambda_{eig}I\right)=0$$

$$\det\left(\widetilde{K}-\lambda_{eig}I\right)=\det\begin{bmatrix}\frac{K_S+K_T}{M_S}-\lambda_{eig} & -\frac{K_S}{\sqrt{M_S M_V}}\\ -\frac{K_S}{\sqrt{M_S M_V}} & \frac{K_S}{M_V}-\lambda_{eig}\end{bmatrix}=0$$

$$\det\left(\widetilde{K}-\lambda_{eig}I\right)=\left(\frac{K_S+K_T}{M_S}-\lambda_{eig}\right)\left(\frac{K_S}{M_V}-\lambda_{eig}\right)-\left(-\frac{K_S}{\sqrt{M_S M_V}}\right)\left(-\frac{K_S}{\sqrt{M_S M_V}}\right)=0$$

$$\det\left(\widetilde{K}-\lambda_{eig}I\right)=\lambda_{eig}^2+\left(-\frac{K_S+K_T}{M_S}-\frac{K_S}{M_V}\right)\lambda_{eig}+\left(\frac{K_S K_T}{M_S M_V}\right)=0$$

The equations for the two eigenvalues are obtained by solving this quadratic equation.

$$\lambda_1=\frac{1}{2}\left[\left(\frac{K_S+K_T}{M_S}\right)+\left(\frac{K_S}{M_V}\right)-\sqrt{\left(\frac{K_S+K_T}{M_S}+\frac{K_S}{M_V}\right)^2-4\left(\frac{K_S K_T}{M_S M_V}\right)}\right] \quad \text{(A.3)}$$

$$\lambda_2=\frac{1}{2}\left[\left(\frac{K_S+K_T}{M_S}\right)+\left(\frac{K_S}{M_V}\right)+\sqrt{\left(\frac{K_S+K_T}{M_S}+\frac{K_S}{M_V}\right)^2-4\left(\frac{K_S K_T}{M_S M_V}\right)}\right] \quad \text{(A.4)}$$

If the vehicle parameters are substituted into these equations the eigenvalues for the standard vehicle are given as:

$$\lambda_1=\frac{1}{2}\left[\left(\frac{36000+110000}{40}\right)+\left(\frac{36000}{335}\right)-\sqrt{\left(\frac{36000+110000}{40}+\frac{36000}{335}\right)^2-4\left(\frac{36000*110000}{40*335}\right)}\right]$$

$$\lambda_1=80.37$$

$$\lambda_2=\frac{1}{2}\left[\left(\frac{36000+110000}{40}\right)+\left(\frac{36000}{335}\right)+\sqrt{\left(\frac{36000+110000}{40}+\frac{36000}{335}\right)^2-4\left(\frac{36000*110000}{40*335}\right)}\right]$$

$$\lambda_2=3677.09$$

and for the hub driven vehicle:

$$\lambda_1 = \frac{1}{2}\left[\left(\frac{36000+110000}{100}\right)+\left(\frac{36000}{275}\right)-\sqrt{\left(\frac{36000+110000}{100}+\frac{36000}{275}\right)^2-4\left(\frac{36000*110000}{100*275}\right)}\right]$$

$$\lambda_1 = 96.35$$

$$\lambda_2 = \frac{1}{2}\left[\left(\frac{36000+110000}{100}\right)+\left(\frac{36000}{275}\right)+\sqrt{\left(\frac{36000+110000}{100}+\frac{36000}{275}\right)^2-4\left(\frac{36000*110000}{100*275}\right)}\right]$$

$$\lambda_2 = 1494.56$$

Appendix B Traction control equations

The starting point for deriving the equation for the static friction force is to apply Newton's second law of motion two the to bodies i.e. the vehicle and the wheel.

$$\sum F_x = M_v a_{cm} = M_v \dot{v}_v \tag{B.1}$$

$$\sum M_{cm} = J_w \dot{\omega}_w \tag{B.2}$$

If the forces and moments seen in Fig 3.5 are substituted, these equations become:

$$F_d - F_w - F_m = M_v \dot{v}_v \tag{B.3}$$

$$T_w - r_w F_d - r_w F_w = J_w \dot{\omega}_w \tag{B.4}$$

When the vehicle system is under static friction conditions, the linear acceleration of the vehicle and wheel are equal. Thus, the following equation applies:

$$\dot{v}_v = r_w \dot{\omega}_w \tag{B.5}$$

If equation B.5 is substituted into equation B.3, the wheel's rotational acceleration is given as:

$$\dot{\omega}_w = \frac{1}{M_v r_w}\left[F_d - F_v - F_m\right] \tag{B.6}$$

The following relationship can now be used to derive the equation for the driving force.

$$T_w - r_w F_d - r_w F_w = \frac{J_w}{M_v r_w}\left[F_d - F_v - F_m\right]$$

$$T_w - r_w F_d - r_w F_w = \frac{J_w}{M_v r_w} F_d - \frac{J_w}{M_v r_w}\left[F_v + F_m\right]$$

$$T_w - r_w F_w + \frac{J_w}{M_v r_w}\left[F_v + F_m\right] = \left[\frac{J_w}{M_v r_w} + r_w\right] F_d$$

$$F_d = \frac{1}{\dfrac{J_w}{M_v r_w} + r_w}\left[T_w - r_w F_w + \frac{J_w}{M_v r_w}\left(F_v + F_m\right)\right] \tag{B.7}$$

There exists a boundary between static and kinetic friction. This boundary is determined by the product of the static friction coefficient and the tyre's normal force. Static friction condition occurs if the following condition applies:

$$F_d \leq \mu_s N \tag{B.8}$$

The amount of applied wheel torque that is required to cause the system to shift from static to kinetic friction can now be determined by substituting equation B.5 into the above equation.

$$\frac{1}{\frac{J_w}{M_v r_w} + r_w}\left[T_w - r_w F_w + \frac{J_w}{M_v r_w}\left(F_v + F_m\right)\right] > \mu_s N$$

$$T_w - r_w F_w + \frac{J_w}{M_v r_w}\left(F_v + F_m\right) > \left(\frac{J_w}{M_v r_w} + r_w\right)\mu_s N$$

$$T_w > \left(\frac{J_w}{M_v r_w} + r\right)\mu_s N + r_w F_w - \frac{J_w}{M_v r_w}\left(F_v + F_m\right) \tag{B.9}$$

Appendix C Inverter topology equations

The equations that specify the number of cells that are required to meet the voltage and power criteria of the electric drive system of the EV are derived in this section. The starting point is the energy equation across the inverter. The energy equation is given as:

$$W_{bat} \cdot \eta_{in} = n_m \cdot W_m$$

where W_{bat} and W_m are the energy capability of the battery pack and the required energy by the motors, η_{in} the inverter efficiency and nm the number of motors. The equation to determine the number of cells required to meet the energy criteria of the electric motor is derived as follows:

$$W_{bat} = \frac{n_m \cdot W_m}{\eta_{in}}$$

$$I_c.h \cdot V_b = \frac{n_m \cdot W_m}{\eta_{in}}$$

$$I_c.h \cdot n_c \cdot V_c = \frac{n_m \cdot W_m}{\eta_{in}}$$

$$n_c = \frac{n_m \cdot W_m}{\eta_{in} \cdot I_c.h \cdot V_c} \qquad \text{(C.1)}$$

Equation C.1 is only valid for the electric drive configuration without the DC to DC converter. The converter efficiency needs to be taken into account when calculating the number of cells. The equation for the number of cells required when a DC to DC converter is used in the electric drive system is given as:

$$n_c = \frac{n_m \cdot W_m}{\eta_{con} \cdot \eta_{in} \cdot I_c.h \cdot V_c} \qquad \text{(C.2)}$$

The next step is to determine the equation for the number of cells required to meet the voltage criterion. Such an equation exists for each of the inverter topologies. This is due to the fact that the output voltage is different for the two topologies for the same bus voltage. The equations are derived as follows.

Half-bridge inverter:

$$V_{LL} = \frac{\sqrt{3}}{2\sqrt{2}} V_{bus}$$

$$V_{bus} = \frac{2\sqrt{2}}{\sqrt{3}} V_{LL}$$

$$n_c \cdot V_c = \frac{2\sqrt{2}}{\sqrt{3}} V_{LL}$$

$$n_c = \frac{2\sqrt{2}}{\sqrt{3}} \cdot \frac{V_{LL}}{V_c} \qquad \text{(C.3)}$$

Full-bridge inverter:

$$V_{LL} = \frac{\sqrt{3}}{\sqrt{2}} V_{bus}$$

$$V_{bus} = \frac{\sqrt{2}}{\sqrt{3}} V_{LL}$$

$$n_c \cdot V_c = \frac{\sqrt{2}}{\sqrt{3}} V_{LL}$$

$$n_c = \frac{\sqrt{2}}{\sqrt{3}} \cdot \frac{V_{LL}}{V_c} \qquad \text{(C.4)}$$

The equation for the maximum battery current is derived from the power equation across the inverter.

$$P_{bat} \cdot \eta_{in} = n_m \cdot 3 \cdot I_L \cdot V_{LN} \cdot \cos\phi$$

$$\eta_{in} \cdot V_{bat} \cdot I_{bat} = 3 \cdot I_L \cdot V_{LN} \cdot \cos\phi \cdot n_m$$

$$I_{bat} = \frac{3 \cdot I_L \cdot V_{LN} \cdot \cos\phi \cdot n_m}{\eta_{in} \cdot V_c \cdot n_c} \qquad \text{(C.5)}$$

Equation C.5 is only valid for the electric drive systems without a DC to DC converter. The converter efficiency needs to be taken into account when calculating the maximum battery current. The equation for maximum battery current for the configuration with the DC to DC converter is given as:

$$I_{bat} = \frac{3 \cdot I_L \cdot V_{LN} \cdot \cos\phi \cdot n_m}{\eta_{con} \cdot \eta_{in} \cdot V_c \cdot n_c} \qquad \text{(C.6)}$$

Appendix D EMS and electronic load transfer functions

In this section the transfer function of both the EMS and the electronic load is derived. The method used was derived by R.D. Middlebrook and S. Cuk. The method uses the circuits formed during each of the converter switching conditions to obtain the state space equations for each of these conditions. The state space equations are used in an equations derived by Middlebrook and Cuk to derive the transfer function of the system. The duty cycle of the converter forms part of the transfer function.

The Middlebrook and Cuk method can only be applied to converter systems that have one input voltage. The EMS and electronic load circuits have two input voltages. The problem is solved by applying the super positioning principle. The circuit is analyzed for each input voltage separately. The Middlebrook and Cuk method can be applied where necessary.

1. EMS

Fig D.1 shows the EMS circuit. The two input voltages are the bus voltage, V_{bus}, and the ultra capacitor initial voltage, V_{uc0}.

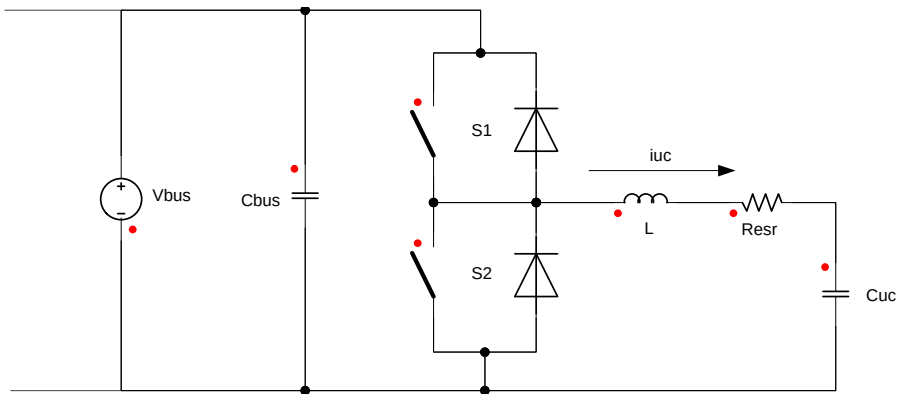

Fig D.1: Circuit diagram of EMS.

The initial capacitor voltage is set equal to zero and the Middlebrook and Cuk method is applied to the circuit for each of the switching conditions.

Top switch on, bottom switch off:

Fig D.2 shows the circuit that is formed during the switching condition where S1 is switched on and S2 is switched off.

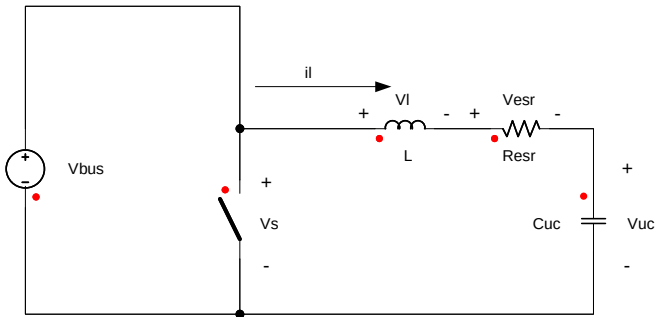

Fig D.2: Switching condition with top switch on and bottom switch off.

The state variables that are used through the derivation of the transfer function of the EMS are as follows:

$$x_1 = i_l\,; \qquad x_2 = V_{uc}\,;$$

$$\dot{x}_1 = \frac{di_l}{dt}\,; \qquad \dot{x}_2 = \frac{dV_{uc}}{dt}\,;$$

$$y = i_l$$

The state space equations are derived from the analysis of the circuit in Fig D.2.

$$V_s - V_L - V_{esr} - V_{uc} = 0$$

$$V_{bus} - L\frac{di_l}{dt} - R_{esr} i_l - V_{uc} = 0$$

$$V_{bus} - L\dot{x}_1 - R_{esr} x_1 - x_2 = 0$$

$$\dot{x}_1 = -\frac{R_{esr}}{L} x_1 - \frac{1}{L} x_2 + \frac{1}{L} V_{bus} \qquad \text{(D.1)}$$

$$i_c = i_l = C_{uc}\frac{dV_{uc}}{dt}$$

$$\dot{x}_2 = \frac{1}{C_{uc}} x_1 \qquad \text{(D.2)}$$

The state space equations in matrix form are obtained by combining equations D.1 and D.2.

$$\begin{bmatrix} \dot{x}_1 \\ \dot{x}_2 \end{bmatrix} = \begin{bmatrix} -\frac{R_{esr}}{L} & -\frac{1}{L} \\ \frac{1}{C_{uc}} & 0 \end{bmatrix} \begin{bmatrix} x_1 \\ x_2 \end{bmatrix} + \begin{bmatrix} \frac{1}{L} \\ 0 \end{bmatrix} V_{bus} \tag{D.3}$$

$$y = \begin{bmatrix} 1 & 0 \end{bmatrix} \begin{bmatrix} x_1 \\ x_2 \end{bmatrix} \tag{D.4}$$

Top switch off, bottom switch on:

Fig D.3 shows the circuit that is formed during the switching condition where S1 is switched off and S2 is switched on.

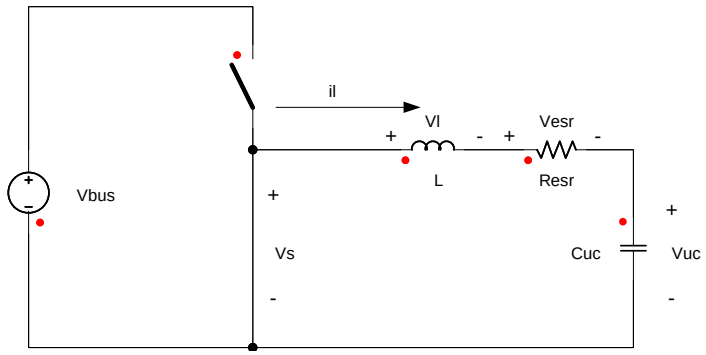

Fig D.3: Switching condition with top switch off and bottom switch on.

The same procedure is followed to obtain the state space equations for the switching condition where the top switch is off and the bottom switch is on. The equations are obtained through analysis of the circuit in Fig D.3. The same state space variables are used.

$$V_s - V_L - V_{esr} - V_{uc} = 0$$

$$-L\frac{di_l}{dt} - R_{esr} i_l - V_{uc} = 0$$

$$-L\dot{x}_1 - R_{esr} x_1 - x_2 = 0$$

$$\dot{x}_1 = -\frac{R_{esr}}{L} x_1 - \frac{1}{L} x_2 \tag{D.5}$$

$$i_c = i_l = C_{uc} \frac{dV_{uc}}{dt}$$

$$\dot{x}_2 = \frac{1}{C_{uc}} x_1 \tag{D.6}$$

The state space equations in matrix form are:

$$\begin{bmatrix}\dot{x}_1\\ \dot{x}_2\end{bmatrix}=\begin{bmatrix}-\frac{R_{esr}}{L} & -\frac{1}{L}\\ \frac{1}{C_{uc}} & 0\end{bmatrix}\begin{bmatrix}x_1\\ x_2\end{bmatrix}+\begin{bmatrix}0\\ 0\end{bmatrix}V_{bus} \tag{D.7}$$

$$y=\begin{bmatrix}1 & 0\end{bmatrix}\begin{bmatrix}x_1\\ x_2\end{bmatrix} \tag{D.8}$$

The Middlebrook and Cuk method uses a derived equation for the transfer function of a converter whereby the switching conditions of the converter are taken into account and thus the duty cycle. The duty cycle of the converter becomes the input to the system. The equation for obtaining the transfer function is given as:

$$\frac{I_1(s)}{d(s)}=C(sI-A)^{-1}\left[(A_1-A_2)X+(B_1-B_2)V_{bus}\right]+(C_1-C_2)X \tag{D.9}$$

where

$$A_1=A_2=\begin{bmatrix}-\frac{R_{esr}}{L} & -\frac{1}{L}\\ \frac{1}{C} & 0\end{bmatrix}$$

$$B_1=\begin{bmatrix}\frac{1}{L}\\ 0\end{bmatrix};\qquad B_2=\begin{bmatrix}0\\ 0\end{bmatrix}$$

$$C_1=C_2=\begin{bmatrix}1\\ 0\end{bmatrix}$$

$$A=A_1d(s)-A_2\left[1-d(s)\right]=A_2$$

These matrices are substituted in equation D.9 and the transfer function derived.

$$sI-A=\begin{bmatrix}s & 0\\ 0 & s\end{bmatrix}-\begin{bmatrix}-\frac{R_{esr}}{L} & -\frac{1}{L}\\ \frac{1}{C_{uc}} & 0\end{bmatrix}=\begin{bmatrix}s+\frac{R_{esr}}{L} & \frac{1}{L}\\ -\frac{1}{C_{uc}} & s\end{bmatrix}$$

$$adj(sI-A)=\begin{bmatrix}s & -\frac{1}{L}\\ \frac{1}{C_{uc}} & s+\frac{R_{esr}}{L}\end{bmatrix}$$

$$\det(sI-A)=\left(s+\frac{R_{esr}}{L}\right)(s)-\left(\frac{1}{L}\right)\left(-\frac{1}{C_{uc}}\right)=s^2+\frac{R_{esr}}{L}s+\frac{1}{LC_{uc}}$$

$$(sI-A)^{-1}=\frac{1}{s^2+\frac{R_{esr}}{L}s+\frac{1}{LC_{uc}}}\begin{bmatrix} s & -\frac{1}{L} \\ \frac{1}{C_{uc}} & s+\frac{R_{esr}}{L} \end{bmatrix}$$

$$\begin{bmatrix}1 & 0\end{bmatrix}\begin{bmatrix} s & -\frac{1}{L} \\ \frac{1}{C_{uc}} & s+\frac{R_{esr}}{L} \end{bmatrix}\begin{bmatrix}\frac{1}{L} \\ 0\end{bmatrix}=\begin{bmatrix}1 & 0\end{bmatrix}\begin{bmatrix} s\frac{1}{L} \\ \frac{1}{LC_{uc}} \end{bmatrix}=\frac{1}{L}s$$

$$\frac{I_l(s)}{d(s)}=\frac{\frac{1}{L}s}{s^2+\frac{R_{esr}}{L}s+\frac{1}{LC_{uc}}} \qquad \text{(D.10)}$$

Equation D.10 gives the transfer function when the initial ultra capacitor voltage is set equal to zero. The next step is to set the bus voltage equal to zero and derive the transfer function from the circuit. The Middlebrook and Cuk method is not used as the switching conditions disappear when the bus voltage is set equal to zero. The circuit analyzed to obtain the transfer function is shown in Fig D.4.

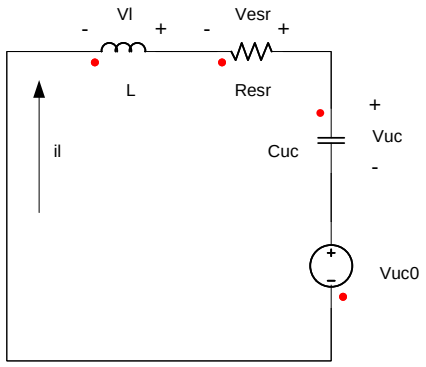

Fig D.3: Converter circuit with $V_{bus} = 0$.

The same state space variables as in the Middlebrook and Cuk method are used. The state space equations are derived as follows:

$$-V_L-V_{esr}-V_{uc}-V_{uc0}=0$$

$$-L\frac{di_l}{dt}-R_{esr}i_l-V_{uc}-V_{uc0}=0$$

$$-L\dot{x}_1-R_{esr}x_1-x_2-V_{uc0}=0$$

$$\dot{x}_1=-\frac{R_{esr}}{L}x_1-\frac{1}{L}x_2-V_{uc0} \qquad \text{(D.11)}$$

$$i_c = i_l = C_{uc}\frac{dV_{uc}}{dt}$$

$$\dot{x}_2 = \frac{1}{C_{uc}}x_1 \tag{D.12}$$

The state space equations in matrix form are given as:

$$\begin{bmatrix}\dot{x}_1\\ \dot{x}_2\end{bmatrix} = \begin{bmatrix}-\frac{R_{esr}}{L} & -\frac{1}{L}\\ \frac{1}{C_{uc}} & 0\end{bmatrix}\begin{bmatrix}x_1\\ x_2\end{bmatrix} + \begin{bmatrix}0\\ 0\end{bmatrix}V_{bus} \tag{D.13}$$

$$y = \begin{bmatrix}1\\ 0\end{bmatrix}\begin{bmatrix}x_1 & x_2\end{bmatrix} \tag{D.14}$$

Equation D.15 is used to transform the state space equations into the transfer function of the system.

$$\frac{I_l(s)}{V_{uc0}(s)} = C(sI - A)^{-1}B \tag{D.15}$$

$$sI - A = \begin{bmatrix}s & 0\\ 0 & s\end{bmatrix} - \begin{bmatrix}-\frac{R_{esr}}{L} & -\frac{1}{L}\\ \frac{1}{C_{uc}} & 0\end{bmatrix} = \begin{bmatrix}s+\frac{R_{esr}}{L} & \frac{1}{L}\\ -\frac{1}{C_{uc}} & s\end{bmatrix}$$

$$adj(sI - A) = \begin{bmatrix}s & -\frac{1}{L}\\ \frac{1}{C_{uc}} & s+\frac{R_{esr}}{L}\end{bmatrix}$$

$$\det(sI - A) = \left(s+\frac{R_{esr}}{L}\right)(s) - \left(\frac{1}{L}\right)\left(-\frac{1}{C_{uc}}\right) = s^2 + \frac{R_{esr}}{L}s + \frac{1}{LC_{uc}}$$

$$\begin{bmatrix}1 & 0\end{bmatrix}\begin{bmatrix}s & -\frac{1}{L}\\ \frac{1}{C_{uc}} & s+\frac{R_{esr}}{L}\end{bmatrix}\begin{bmatrix}-\frac{1}{L}\\ 0\end{bmatrix} = \begin{bmatrix}1 & 0\end{bmatrix}\begin{bmatrix}-s\frac{1}{L}\\ -\frac{1}{LC_{uc}}\end{bmatrix} = -\frac{1}{L}s$$

$$\frac{I_l(s)}{V_{uc0}(s)} = \frac{-\frac{1}{L}s}{s^2 + \frac{R_{esr}}{L}s + \frac{1}{LC_{uc}}} \tag{D.16}$$

2. Electronic Load

The same procedure followed to derive the transfer function of the converter circuit used in the EMS is followed to derive the transfer function for the electronic load. Fig D.5 shows the electronic load system.

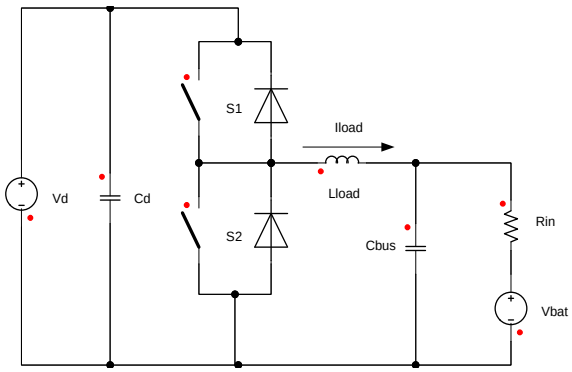

Fig D.5 Electronic load circuit.

The battery voltage, V_{bat}, is set equal to zero and the Middlebrook and Cuk method is applied to the circuit to obtain the transfer function of the system.

Top switch on, bottom switch off:

Fig D.6 shows the circuit that is formed during the switching condition where S1 is switched on and S2 is switched off.

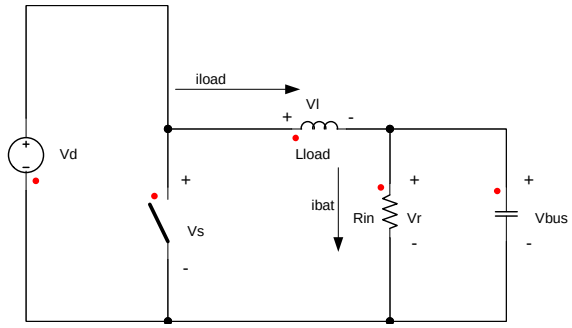

Fig D.6 Switching condition with top switch on and bottom switch off.

The state variables that are used through the derivation of the transfer function of the EMS are as follows:

$$x_1 = i_{load}\,; \qquad x_2 = V_{bus}\,;$$

$$\dot{x}_1 = \frac{di_{load}}{dt}\,; \qquad \dot{x}_2 = \frac{dV_{uc}}{dt}\,;$$

$$y = i_l$$

The state space equations are derived from the analysis of Fig D.6.

$$V_r = V_{bus}$$

$$R_{in}\left(i_{load} - i_c\right) = V_{bus}$$

$$R_{in}x_1 - R_{in}C_{bus}\dot{x}_2 = x_2$$

$$\dot{x}_2 = \frac{1}{C_{bus}}x_1 - \frac{1}{R_{in}C_{bus}}x_2 \tag{D.17}$$

$$V_s - V_L - V_r = 0$$

$$V_d - L_{load}\frac{di_l}{dt} - R_{in}\left(i_{load} - i_c\right) = 0$$

$$V_d - L_{load}\frac{di_{load}}{dt} - R_{in}i_{load} + R_{in}C_{bus}\frac{dV_{bus}}{dt}$$

$$\dot{x}_1 = \frac{R_{in}C_{bus}}{L_{load}}\dot{x}_2 - \frac{R_{in}}{L_{load}}x_1 + \frac{1}{L_{load}}V_d$$

$$\dot{x}_1 = \frac{R_{in}C_{bus}}{L_{load}}\left[\frac{1}{C_{bus}}x_1 - \frac{1}{R_{in}C_{bus}}x_2\right] - \frac{R_{in}}{L_{load}}x_1 + \frac{1}{L_{load}}V_d$$

$$\dot{x}_1 = -\frac{1}{L_{load}}x_2 + \frac{1}{L_{load}}V_d \tag{D.18}$$

The state space equations in matrix form are given as:

$$\begin{bmatrix}\dot{x}_1\\ \dot{x}_2\end{bmatrix} = \begin{bmatrix}0 & -\frac{1}{L_{load}}\\ \frac{1}{C_{bus}} & -\frac{1}{R_{in}C_{bus}}\end{bmatrix}\begin{bmatrix}x_1\\ x_2\end{bmatrix} + \begin{bmatrix}\frac{1}{L_{load}}\\ 0\end{bmatrix}V_d \tag{D.19}$$

$$y = \begin{bmatrix}1\\ 0\end{bmatrix}\begin{bmatrix}x_1 & x_2\end{bmatrix} \tag{D.20}$$

Top switch off, bottom switch on:

Fig D.7 shows the circuit that is formed during the switching condition where S1 is switched off and S2 is switched on.

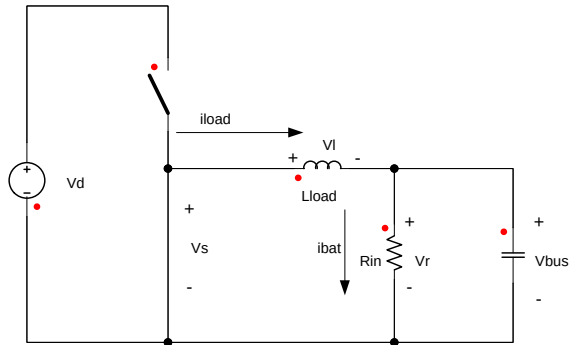

Fig D.7: Switching condition with top switch off and bottom switch on.

The state space equations are derived from the analysis of the circuit in Fig D.7.

$$V_r = V_{bus}$$

$$R_{in}\left(i_{load} - i_c\right) = V_{bus}$$

$$R_{in}x_1 - R_{in}C_{bus}\dot{x}_2 = x_2$$

$$\dot{x}_2 = \frac{1}{C_{bus}}x_1 - \frac{1}{R_{in}C_{bus}}x_2 \qquad \text{(D.21)}$$

$$-V_L - V_r = 0$$

$$-L_{load}\frac{di_l}{dt} - R_{in}\left(i_{load} - i_c\right) = 0$$

$$-L_{load}\frac{di_{load}}{dt} - R_{in}i_{load} + R_{in}C_{bus}\frac{dV_{bus}}{dt}$$

$$\dot{x}_1 = \frac{R_{in}C_{bus}}{L_{load}}\dot{x}_2 - \frac{R_{in}}{L_{load}}x_1$$

$$\dot{x}_1 = \frac{R_{in}C_{bus}}{L_{load}}\left[\frac{1}{C_{bus}}x_1 - \frac{1}{R_{in}C_{bus}}x_2\right] - \frac{R_{in}}{L_{load}}x_1$$

$$\dot{x}_1 = -\frac{1}{L_{load}}x_2 \qquad \text{(D.22)}$$

The state space equations in matrix form are as follows:

$$\begin{bmatrix}\dot{x}_1\\ \dot{x}_2\end{bmatrix}=\begin{bmatrix}0 & -\dfrac{1}{L_{load}}\\ \dfrac{1}{C_{bus}} & -\dfrac{1}{R_{in}C_{bus}}\end{bmatrix}\begin{bmatrix}x_1\\ x_2\end{bmatrix}+\begin{bmatrix}0\\ 0\end{bmatrix}V_d \tag{D.23}$$

$$y=\begin{bmatrix}1\\ 0\end{bmatrix}\begin{bmatrix}x_1 & x_2\end{bmatrix} \tag{D.24}$$

The Middlebrook and Cuk method uses a derived equation for the transfer function of a converter whereby the switching conditions of the converter are taken into account and thus the duty cycle. The duty cycle of the converter becomes the input to the system. The equation for obtaining the transfer function is given as:

$$\frac{I_l(s)}{d(s)}=C(sI-A)^{-1}\left[(A_1-A_2)X+(B_1-B_2)V_d\right]+(C_1-C_2)X \tag{D.25}$$

where

$$A_1=A_2=\begin{bmatrix}0 & -\dfrac{1}{L_{load}}\\ \dfrac{1}{C_{bus}} & -\dfrac{1}{R_{in}C_{bus}}\end{bmatrix}$$

$$B_1=\begin{bmatrix}\dfrac{1}{L_{load}}\\ 0\end{bmatrix};\quad B_2=\begin{bmatrix}0\\ 0\end{bmatrix}$$

$$C_1=C_2=\begin{bmatrix}1\\ 0\end{bmatrix}$$

$$A=A_1d(s)-A_2\left[1-d(s)\right]=A_2$$

These matrices are substituted in equation D.9 and the transfer function derived.

$$sI-A=\begin{bmatrix}s & 0\\ 0 & s\end{bmatrix}-\begin{bmatrix}0 & -\dfrac{1}{L_{load}}\\ \dfrac{1}{C_{bus}} & -\dfrac{1}{R_{in}C_{bus}}\end{bmatrix}=\begin{bmatrix}s & \dfrac{1}{L_{load}}\\ -\dfrac{1}{C_{bus}} & s+\dfrac{1}{R_{in}C_{bus}}\end{bmatrix}$$

$$adj(sI-A)=\begin{bmatrix} s+\dfrac{1}{R_{in}C_{bus}} & -\dfrac{1}{L_{load}} \\ \dfrac{1}{C_{bus}} & s \end{bmatrix}$$

$$\det(sI-A)=\left(s+\frac{1}{R_{in}C_{bus}}\right)(s)-\left(\frac{1}{L_{load}}\right)\left(-\frac{1}{C_{bus}}\right)=s^2+\frac{1}{R_{in}C_{bus}}s+\frac{1}{L_{load}C_{bus}}$$

$$(sI-A)^{-1}=\frac{1}{s^2+\dfrac{1}{R_{in}C_{bus}}s+\dfrac{1}{L_{load}C_{bus}}}\begin{bmatrix} s+\dfrac{1}{R_{in}C_{bus}} & -\dfrac{1}{L_{load}} \\ \dfrac{1}{C_{bus}} & s \end{bmatrix}$$

$$\begin{bmatrix}1 & 0\end{bmatrix}\begin{bmatrix} s+\dfrac{1}{R_{in}C_{bus}} & -\dfrac{1}{L_{load}} \\ \dfrac{1}{C_{bus}} & s \end{bmatrix}\begin{bmatrix}\dfrac{1}{L_{load}} \\ 0\end{bmatrix}=\begin{bmatrix}1 & 0\end{bmatrix}\begin{bmatrix}\dfrac{1}{L_{load}}s+\dfrac{1}{R_{in}C_{bus}L_{load}} \\ \dfrac{1}{L_{load}C_{bus}}\end{bmatrix}=\frac{1}{L_{load}}s+\frac{1}{R_{in}C_{bus}L_{load}}$$

$$\frac{I_l(s)}{d(s)}=\frac{\dfrac{1}{L_{load}}s+\dfrac{1}{R_{in}C_{bus}L_{load}}}{s^2+\dfrac{1}{R_{in}C_{bus}}s+\dfrac{1}{L_{load}C_{bus}}} \qquad \text{(D.26)}$$

As with deriving the transfer function of the EMS, the bus voltage, V_d, is set equal to zero. Fig D.8 shows the circuit that is formed when this is done. The state space equations are derived from the analysis of the circuit in Fig D.8.

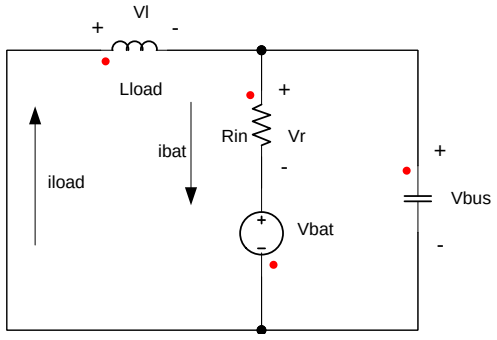

Fig D.8: Converter circuit with V_d= 0.

$$-V_L - V_{bus} = 0$$

$$-L_{load}\frac{di_l}{dt} - V_{bus} = 0$$

$$\dot{x}_1 = -\frac{1}{L_{load}}x_2 \qquad \text{(D.27)}$$

$$-V_L - V_r - V_{bat} = 0$$

$$-L\frac{di_{load}}{dt} - R_{in}\left(i_{load} - i_c\right) - V_{bat} = 0$$

$$-L_{load}\dot{x}_1 - R_{in}x_1 + V_{bat} + R_{in}C_{bus}\dot{x}_2 = 0$$

$$-L_{load}\left(-\frac{1}{L_{load}}x_2\right) - R_{in}x_1 + R_{in}C_{bus}\dot{x}_2 - V_{bat} = 0$$

$$\dot{x}_2 = \frac{1}{C_{bus}}x_1 - \frac{1}{R_{in}C_{bus}}x_2 + \frac{1}{R_{in}C_{bus}}V_{bat} \tag{D.28}$$

The state space equations in matrix form are:

$$\begin{bmatrix}\dot{x}_1\\ \dot{x}_2\end{bmatrix} = \begin{bmatrix}0 & -\frac{1}{L_{load}}\\ \frac{1}{C_{bus}} & -\frac{1}{R_{in}C_{bus}}\end{bmatrix}\begin{bmatrix}x_1\\ x_2\end{bmatrix} + \begin{bmatrix}0\\ \frac{1}{R_{in}C_{bus}}\end{bmatrix}V_{bat} \tag{D.29}$$

$$y = \begin{bmatrix}1\\ 0\end{bmatrix}\begin{bmatrix}x_1 & x_2\end{bmatrix} \tag{D.30}$$

The transfer function can now be derived by using the state space equations.

$$\frac{I_l(s)}{V_{bat}(s)} = C(sI - A)^{-1}B \tag{D.31}$$

$$sI - A = \begin{bmatrix}s & 0\\ 0 & s\end{bmatrix} - \begin{bmatrix}0 & -\frac{1}{L_{load}}\\ \frac{1}{C_{bus}} & \frac{1}{R_{in}C_{bus}}\end{bmatrix} = \begin{bmatrix}s & \frac{1}{L_{load}}\\ -\frac{1}{C_{bus}} & s + \frac{1}{R_{in}C_{bus}}\end{bmatrix}$$

$$adj(sI - A) = \begin{bmatrix}s + \frac{1}{R_{in}C_{bus}} & -\frac{1}{L_{load}}\\ \frac{1}{C_{bus}} & s\end{bmatrix}$$

$$\det(sI - A) = \left(s + \frac{1}{R_{in}C_{bus}}\right)(s) - \left(-\frac{1}{L_{load}}\right)\left(-\frac{1}{C_{bus}}\right) = s^2 + \frac{1}{R_{in}C_{bus}}s + \frac{1}{L_{load}C_{bus}}$$

$$\begin{bmatrix}1 & 0\end{bmatrix}\begin{bmatrix}s + \frac{1}{R_{in}C_{bus}} & -\frac{1}{L_{load}}\\ \frac{1}{C_{bus}} & s\end{bmatrix}\begin{bmatrix}0\\ \frac{1}{R_{in}C_{bus}}\end{bmatrix} = \begin{bmatrix}1 & 0\end{bmatrix}\begin{bmatrix}-\frac{1}{R_{in}L_{load}C_{bus}}\\ \frac{s}{R_{in}C_{bus}}\end{bmatrix} = -\frac{1}{R_{in}L_{load}C_{bus}}$$

$$\frac{I_l(s)}{V_{bat}(s)} = \frac{-\frac{1}{R_{in}L_{load}C_{bus}}}{s^2 + \frac{1}{R_{in}C_{bus}}s + \frac{1}{L_{load}C_{bus}}} \tag{D.32}$$

Appendix E EMS and battery system photos

Fig E.1: Single Thundersky Lithium-ion battery cell.

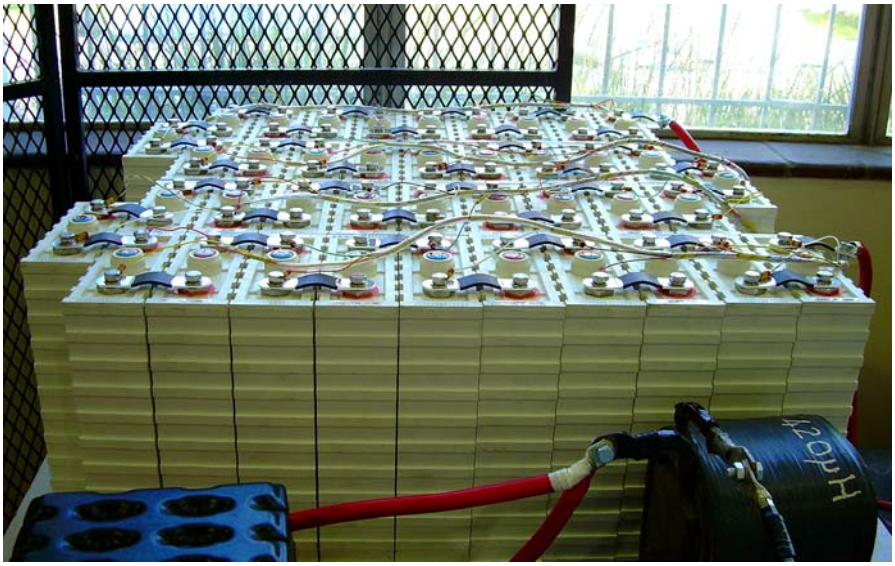

Fig E.2: Battery pack layout for laboratory testing of EMS.

Fig E.3: Charger supplied with Thundersky Lithium-ion battery cells.

Fig E.4: Battery Management System control and display unit.

Fig E.5: Coreless inductor used in laboratory setup of EMS.

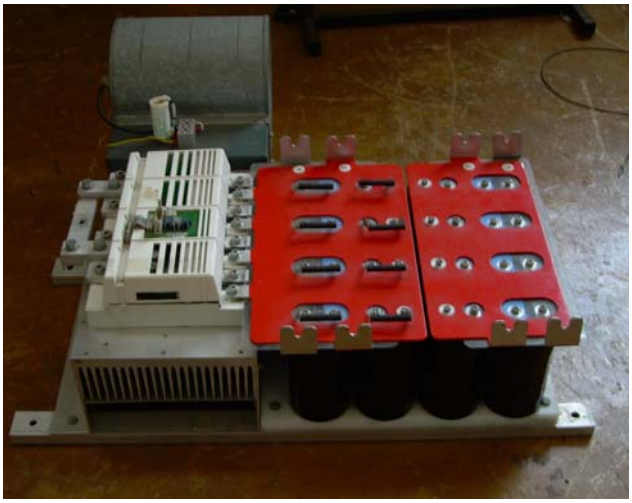

Fig E.6: IGBT phase arm unit with bus capacitors and cooling.

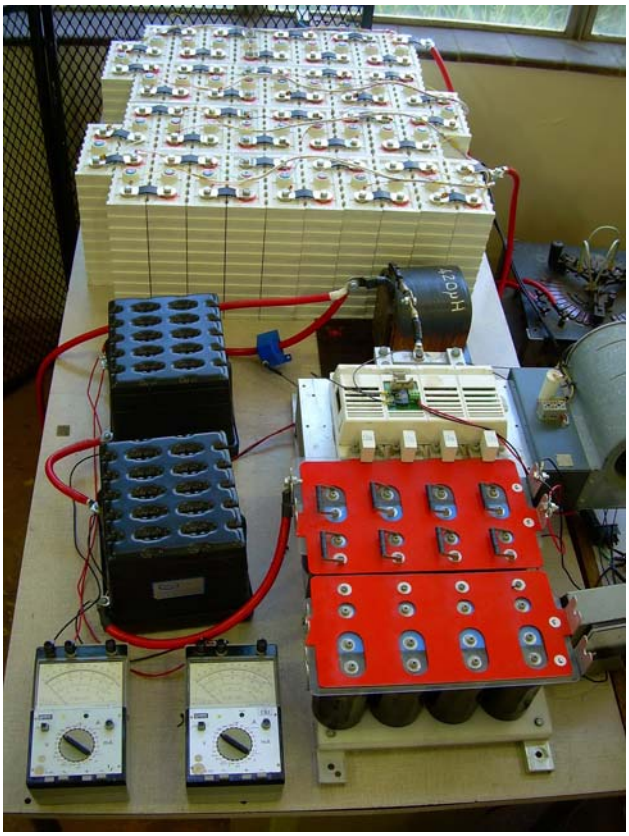

Fig E.7: Laboratory setup of EMS.